

MICROANALYTICAL CHARACTERIZATION OF SLAGGING DEPOSITS IN A PILOT-SCALE COMBUSTOR

J. West and J.N. Harb
Department of Chemical Engineering and
Advanced Combustion Research Center
Brigham Young University
Provo, Utah 84602

Keywords: Slagging, coal ash deposits, SEMPC

INTRODUCTION

The purpose of this work was to characterize a set of deposit samples with respect to their compositions, phases present, and morphology. An understanding of how these properties change as a deposit grows is essential to developing a physical picture of deposit behavior, especially transitions in behavior from heterogeneous agglomerations of particles to highly sintered particles, or even a completely homogeneous molten phase that assimilates all impacting particles. Indeed, these deposit properties are of primary importance in determining the effect of deposition on heat transfer through the water wall, and on the removability of the deposit. These properties must be understood and quantified in order to predict deposition behavior.

ANALYSIS PROCEDURE

Analyses were performed on two water-wall samples from ABB-CE's Fireside Performance Test Facility (FPTF), a pilot-scale facility which operates at temperatures, heat fluxes and residence times representative of those found in full-scale units [1]. Both deposit samples were formed while firing the same U.S. Eastern Bituminous coal. The samples were cross-sectioned and prepared for analysis in a Scanning Electron Microscope (SEM). An ISIS microanalytical system equipped with X-ray and backscatter detectors was used to run a Scanning Electron Microscopy Point Counting (SEMPC) analysis [2] to determine elemental compositions at discrete points on the sample. Backscattered electron (BSE) images were also collected and evaluated, in which the brightness of a point is proportional to the atomic number of the species present at that point. Thus, in BSE images of these samples, regions with heavy elements such as iron are bright white, aluminosilicates are light grey, silicates are dark grey, and the epoxy mounting medium is black.

An important consideration in this work is the changes in deposit properties as the deposits grows, or increases in thickness. Thus, the samples analyzed were cross-sectioned, and analyses of these samples were conducted in 10-12 discrete regions of the deposit, from the initial layer to the outer region of the deposit. Since it is not possible in this forum to discuss each of the regions individually, we have chosen to discuss three regions representative of the changes taking place. Of particular interest in this study is the transition from 'inner layer' behavior to the strongly sintered outer layer, since this transition is often the one that leads to formation of tenacious or otherwise troublesome slagging deposits [3].

RESULTS AND DISCUSSION

Changes in morphology of the deposit samples provide an excellent framework from which to understand changes in other deposit properties and behavior. Figures 1, 2, and 3 are BSE images of three distinct regions of the deposit, referred to as the inner layer, intermediate region, and outer region, respectively. Both of the samples analyzed showed dramatic changes in morphology through the deposit in the direction of deposit growth. Figure 1 shows the morphology of the initial layer, which can be characterized by its small particle size and discrete and spherical particles. Immediately next to the initial layer, the particles become larger and less round and regular in shape and appearance. The intermediate region occurs as the particles show signs of sintering and/or agglomeration, as shown in Fig. 2. However, discrete Fe-rich and Si-rich particles are still evident throughout this region of the deposit. Next there occurs, in gradual increments, the increased sintering and assimilation of particles, culminating in a largely homogeneous phase at the outer region where crystallization can be observed (Fig. 3).

These changes in morphology are strongly connected to changes in the elemental and phase

compositions throughout the deposit. Figure 4 shows a triangular histogram of the compositions of Fe, Al and Si in the initial layer of the deposit, which has been normalized to elemental mole percents (not oxides). It can be seen that the bulk of the particles are kaolinite-type aluminosilicates with an Al/Si ratio of approximately one and a small amount of Fe. There are also significant amounts of Fe-rich and Si-rich particles present. Figure 5 is a ternary diagram which corresponds to the intermediate region of the deposit (Fig. 2). In this region, the deposit is heterogeneous. The number of Fe-rich and Si-rich particles has begun to decrease due to mixing with the aluminosilicate phases, resulting in the overall broadening of the range of compositions toward more Fe and Si-rich aluminosilicates. Note that the compositions are spread over a much wider region than in the initial layer. The heterogeneity is an indication of local assimilation of Fe-rich and Si-rich particles. At the outer region of the deposit, the compositions form into a more narrow band as the deposit becomes more homogeneous. A small increase in Al-rich aluminosilicates ($Al/Si > 1$) is also observed, corresponding to the crystallization of mullite ($3(Al_2O_3)_2(SiO_2)$) in the deposit.

In the samples studied, K was deposited selectively in the inner layer of the deposit. Table 1 shows the bulk elemental compositions from each of the regions analyzed, from inner to outer regions; the amount of K_2O present in the initial layer is significantly higher than that found in the deposit regions further from the wall. It should also be noted from Table 1 that, other than the initial layer, the bulk concentration remains largely constant throughout all regions of the deposit. Therefore, it is the phase distribution that changes in different regions of the deposit rather than the elemental composition.

Analysis of the distribution of K in the deposit phases shows that the amount of particles with more than 3 mole % of K decreased dramatically from the initial layer to the intermediate region of the deposit. This shift occurred as the potassium aluminosilicate particles were assimilated into other aluminosilicates. This assimilation tends to decrease the melting temperature of the resulting mixture, facilitating the assimilation of other particles and resulting in an increase in cluster size. Therefore, K-aluminosilicates played a significant role in the transition from the inner layer to the intermediate layer.

Although the elemental percent of Fe was relatively constant throughout the deposit (Table 1), the phases in which it was found changed significantly. The distribution of Fe-containing particles in the inner layer showed the presence of some Fe-aluminosilicates with relatively high amounts of iron (>10 mole %). These particles, presumably formed by coalescence of aluminosilicates and Fe-rich minerals in the coal, appeared to be assimilated early (just outside the inner layer). Iron assimilation appeared to be localized in the intermediate region of the deposit. In contrast, the iron content was much more homogeneous in the outer regions of the deposit.

CONCLUSIONS

For the coal and combustor system analyzed, the results indicate that both K and Fe have significant effects on deposition behavior in the early deposition stage. Both K and Fe act to accelerate the sintering and melting behavior of the aluminosilicates which make up the bulk of the deposit. In particular, Fe played an important role throughout the deposit, and its distribution was indicative of the extent of homogeneity of the deposit.

Through detailed microanalytical characterization of deposits from a combustor representative of a utility boiler, we have shown the presence of inherently different and distinct regions of the deposit. The transitions between these regions are the key to determining when undesirable deposit behavior is likely to occur, and are also important to determining the mechanisms which determine deposit behavior and properties in each region. Additional work is needed in this area to enhance the ability to quantify deposit behavior and properties at all stages of deposit growth and to develop mechanisms which can be applied in mathematical models to predict deposition behavior.

ACKNOWLEDGMENTS

This work was sponsored by the Advanced Combustion Engineering Research Center. Funds for this Center are received from the National Science Foundation, the State of Utah, 42 industrial participants, and the U.S. Department of Energy. We wish to thank ABB-CE for providing the samples from their FPTF.

REFERENCES

- [1] Combustion Engineering, "Developing a Coal Quality Expert: Combustion and Fireside Performance Characterization Factors," Progress Report, July 1992.
- [2] Jones, M.L., Kalmanovitch, D.P., Steadman, E.N., Zygarlicke, C.J., and Benson, S.A., "Application of SEM Techniques to the Characterization of Coal and Coal Ash Products" in H.L.C. Meuzelaar (Ed.), *Advances in Coal Spectroscopy*, Plenum Press, New York, 1991.
- [3] Wain, T.F., Livingston, W.R., Sanyal, A., and Williamson, J., "Thermal and Mechanical Properties of Boiler Slags of Relevance to Sootblowing," in S.A. Benson (Ed.), *Inorganic Transformations and Ash Deposition During Combustion*, United Engineering Trustees, Inc., New York, 1992.

Table 1: Selected bulk elemental compositions at regions throughout the deposit (oxide mole %). Region numbers begin at the initial layer and increase through the outer region.

| Region No. | Al ₂ O ₃ | SiO ₂ | K ₂ O | CaO | TiO ₂ | Fe ₂ O ₃ |
|------------|--------------------------------|------------------|------------------|------|------------------|--------------------------------|
| 1 | 34.66 | 50.77 | 3.27 | 1.49 | 1.56 | 6.21 |
| 2 | 33.37 | 55.9 | 2.13 | 1.24 | 1.6 | 4.65 |
| 3 | 33.23 | 53.36 | 1.91 | 2.09 | 1.66 | 6.97 |
| 4 | 32.85 | 56.36 | 1.59 | 1.64 | 1.48 | 5.57 |
| 5 | 31.51 | 56.52 | 1.65 | 1.68 | 1.44 | 6.64 |
| 6 | 31.77 | 56.92 | 1.68 | 1.36 | 1.45 | 6.28 |
| 7 | 32.69 | 56.18 | 1.57 | 1.38 | 1.73 | 5.91 |
| 8 | 30.96 | 58.35 | 1.44 | 1.31 | 1.5 | 5.85 |
| 9 | 31.08 | 56.94 | 1.66 | 1.37 | 1.39 | 7.03 |
| 10 | 27.96 | 52.56 | 1.33 | 1.4 | 1.24 | 7.85 |
| 11 | 30.71 | 57.42 | 1.66 | 1.35 | 1.31 | 7.08 |
| 12 | 30.75 | 57.67 | 1.74 | 1.5 | 1.47 | 6.43 |
| 13 | 31.84 | 56.47 | 1.69 | 1.52 | 1.45 | 6.63 |

Figure 1. BSE image of the initial layer of the deposit (600x).

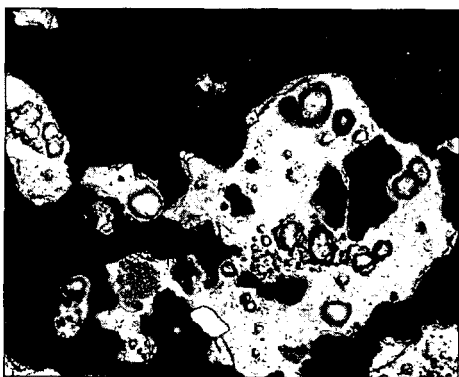
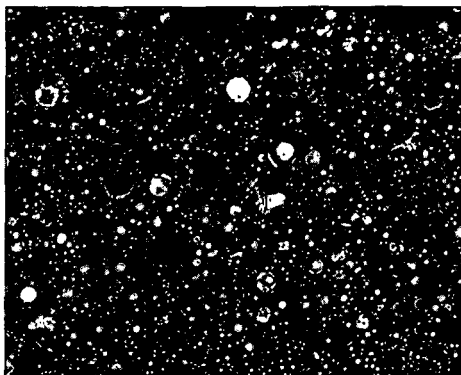
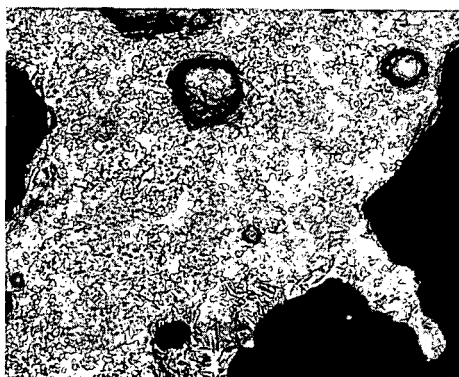


Figure 2. BSE image of the intermediate region of the deposit (300x).

Figure 3. BSE image of the outer region of the deposit (300x).



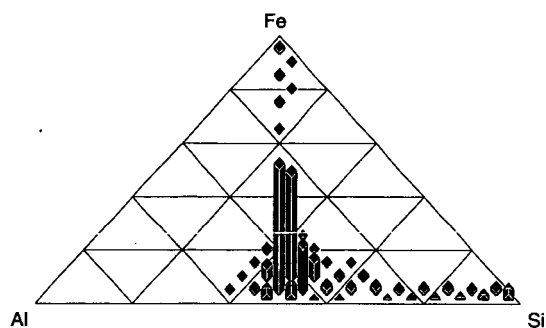


Figure 4. Frequency distribution of compositions found in the initial layer of the deposit (mole %).

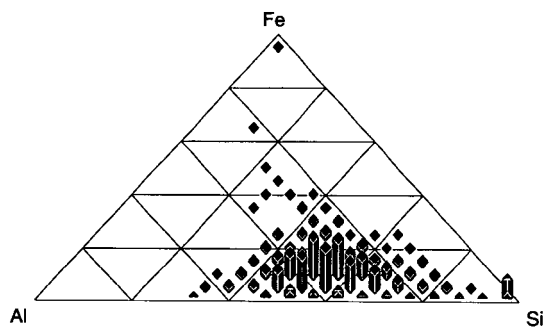


Figure 5. Frequency distribution of compositions found in the intermediate region of the deposit (mole %).

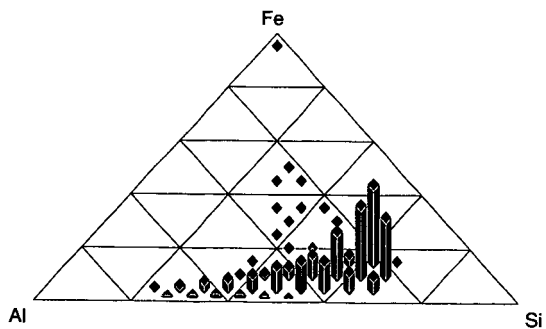


Figure 6. Frequency distribution of compositions found in the outer region of the deposit (mole %).

HYDROTHERMAL REACTION OF $\text{Ca}(\text{OH})_2$ WITH QUARTZ IN COAL

J. Wang and A. Tomita
Institute for Chemical Reaction Science,
Tohoku University, Sendai 980, Japan

G. H. Taylor
Research School of Earth Science,
Australian National University,
GPO Box 4, Canberra ACT2601, Australia

Keywords: Quartz; Coal; Demineralization

ABSTRACT

Quartz is generally most abundant as mineral matter in coal. In order to obtain fundamental information for chemical demineralization of coal with $\text{Ca}(\text{OH})_2$, the hydrothermal reaction of $\text{Ca}(\text{OH})_2$ with reagent quartz has been studied in detail. The results showed that the quartz was converted to various silicates, depending on autoclaving conditions. At a CaO/SiO_2 ratio of about 1, quartz was initially converted to $\text{Ca}_2\text{SiO}_4 \cdot \text{H}_2\text{O}$, then to tobermorite-like compounds, and finally to xonotlite. Higher temperature and longer reaction time are preferable to the complete conversion of quartz. The formed calcium silicates were susceptible to dissolution in acid.

INTRODUCTION

The presence of minerals in coal causes many serious disadvantages in coal utilization. A great deal of effort has been concentrated on removal of mineral matter from coal. Chemical cleaning has attracted much attention because of its high removal efficiency^{1,2}. In general, however, high processing costs have been a major barrier to commercialization of these processes. We proposed a chemical leaching method by using a cheaper and less corrosive reagent, lime, for coal demineralization and found that 75% of the ash in Newstan coal could be removed from coal³.

Among numerous mineral species present in coal, quartz, together with clays, carbonates and sulfides constitute the most common species⁴. Therefore, the understanding of the reaction between $\text{Ca}(\text{OH})_2$ and quartz is of fundamental significance as far as coal demineralization by $\text{Ca}(\text{OH})_2$ leaching is concerned. Although the reactions in the system of quartz/lime/water have been investigated in relation to cement and concrete production^{5,6}, the reactions were extremely complex and the products considerably varied with the hydrothermal conditions. The principal aim of this paper is to study the hydrothermal reaction between $\text{Ca}(\text{OH})_2$ and reagent quartz from the standpoint of coal demineralization. On the basis of the results obtained by using pure quartz, the reaction between $\text{Ca}(\text{OH})_2$ and quartz in coal is further examined.

EXPERIMENTAL

Pulverized lime used in this study contained $40 \pm 15\%$ of $\text{Ca}(\text{OH})_2$ (estimated by TG analysis) with other impurities of less than 2%. α -Quartz (Kanto Chemical Co.) had a particle size distribution of -325 mesh: 30%, 325-200 mesh: 68% and 200-100 mesh: 2%.

Hydrothermal reactions were carried out at saturated steam pressures using an autoclave equipped with a stirrer. About 2.5 g of quartz powder with a pulverized lime was used for each run with 150 ml of distilled water. After being autoclaved, all specimens were dried at 105°C under a nitrogen atmosphere. The specimens were stored in tightly stoppered bottles. The coal demineralization method was in detail described elsewhere³.

The assignment of products by X-ray diffraction (XRD) was carried out after drying at 105°C, whereas the semi-quantitative XRD analysis to determine the amount of unreacted quartz was made after heat treatment at 850°C. After this treatment, most of calcium silicates were nearly free of water and this procedure enables to evaluate the exact weight of sample on

an XRD sample holder. X-ray photoelectron spectroscopy (XPS) analysis was accomplished with Shimadzu ESCA 750 spectrometer. Scanning electron microscopes (SEM) used were Cambridge S360 with Tracor Northern EDAX equipment and Hitachi S2250N with Link System EDAX equipment.

RESULTS AND DISCUSSION

Hydrothermal reaction between $\text{Ca}(\text{OH})_2$ and reagent quartz

Selected X-ray diffraction patterns for the samples obtained at 300°C are illustrated in Figure 1. Table 1 lists the reaction products obtained at various temperatures with a CaO/SiO_2 molar ratio of 0.93 ± 0.02 . At 175°C, the major product was $\text{Ca}_2\text{SiO}_4 \cdot \text{H}_2\text{O}$ ($\text{C}_2\text{SW}(\text{A})$ according to Eitel's nomenclature⁷). Some other weak peaks were difficult to be identified, however they were probably due to compounds similar to tobermorite ($\text{Ca}_4\text{Si}_5\text{O}_{14} \cdot 5\text{H}_2\text{O}$)⁵. At 250°C and 300°C, the major product was also $\text{Ca}_2\text{SiO}_4 \cdot \text{H}_2\text{O}$ during a relatively short period of time, but tobermorite-like compounds were more distinct than at 175°C especially after 5 h. At 7 h, the XRD intensity for a new phase, xonotlite, became very strong and the peak for $\text{Ca}_2\text{SiO}_4 \cdot \text{H}_2\text{O}$ almost disappeared at both temperatures. When the temperature was raised up to 340°C, the tendency of the changes of products with time was virtually the same as observed for 300°C, although the reaction became more prompt. Only xonotlite was observed after 5 h.

The variations of quartz conversion with time during autoclaving at different temperatures are shown in Figure 2. When the autoclaving at 175°C was prolonged up to 12 h, about half of quartz was converted and $\text{Ca}(\text{OH})_2$ disappeared completely (Table 1). A higher temperature is necessary to convert the rest of quartz. At higher temperatures, the quartz conversion took place in two stages. The first stage was a relatively rapid reaction in which the main reaction was the formation of $\text{Ca}_2\text{SiO}_4 \cdot \text{H}_2\text{O}$. Thus, it can be said that at a CaO/SiO_2 molar ratio of about 1, this stage roughly terminated when half of quartz was converted. In the second stage, the main reactions were the transformation of $\text{Ca}_2\text{SiO}_4 \cdot \text{H}_2\text{O}$ to tobermorite-like compounds and/or xonotlite. These reactions were relatively slow compared with the formation of $\text{Ca}_2\text{SiO}_4 \cdot \text{H}_2\text{O}$.

XPS analysis was used to determine the binding energy of Si_{2p} in reagent quartz and in two treated samples (No. 9 and No. 13 presented in Table 1). The XPS spectra showed that the chemical environment of Si greatly changed due to the formation of $\text{Ca}_2\text{SiO}_4 \cdot \text{H}_2\text{O}$ and xonotlite. This change may be related to greater solubility of the products in acidic solution.

Interaction between $\text{Ca}(\text{OH})_2$ and quartz in coal

Newstan coal was taken as an example. The properties of this coal were presented previously³. The examination of this coal, by XRD analysis and SEM-EDAX analysis, showed that quartz and clay were dominated mineral phases in the original coal. When the coal was subjected to $\text{Ca}(\text{OH})_2$ leaching followed by a dilute HCl washing, the XRD analysis showed that most of quartz could be removed. Figure 3 is the SEM-EDAX analysis of a treated sample obtained at 320°C and 1.5 h by use of 5% CaO before acid washing. The observed particle was strongly attacked by $\text{Ca}(\text{OH})_2$, forming Ca-bearing phases. Elements in spot A were mainly Ca and Si, which might be a calcium silicate derived from the reaction between $\text{Ca}(\text{OH})_2$ and quartz. The rich elements in Spot B were Ca, Si and some Al. This observation suggests another important reaction occurring between $\text{Ca}(\text{OH})_2$ and clays in coal. The SEM analysis of the acid-washed sample indicated that the Ca-bearing silicate products were removed by the acid solution. After the acid-washing of the treated sample, the ash content was reduced from 9.2 % of the original coal to 2.6 %. As can be seen from Figure 2, the above autoclaving condition (320°C, 1.5 h) was not enough for a complete removal of quartz. Thus we tried to use a longer reaction time for demineralization of Newstan coal. The treatment at 300°C for 7 h produced a clean coal with much lower ash content, 1.0 %.

CONCLUSION

1. Upon the hydrothermal reaction with Ca(OH)_2 , quartz formed various hydrated calcium silicates, depending on the autoclaving conditions. Increasing temperature from 175°C to 340°C significantly accelerated the reaction.

2. At a CaO/SiO_2 ratio of about 1, the reaction between Ca(OH)_2 and quartz initially resulted in $\text{Ca}_2\text{SiO}_4 \cdot \text{H}_2\text{O}$. As the reaction proceeded, $\text{Ca}_2\text{SiO}_4 \cdot \text{H}_2\text{O}$ progressively reacted with residual SiO_2 to form tobermorite-like compounds. Final product at higher temperature and longer time was xonotlite. Through these reactions, quartz could be completely converted to calcium silicates.

3. Quartz was a major mineral phase in Newstan coal. During the leaching of this coal, the quartz was reacted by Ca(OH)_2 forming Ca-bearing phases, which was removed by dilute HCl washing. The ash content could be reduced from 9.2 % to 1.0 %.

ACKNOWLEDGMENTS

The authors thank Dr. Y. Kobayashi of Tohoku University for many helpful discussions. New Energy and Industrial Technology Development Organization are also acknowledged for the financial support (International Joint Research Grant).

REFERENCES

1. Wang, Z. Y.; Ohtsuka, Y.; and Tomita, A. *Fuel Process. Technol.* **13**, 279-289 (1986).
2. Waugh, A. B.; Bowling, K. McG. *Fuel Process. Technol.* **9**, 217-233 (1984).
3. Wang, J.; Kobayashi, Y.; Tomita, A.; Zhang, Z. G. *Proc. 8th International Conference on Coal Science*, Oviedo, Spain, 1995.
4. Jenkins, R. G. and Walker, P. L. Jr. in "Analytical Methods for Coal and Coal Products II"; Karr, Jr. C. Eds.; Academic Press, New York, 1979, 265-314.
5. Ahmed, A. H. M. and Taylor, H. F. W. *J. Appl. Chem.*, **19**, 245-246 (1969).
6. Kalousek, G. L. *J. Amer. Concrete Inst.*, **6**, 889-1011 (1955).
7. Eitel, W. "Silicate Science IV"; Academic Press: New York, 1966: p. 260.

Table 1. Products of hydrothermal reactions of Ca(OH)_2 with quartz at a CaO/SiO_2 molar ratio of 0.93.

| No. | Conditions | | Products* | | | | |
|-----|------------|----------|----------------|-------------------|----|---|----|
| | Temp. (°C) | Time (h) | SiO_2 | Ca(OH)_2 | A | T | X |
| 1 | 175 | 3 | vs | m | s | w | - |
| 3 | 175 | 7 | vs | s | s | w | - |
| 4 | 175 | 12 | s | - | vs | w | - |
| 5 | 250 | 1.5 | vs | s | s | w | - |
| 6 | 250 | 3 | vs | w | s | m | - |
| 7 | 250 | 5 | s | - | vs | m | - |
| 8 | 250 | 7 | s | - | - | m | vs |
| 9 | 300 | 1 | vs | s | s | w | - |
| 11 | 300 | 3 | s | w | vs | w | - |
| 12 | 300 | 5 | m | - | s | m | s |
| 13 | 300 | 7 | - | - | - | - | vs |
| 14 | 340 | 0.75 | vs | w | s | s | - |
| 17 | 340 | 5 | - | - | - | - | vs |

* A: α -Dicalcium silicate hydrate ($\text{Ca}_2\text{SiO}_4 \cdot \text{H}_2\text{O}$); T: Tobermorite-like compounds; X: Xonotlite ($\text{Ca}_6\text{Si}_6\text{O}_{18} \cdot \text{H}_2\text{O}$). vs: very strong; s: strong; m: medium; w: weak.

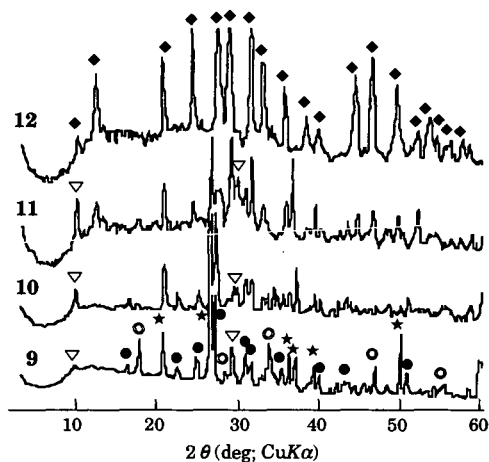


Figure 1 XRD patterns of the specimens obtained at 300°C. The sample numbers indicated correspond to those in Table 1.
 ●: $\text{Ca}_2\text{SiO}_4 \cdot \text{H}_2\text{O}$; ★: Quartz + $\text{Ca}_2\text{SiO}_4 \cdot \text{H}_2\text{O}$; ○: $\text{Ca}(\text{OH})_2$;
 ▽: Tobermorite-like compounds.

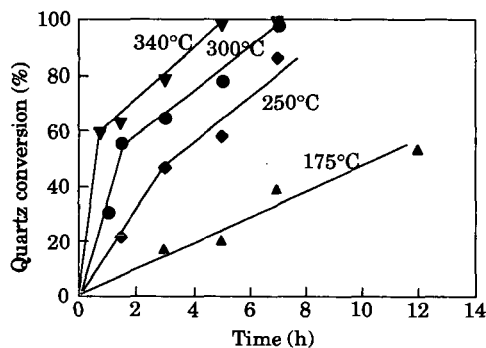


Figure 2 Quartz conversion during the hydrothermal reaction at a CaO/SiO_2 molar ratio of 0.93.

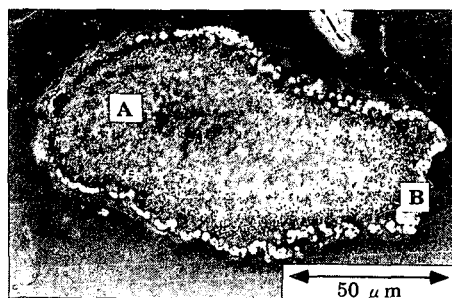


Figure 3 Scanning electron micrograph of mineral matter in coal after the reaction with $\text{Ca}(\text{OH})_2$.

BEHAVIOR OF IRON BEARING MINERALS IN THE EARLY STAGES OF PULVERIZED COAL CONVERSION PROCESSES

Harl Babu Vuthaluru, Simon Eenkhoorn, Gerrit Hamburg and Peter Heere
Netherlands Energy Research Foundation ECN, Business Unit ECN Fossil Fuels
P.O. Box 1, 1755 ZG Petten, The Netherlands

Keywords: combustion, gasification, pyrite

ABSTRACT

Early stage transformations and deposition of iron bearing coal minerals, in particular pyrite (FeS_2) were studied. An atmospheric lab-scale facility was used to simulate the near burner environments in two different coal conversion processes: i) Low- NO_x pulverized fuel combustion and ii) Entrained-flow gasification. Particle sampling showed that for both environments, the pyrite was transformed quickly to pyrrhotite (FeS). In the deposition experiments this pyrrhotite impacts on the substrates. In the deposition experiments, the chemical composition and the morphology of the slags formed under the two conditions showed clear differences. Special attention was paid to the role of sulphur. Based on these (preliminary) experiments, a mechanistic model is proposed for the transformations of pyrite in both pulverized coal conversion systems. Furthermore a description is given of a new experimental setup for future work at elevated pressures (up to 20 bar) to enable a closer simulation of pressurized entrained-flow coal gasification processes.

INTRODUCTION

In the Netherlands, oxygen-blown entrained-flow gasification has been selected as the most promising technology for large scale coal-based power generation. This is mainly due to its fuel flexibility, high efficiency and relatively low environmental impact. The world's first fully Integrated Gasification Combined Cycle (IGCC) demonstration plant (250 MWe) based on (Shell) gasification technology is currently in operation in Buggenum.

To support and ensure a successful introduction of IGCC and other new coal-based power generation technologies, the coal-related research at ECN is extended to include these technologies. To this purpose, the staged flat flame burner concept has been adapted which was successfully applied earlier to simulate (low- NO_x) pulverized coal combustion conditions accurately on a laboratory scale (1,2). The atmospheric test facility was reconstructed from an open up-fired to a closed down-fired system, where the off-gases are flared. The facility was renamed as the Atmospheric Entrained-Flow Gasification and Combustion simulator (AEFGC-simulator). The coal/mineral particles are carried along in the combustion gas and thus the high initial temperatures and very rapid particle heat-up in both combustion and gasification can be simulated in this facility.

For entrained-flow gasification conditions, the mechanism of the formation of slags was explored by depositing the mineral particles onto alumina plates, simulating gasifier wall. The plates were held at a temperature of around 1450 °C, characteristic for that of the wall in an actual entrained-flow gasifier (3). Experience with slag production in the reducing environment of low- NO_x burners (4,5) was used in the evaluation of the results.

EXPERIMENTAL

Laboratory-scale test facility

The test facility is an entrained-flow reactor with an integrated, premixed and multistage flat flame gas burner. A schematic view of the simulator is given in Figure 1. The burner consists of two sub-burners viz. an inner burner (10.9 mm) and an outer burner (60.7 mm). A tertiary gas stream (consisting of nitrogen) is applied to create suitable mixing profiles and to protect the tube from the hot secondary gas stream. Coal/char particles are fed through the inner burner and undergo rapid heating ($> 10^3$ °C/s) up to the high temperature level of the near-burner zone in the actual process. The particles are fed at a feed rate of approximately 1 g/h by means of a rotating brush feeder (4). The gas/particle flow is confined to a 76 mm ID (ceramic) reactor tube with a length of 550 mm. The tube is surrounded by a controllable heating section equipped with Kanthal Super 33 elements to create the required temperature history for the particles.

Coal choice

The experimental work has been performed with pyrite rich coal (Prince coal, Canada). Coal with a high content of iron minerals (pyrite) was chosen because iron is known to react with the reducing gasifier gas. Narrow size fractions (pyrite enriched) were used in the experiments. The specifications of this coal and preparation techniques have been described in detail elsewhere (4).

Sampling and analysis

Sampling of in-flame particles was carried out with a quench probe followed by a cyclone and a filter. Ash particles were sampled isokinetically from the hot gas at distances corresponding to residence times of 90, 120, 170 ms using a helium-fed quench probe under entrained-flow gasification conditions. However, for combustion conditions, ash particles were sampled at distances corresponding to residence times of 18, 22, 50 and 120 ms. Experimental conditions used in the present investigations are given in Tables 1 and 2. The samples were analyzed with SEM with simultaneous characterization of composition and morphology. In addition, a deposition probe was used for slagging tests. On this probe different substrate materials (high grade Al_2O_3 and SiC) were placed to simulate wall surface material. The plates were placed at distances corresponding to residence times of 50ms for combustion conditions and 90, 120, 170ms for gasification conditions. The plates were held in the particle stream for 15 minutes at a furnace wall temperature of 1500 °C. After completion of the test, cold helium gas was introduced along the plates via the tip of the probe holder. Perpendicular cross-sections through the deposit plates and attached deposits were examined with SEM for internal

structure. Single spots and complete layers were analyzed. Elemental mapping was also performed to obtain the profile for a given element in the layer. The measured gas temperatures for both low- NO_x combustion and entrained-flow gasification conditions are as shown in Figure 2.

RESULTS

Both the results obtained for low- NO_x combustion and entrained-flow gasification conditions are detailed in the following sections.

Ash formation experiments

Analysis of ash particles formed under entrained-flow gasification revealed the formation of cenospheres, clusters (50-60 μm) and some skeletal structures. Several small fragments were also found which consisted of Al, Si, Fe and K. Similar ash particles were formed under low- NO_x combustion conditions.

Figure 3 summarizes the measured sulphur to iron ratios both under simulated low NO_x conditions, as extracted from earlier work (5), and simulated entrained-flow gasification conditions. The measured ratio of S/Fe present as pyrite in the coal is shown in the figure for comparison purposes. From the figure it can be observed that for combustion conditions the pyrite transforms quickly to pyrrhotite (FeS) in 20 ms. At increasing residence times a further transformation to FeOS or FeO found to occur. For entrained-flow gasification, also a quick transformation to pyrrhotite occurs. However, here the pyrrhotite appears to be remain stable at longer residence times. Nevertheless, it should be noted that the gasification experiments were conducted with 1% H_2S in the gas, while no sulphur compound was added in the combustion experiments.

Deposition experiments

Low- NO_x combustion

Figure 4 shows the internal structure of the deposit. Elemental analysis closer to the plate showed enrichment in Al. This strongly suggests interaction of slag with substrate material (Al-sint). The crystals at the top and bottom are spinels (iron-alumina). These deposits consisted of several dendrites enriched in iron were found (Figure 4). The iron enrichment in the top and first layer is presumably due to preferential crystallization of iron-alumina spinel at these regions. The slag matrix (second layer) was enriched in silicon. Analysis of the deposits showed no sulphur.

Entrained-flow gasification

Figure 5 shows the cross-sectional view of the deposit plate and the deposits collected at three locations within the reactor. All the deposits contained several bubbly regions. Slag flow was observed for the deposits collected at two locations (viz. 270 mm, 370 mm) within the reactor. However, for the deposits collected at a distance of 520mm, no slag flow was observed along the sides of the deposit plate. This is probably due to misalignment of the probe within the reactor. In addition, changing gas environments may have led to this sort of slag flow behavior. This requires further attention. The slag matrix in all deposits was rich in Fe, Si, Al and small proportions of O. Also some interaction of iron with SiC substrate material was seen. Especially the analysis of the white spots (see Figure 5a) at the interface revealed Fe and Si. No sulphur was found in the deposits.

MECHANISTIC MODEL FOR PYRITE TRANSFORMATIONS

Observed flame transitions of pyrite under low NO_x combustion and entrained-flow gasification conditions are shown in Figure 6. It appears from the experimental results that the first reaction process is not oxidation but decomposition of pyrite into pyrrhotite in both processes (see Figure 3). This may be explained by the evolution of sulphur gas which prevents the oxygen from reaching the particles (6). The rapid melting of the pyrrhotite was evidenced by the rounded shape of the collected particles. Overall, the present test results indicate that the final product for low NO_x combustion being Fe_2O_3 whereas for entrained-flow gasification Fe is the final product.

Although our preliminary experiments have shown that both combustion and gasification processes can be realized in the AEFGC-simulator, it would be more appropriate to conduct the gasification tests at elevated pressures. To enable these experiments at elevated pressures (up to 20 bar), new experimental facility based on the same concept has been built (the so-called Pressurized Entrained-Flow Gasification simulator). Commissioning work of this facility is currently in progress and it will be available for carrying out experiments at elevated pressures early 1996.

CONCLUSIONS

Preliminary experiments have shown that both the low- NO_x combustion and entrained-flow gasification experiments can be realized in the AEFGC-simulator. Irrespective of the gas conditions prevailing within the reactor, the deposits did not contain sulphur. Ash particles collected in the vicinity of the burner before deposition showed sulphur in the sample, suggesting the transformation of pyrite to pyrrhotite. Upon deposition the sulphur in pyrrhotite appeared to be released from the slag into the gas phase. End products in the slag for both low NO_x combustion and entrained-flow gasification processes were determined to be Fe_2O_3 and Fe respectively.

ACKNOWLEDGEMENTS

The authors acknowledge the financial support from the European Community under the Joule II Extension Program for the project 'Slagging in Low- NO_x Combustion and Entrained-Flow Gasification'. The authors are also thankful to Dr. H.M. ten Brink and Dr. J.H.A. Kiel for their valuable suggestions.

REFERENCES

- [1] H.M. ten Brink, S. Eenkhoorn and G. Hamburg: *Slagging in entrained-flow gasification and low- NO_x firing conditions*. In: Proc. Engineering Foundation Conference on 'The Impact of Ash Deposition on Coal Fired Plants', June 20-25, 1993, Solihull, U.K. (ed. Williamson, J. and Wigley, F., UK, 1994), pp 113-122.

- [2] H.M. ten Brink, S. Eenkhoorn and M. Weeda: *Flame transformations of coal-siderite*. In: Proc. Engineering Foundation Conference on 'The Impact of Ash Deposition on Coal Fired Plants', June 20-25, 1993, Solihull, U.K. (ed. Williamson, J. and Wigley, F., UK, 1994), pp 373-383.
- [3] R. Wetzel: *PRENFLO-Pressurized Entrained-Flow Coal Gasification. Final Report Phase 2*, Report EUR 13091 EN, 1990.
- [4] H.M. ten Brink, S. Eenkhoorn and G. Hamburg: *Flame-transformations of coal-pyrite*, ECN-report ECN-RX--95-037 [1995]. Also submitted to Fuel (July, 1995).
- [5] H.M. ten Brink, S. Eenkhoorn and G. Hamburg: *A mechanistic study of the slag formation from Iron-rich coals*, ECN-report ECN-RX--95-041 [1995]. Also submitted to Fuel Processing Technology (August, 1995).
- [6] Srinivasachar, S. and A.A. Boni: *A kinetic model for pyrite transformations in a combustion environment*, Fuel 1989, 68, 29.

Table 1: Gas mixtures before combustion (gas flows in l/min)

| | Low-NO _x combustion | | Entrained-flow gasification | |
|------------------|--------------------------------|--------------|-----------------------------|--------------|
| | Inner Burner | Outer burner | Inner Burner | Outer burner |
| CH ₄ | 0.133 | 3.98 | 0.5 | 0.2 |
| CO | | | | 15 |
| CO ₂ | | | 1.56 | |
| O ₂ | | | 1 | 1.67 |
| H ₂ S | | | 0.008 | |
| Air | 1.0 | 30.0 | | |

Table 2: Experimental conditions

| | Low-NO _x combustion | Entrained-flow gasification |
|-------------------------------|---|-----------------------------|
| Particle feed rate (in g/h) | 1 | 1 |
| Furnace temperature (°C) | 1500 | 1450 |
| Sampling residence times (ms) | | |
| sample 1 | 18 | 90 |
| sample 2 | 22 | 120 |
| sample 3 | 50 | 170 |
| sample 4 | 120 | - |
| Deposit substrate | High grade Al ₂ O ₃ | High grade SiC |
| Deposit plate | 15mm x 50mm, 2mm thick | 15mm x 50mm, 2mm thick |
| Deposit formation time (min) | 15 | 20 |

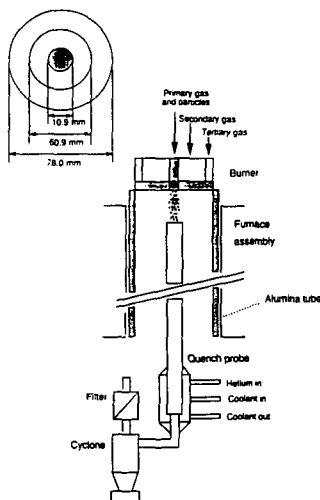


Figure 1: Atmospheric Entrained-Flow Gasification and Combustion simulator (AEFGC-simulator).

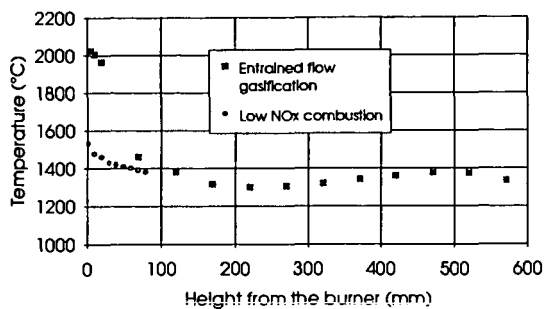


Figure 2: Measured gas temperature profiles within the reactor.

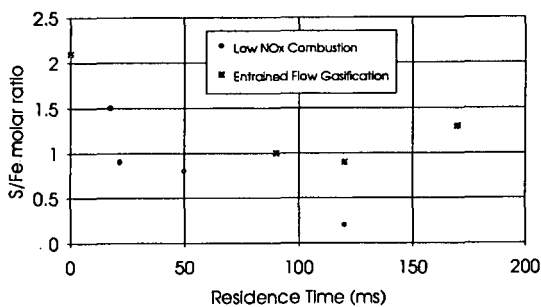


Figure 3: Sulfur to iron molar ratio against reaction time.

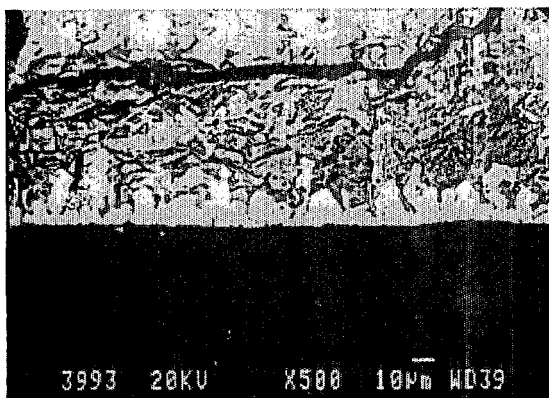


Figure 4: Cross-section perpendicular through the deposit plate (combustion experiments)

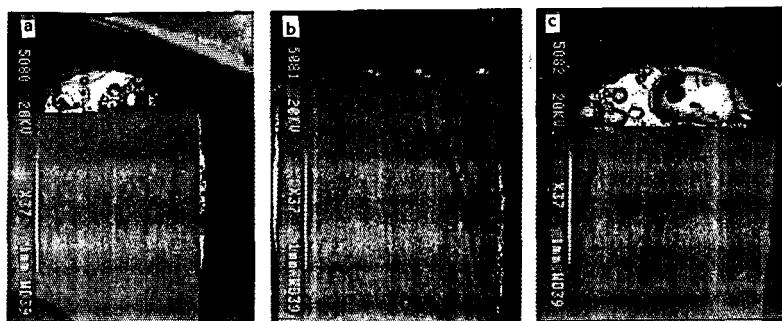


Figure 5: Cross-section perpendicular through the deposit plate (gasification experiments) at different probe locations. a) 270mm; b) 370mm; c) 520mm.

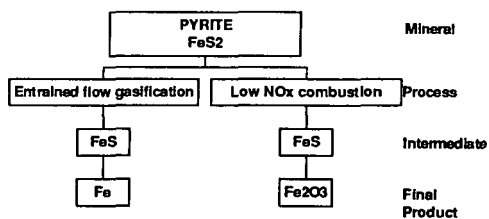


Figure 6: Mechanistic model for pyrite transformations

RELATIONSHIPS BETWEEN MAJOR INORGANIC ELEMENTS AND MINERALS
IN COALS FROM THE ASHIBETSU DISTRICT, ISHIKARI COAL FIELD, JAPAN

Tatsuo Kimura
Energy Resources Department
National Institute for Resources and Environment
16-3 Onogawa, Tsukuba-shi, 305 Japan

Keywords: Minerals, Major inorganic elements, Correlation coefficient

INTRODUCTION

Information from both mineralogical and elemental analyses of coal is important for coal utilization technologies such as combustion, gasification, liquefaction, and coking, as well as for environmental considerations. The analyses have often been carried out separately. However, a combination of both analyses would bring more fruitful results than separate analyses concerning the nature of the mineral matter in coal. Two methods of coal sample collection for both analyses are available: collection of various kinds of coal samples on rank from different locations and collection of coal samples from different coal seams at the same location. The former method provides a wide range of information on coal mineral phases and elements and the latter provides precise specification of coal mineralogical and elemental characteristics. The goal of this study was to explore the relationships between major inorganic elements and mineral phases in coals by analyzing samples from different coal seams in the Ashibetsu district, Ishikari coal field, Japan. The geochemical implications of mineral abundances were previously reported (1-3).

ANALYTICAL PROCEDURES

Coal samples were hand picked along vertical transects from near roof to near floor at seven coal pit faces of six coal seams. Coal samples containing less than 40% ash were selected. Minerals were identified by X-ray diffraction analysis of the low-temperature ashes (LTA) obtained by ashing powdered coal samples in an oxygen plasma reactor. The major inorganic element (Si, Al, K, Ti, Na, Mg, Ca, Fe, Sr, P, F, and Cl) and total sulfur contents were determined by X-ray fluorescence analysis.

RESULTS AND DISCUSSION

Kaolinite and quartz are the most dominant silicate minerals in coals from the Ashibetsu district (Table 1), and were found from the very lowest ash to the highest ash coals. The silicate minerals, plagioclase, illite, illite/smectite (I/S) mixed-layer clay minerals, smectite and K-smectite were also found, but chlorite is very rare. Calcite and ankerite are the most dominant carbonate minerals. They occur as cleat and fracture fillings (3). Carbonates also occurred as siderite, dolomite (Fe-dolomite) and aragonite. Siderite and dolomite are syngenetic minerals which occur as aggregates of fine nodules (3). Pyrite was abundant in only one coal seam and marcasite was very rare. The low abundance of pyrite suggests that most of these coal seams were formed under fresh water environments. Gypsum, which was identified as bassanite or anhydrite in the LTA, and other five iron sulfate minerals occur in some coal samples as a result of weathering of pyrite. Apatite was present in more than 60% of the coal samples, and was sometimes accompanied by goyazite. Some coal samples contained boehmite.

The high correlation coefficients between all pairings of ash, Si, Al, K, Ti, and Na (Table 2) indicates that these five elements are associated with silicate minerals. The correlation coefficient between Si and ash contents is the highest because Si is contained in quartz and all aluminosilicate minerals in the coal samples. Most of the Al is associated with aluminosilicate minerals, although a minor fraction is also associated with goyazite and boehmite.

The ash and K contents (Fig. 1) of the coal samples containing K-bearing clay minerals (illite, K-smectite, and/or I/S mixed-layer clay minerals) were closely correlated, indicating that K is contained as an interlayer cation in these clay minerals. The Al and Ti contents (Fig. 2) were closely correlated (correlation coefficient 0.83). Ti is thought to substitute for Al in clay minerals and the maximum amount of Ti substituted for Al was 12.5%. Several studies (4-7) have already pointed out that the correlation coefficients between any pair of ash, Si, Al, K, and Ti are high and that these elements are associated with silicate minerals in coal. However, the mineral species associated with these elements have not previously been determined.

Relatively high correlation coefficients for Na with ash, Si, Al, K, and Ti suggest that the Na content reflects the existence of Na-bearing minerals such as plagioclase, smectite, and I/S mixed-layer clay minerals. The weight ratio of Na to ash is higher for the coal samples containing two or three Na-bearing minerals than for those containing one Na-bearing mineral.

Fig. 3 shows ash versus Mg. The Mg and ash contents of the coal samples containing Mg-bearing clay minerals (illite, I/S mixed-layer clay minerals, smectite, K-smectite, and/or chlorite) were closely related.

The frequencies of mineral occurrences in the coal samples (see Table 1)

suggests that Mg is primarily associated with carbonate minerals and to a lesser extent associated with Mg-bearing clay minerals (Fig. 3). Most of the Ca exists in calcite and ankerite, although some occurs in apatite, dolomite and plagioclase. The great abundance of ankerite resulted in a comparatively high correlation coefficient (0.63) between Ca and Mg. Most of the coal samples contained less than 1.5% Ca and less than 0.2% Mg (Fig. 4).

The average Ca, Mg and Fe contents in the coal samples containing only calcite and ankerite as the Ca-, Mg-, and/or Fe-bearing minerals are 0.895% (29 samples), 0.097% (45 samples), and 0.290% (43 samples) respectively. Both the Ca and Mg contents of these coal samples are estimated to be approximately the same as those in recent plants (8). However, the Fe content is higher in these coal samples than those in recent plants and approximately the same as those in recent peats (8). This result implies that Ca, Mg and Fe in both calcite and ankerite could originate from the organic materials of plants and peats.

The coal samples have been classified based on their Mg and Fe contents into three groups (Fig. 5): (1) samples plotting along the Fe-axis (solid circles), (2) samples distributed diagonally from the origin (diamonds) and (3) samples containing moderately increasing Fe content with increasing Mg content (open circles). Fe in the first group is mostly associated with pyrite. Siderite and ankerite were the Fe-bearing carbonate minerals in the second group with the exception of one coal sample, which contained dolomite instead of ankerite. Ankerite was the only Fe-bearing carbonate mineral found in coal samples from the third group. The slope of the Fe to Mg weight ratio of samples from the third group almost matched that in ankerite. The difference between the slopes of the second and third groups is due to the presence of siderite in the third group, proving that the siderite in the coal samples is Mg-bearing siderite.

Fe occurs both in carbonate minerals (ankerite and siderite) and Fe in pyrite, marcasite and iron sulfate minerals. The high correlation of Fe with S is caused by several samples which contained higher amounts of pyrite and iron sulfate minerals.

A substantial number of the coal samples were rich in both P and Sr (Fig. 6). P occurs as apatite and goyazite but Sr occurs only as goyazite. As P and Sr show a high correlation coefficient (0.92), these two phosphate minerals are thought to be of similar origin. A similar correlation between P and Sr was reported for Eastern Tennessee coals (4).

No close correlation between F and P was observed. Since the P content as goyazite is evaluated by Sr content, the P content as apatite can be evaluated by subtracting the P content as goyazite from the total P content. The relationship between P content as apatite and F content (Fig. 7) has a straight line, indicating that fluorapatite is present. Apatite is thought to exist mostly as fluorapatite since most of the coal samples contain enough F to form fluorapatite. The remainder of the F is believed to be organically bound.

The Cl content in the coal samples was less than 0.04%. Fig. 8 shows Na versus Cl. Both inorganic and organic Cl appear to exist although the total Cl content is low. The correlation coefficients of Cl for Na, the other silicate related elements and ash are relatively high, suggesting that a certain amount of inorganic Cl is included in the coal samples. The correlation coefficient between Na and Cl increased with increasing Na-bearing clay mineral (smectite and/or I/S mixed-layer clay mineral) content, suggesting that inorganic Cl was incorporated into the coal seams by these clay minerals. Since the minimum Cl content was around 0.01% as the Na content approaches 0 (Fig. 8), at least up to about 0.01% of the Cl appears to be organically bound.

CONCLUSIONS

The major inorganic elements studied in the coal samples from the Ashibetsu district have been classified with respect to mineral sources. Si, Al, K, Ti and Na are associated with silicate minerals. K occurs as an interlayer cation in clay minerals. Mg is mostly associated with carbonate minerals and partly with clay minerals. Most of the Ca exists as calcite and ankerite, although part of the Ca exists as apatite. Fe was primarily found in carbonate minerals and pyrite. A minor fraction of the Al was associated with goyazite and boehmite. P occurs as fluorapatite and goyazite and Sr also occurs as goyazite. F exists not only as fluorapatite, but also appears to be organically bound. Cl also appears to exist in both inorganic and organic forms. Inorganic Cl is thought to be incorporated into the coal seams by clay minerals.

REFERENCES

1. T. Kimura and M. Kubonoya, *Mining Geol.*, 41, 297-312(1991) (in Japanese).
2. T. Kimura and M. Kubonoya, *Resource Geol.*, 44, 419-428(1994) (in Japanese).
3. T. Kimura and M. Kubonoya, *Resource Geol.*, 45, 99-109(1995) (in Japanese).
4. L.A. Harris, H.E. Barrett and O.C. Kopp, *Int. J. Coal Geol.*, 1, 175-193(1981).
5. A.E. Dorsey and O.C. Kopp, *Int. J. Coal Geol.*, 5, 261-274(1985).
6. P.C. Lindahl and R.B. Finkelman, In *Mineral Matter and Ash in Coal*: K.S. Vorres, ed; ACS Sym. Ser. 301, Amer. Chem. Soc., Washington, DC, 61-69(1986).
7. G.O. Asuen, *Int. J. Coal Geol.*, 9, 171-186(1987).
8. D.J. Casagrande and L.D. Erchull, *Geochim. Cosmochim. Acta*, 1391-1394(1977).

Table 1 Frequency of mineral occurrence in coal samples containing less than 40% ash.

| Coal seam | -600 m L | | | | | -695 m L | | Total |
|-----------------------|-----------|-----------|-------|------------|------|-----------|------|-------|
| | Torakawa | Torashita | No.10 | Upper No.8 | No.8 | Torashita | No.8 | |
| | -sanshaku | | | | | -nishaku | | |
| Thickness (cm) | 165 | 156 | 105 | 366 | 71 | 115 | 452 | |
| Number of samples | 10 | 6 | 9 | 12 | 8 | 9 | 20 | 74 |
| Silicates | | | | | | | | |
| Quartz | 10 | 5 | 8 | 10 | 8 | 8 | 14 | 63 |
| Plagioclase | 9 | 0 | 1 | 0 | 1 | 0 | 1 | 12 |
| Kaolinite | 10 | 6 | 9 | 12 | 8 | 9 | 19 | 73 |
| Illite | 1 | 0 | 0 | 4 | 2 | 1 | 1 | 9 |
| Illite/smectite mixed | 5 | 0 | 0 | 4 | 2 | 1 | 1 | 13 |
| -layer clay minerals | | | | | | | | |
| Smectite | 5 | 0 | 1 | 0 | 0 | 0 | 0 | 6 |
| K-smectite | 6 | 0 | 2 | 0 | 0 | 0 | 0 | 8 |
| Chlorite | 0 | 0 | 0 | 0 | 0 | 1 | 0 | 1 |
| Carbonates | | | | | | | | |
| Calcite | 9 | 6 | 9 | 3 | 8 | 8 | 19 | 62 |
| Aragonite | 0 | 0 | 0 | 0 | 3 | 0 | 0 | 3 |
| Ankerite | 6 | 3 | 9 | 6 | 7 | 3 | 19 | 53 |
| Siderite | 2 | 2 | 0 | 2 | 3 | 1 | 5 | 15 |
| Dolomite | 0 | 0 | 0 | 3 | 0 | 0 | 0 | 3 |
| Sulfides | | | | | | | | |
| Pyrite | 0 | 6 | 2 | 1 | 0 | 4 | 5 | 18 |
| Marcasite | 0 | 1 | 0 | 0 | 0 | 0 | 0 | 1 |
| Sulfates | | | | | | | | |
| Gypsum | 0 | 6 | 2 | 0 | 0 | 0 | 1 | 9 |
| Melanterite | 0 | 1 | 0 | 0 | 0 | 0 | 1 | 2 |
| Szomolnokite | 0 | 0 | 0 | 0 | 0 | 0 | 1 | 1 |
| Conquinbite | 0 | 0 | 0 | 0 | 0 | 0 | 1 | 1 |
| Roemerite | 0 | 0 | 0 | 0 | 0 | 0 | 1 | 1 |
| Hydronium jarosite | 0 | 0 | 0 | 0 | 0 | 0 | 1 | 1 |
| Phosphates | | | | | | | | |
| Apatite | 8 | 1 | 5 | 8 | 5 | 6 | 13 | 46 |
| Goyatzite | 2 | 0 | 0 | 5 | 3 | 3 | 4 | 17 |
| Boehmite | 1 | 0 | 0 | 1 | 5 | 5 | 12 | 24 |

Table 2 Correlation coefficients for coal samples containing less than 40% ash.

| | Si | Al | K | Ti | Na | Mg | Fe | Ca | Sr | P | Cl | F | S |
|-----|------|------|------|------|------|------|------|------|------|------|------|-------|-------|
| Ash | 0.96 | 0.72 | 0.75 | 0.64 | 0.61 | 0.31 | 0.08 | 0.25 | 0.15 | 0.25 | 0.49 | 0.01 | 0.08 |
| Si | | 0.61 | 0.72 | 0.57 | 0.58 | 0.25 | 0.09 | 0.18 | 0.03 | 0.11 | 0.49 | 0.02 | 0.05 |
| Al | | | 0.77 | 0.83 | 0.58 | 0.05 | 0.09 | 0.11 | 0.43 | 0.50 | 0.38 | 0.15 | 0.04 |
| K | | | | 0.68 | 0.62 | 0.16 | 0.12 | 0.05 | 0.08 | 0.20 | 0.45 | 0.07 | 0.13 |
| Ti | | | | | 0.48 | 0.00 | 0.00 | 0.07 | 0.24 | 0.41 | 0.38 | 0.18 | 0.07 |
| Na | | | | | | 0.16 | 0.13 | 0.03 | 0.12 | 0.22 | 0.66 | 0.26 | 0.13 |
| Mg | | | | | | | 0.26 | 0.63 | 0.15 | 0.13 | 0.11 | -0.23 | 0.17 |
| Fe | | | | | | | | 0.11 | 0.19 | 0.15 | 0.20 | -0.17 | 0.81 |
| Ca | | | | | | | | | 0.09 | 0.17 | 0.12 | -0.17 | 0.02 |
| Sr | | | | | | | | | | 0.92 | 0.18 | 0.22 | 0.11 |
| P | | | | | | | | | | | 0.28 | 0.29 | 0.07 |
| Cl | | | | | | | | | | | | 0.42 | 0.24 |
| F | | | | | | | | | | | | | -0.17 |

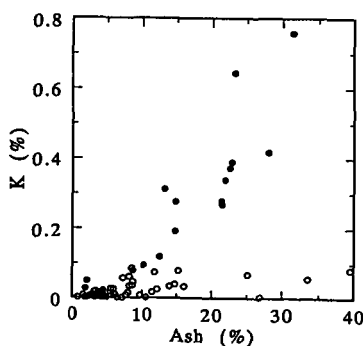


Fig.1 Relationship between ash and K contents. Solid circle=coal samples containing K-bearing clay minerals.

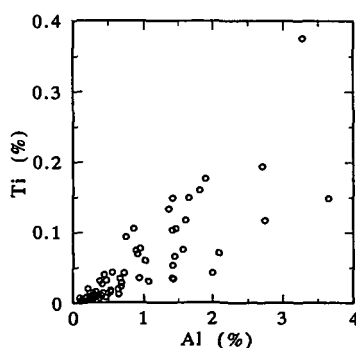


Fig.2 Relationship between Al and Ti contents.

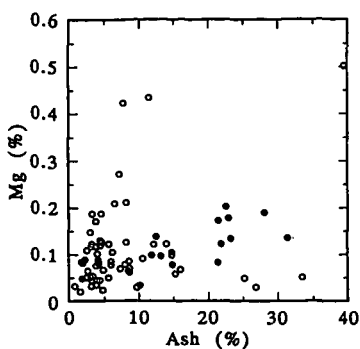


Fig. 3 Relationship between ash and Mg contents. Solid circle=coal samples containing Mg-bearing clay minerals.

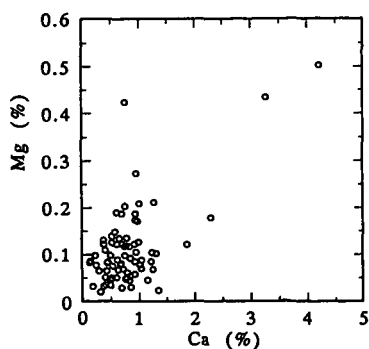


Fig. 4 Relationship between Ca and Mg contents.

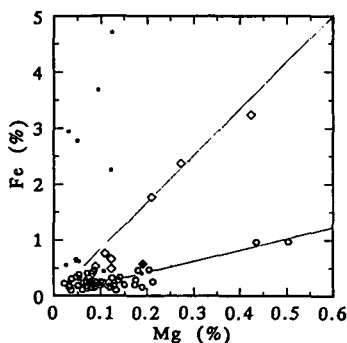


Fig. 5 Relationship between Mg and Fe contents. Solid circle, diamond, solid diamond, open circle=coal samples containing pyrite, both siderite and ankerite, both siderite and dolomite, and ankerite, respectively.

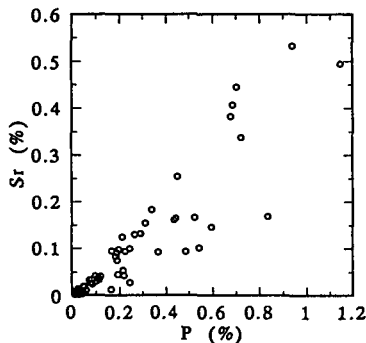


Fig. 6 Relationship between P and Sr contents.

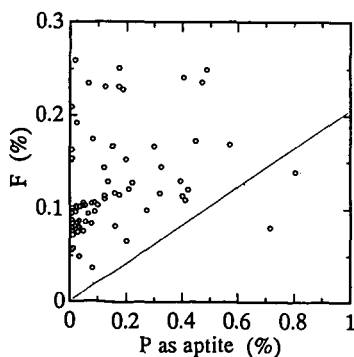


Fig. 7 Relationship between P content as apatite and F content. Solid line =F/P weight ratio of fluoroapatite.

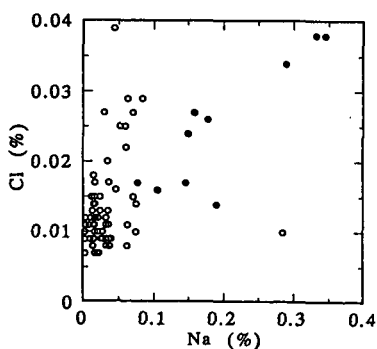


Fig. 8 Relationship between Na and Cl contents. Solid circle=coal samples relatively rich in Na-bearing clay minerals.

Bengt-Johan Skrifvars, Rainer Backman, Mikko Hupa,
Åbo Akademi University, Combustion Chemistry Group
FIN-20520-Turku, Finland

Keywords: Ash chemistry, ash sintering, melt behavior calculations

INTRODUCTION

The thermal behavior of a fuel ash is one important factor to consider when fireside slagging and fouling problems in steam boilers are addressed. It is well known that different types of chemical reactions and melts in deposits play an important role in the build-up of problematic fireside deposits.

Low viscous melts occur in steam boilers mainly when salt mixtures are present in the ash. Such are different mixtures of alkali and earth alkali sulfates, chlorides and carbonates. These mixtures do not melt at a certain temperature but form a melt in a temperature range which in some cases may be several hundreds of degrees. The amount of melt is crucial for the deposit build-up. For some boilers it has been found that roughly 10 - 20 weight-% melt in an ash mixture would be enough to cause extensive deposit formation, while 60 - 80 weight-% melt would already cause the ash to be so wet it would flow down a vertical tube and not cause any further deposit growth [1].

Another type of melt that causes deposits is the highly viscous silicate melt which occurs when silicon is present in the system. This type of melt causes mainly slagging problems in pulverised fuel fired boilers using coal or peat as fuel, but may occur also in fluidised bed boilers when quartz is used as the bed material. The silicate melts are problematic also because of their capability to form glassy phases which do not crystallize when the temperature decreases back below their first melting points. Viscous flow sintering of glassy silicate particles may cause extensive fouling. The amount of the formed melt and its viscosity are two important factors to consider when looking at viscous flow sintering, besides those parameters expressed in the Frenkel equation [2].

Also chemical reactions may cause hard deposits [3]. Calcium is one element which has been found very active in this sense. If it arrives in the oxide form to a surface it has been found to cause extensive deposit build-up if it reacts with $\text{SO}_2(\text{g})$ or $\text{CO}_2(\text{g})$ at the surface.

When studying these phenomena one has to take the chemistry into consideration since these above mentioned mechanisms are all strongly dependent on which elements you have present in the deposit, as which component and in which surrounding gas phase they are placed.

In this paper we present some initial thermal behavior predictions made for 10 different ashes which have been studied in a broader project. In this project both laboratory scale testing, as well as theoretical tools were used for establishing the thermal behavior of the ashes. In this paper we wanted especially to focus on the prediction of molten phases in the ash and compare these with sintering tests performed on the same ashes.

EXPERIMENTAL

10 different ashes were chosen for the tests. These are presented in Table 1.

The ashes were characterized in three different ways. Firstly, they were analysed quantitatively, secondly, they were sintering tested with a compression strength test and thirdly, they were analysed with a combined differential thermal - thermogravimetric analyser (DT/TGA). Details of these results are presented elsewhere [4].

The quantitative wet chemical analyses were re-calculated to components using stoichiometrical assumptions and thermodynamic considerations. The calculations assumed that all phosphorus was present as calcium phosphate, carbonate as both potassium and calcium carbonate, rest calcium as oxide, all chlorine as potassium chloride, sulfur as both sodium and potassium sulfate, rest potassium as oxide and all silicon as quartz. Rest of analysed elements were assumed as their oxides and unanalysed elements (differences to 100% oxides) as unknown.

After this we calculated the melting behavior of the ashes using multi-component, multi-phase thermodynamic calculations and compared the results with the sintering test results we had achieved earlier in the study. In the melting behavior calculations we treated the ashes as if they would have consisted of four separate parts, one salt part consisting of the alkali sulfates, carbonates and chlorides (referred to as alkali salts in the further text), another silicate part consisting of the elements expressed as oxides, a third part consisting of calcium oxide and carbonate and a fourth part consisting of the phosphate and unknown elements.

Of these four parts, the silicates and salts were assumed to be those causing melt formation, while the calcium oxide/carbonate part would be active to react with flue gases and the inert part wouldn't affect deposit at all.

RESULTS

The results from the sintering tests are summarized in Figure 1. The results revealed significant differences in the sintering tendencies such as they were detected by the compression strength test. The temperatures at which the strength of the pellets started to increase varied from 625°C (ash #8) to above 1000°C (ash #7).

In Figure 2 the estimated amounts of different components present in the ash is shown. Focusing on the silicate and salt parts in the ash, one sees that the ashes #1 to 6 are fairly rich in silicates, while the ashes #7 to 10 are very rich in calcium oxide/carbonate with low amounts of silicates. The salt part varies significantly, from roughly 1% by weight for the ash #3 to 44% by weight for the ash #8.

Figure 3 summarises the results from the melting behavior calculations. The results are presented as the amount of melt, expressed as percentages by weight in the sample vs the temperature. The melting of the silicate part and salt part are treated and expressed separately in the figure. The calcium oxide/carbonate and the inert parts are added up to the total amount (100%).

Ash #1 reaches its first melting point, T_0 , already at 525°C. At this temperature a very small amount of alkali salt forms a melt which is approximately 1/10 of a percent of the total ash. The amount of melt stays low throughout the calculated temperature range. At 770°C the silicate part in the ash reaches its T_0 , forming immediately some 17% melt, causing the total amount of melt to increase to 19% melt in the ash. From here on the amount of melt increases very slowly with temperature to reach its maximum, 19% melt, at 1200°C. At this temperature the salt part contributes to the melt with only 3.5% by weight.

Ash #2 reaches its T_0 at 615°C. At this point the alkali salt part of the ash forms a small amount of melt. As the temperature increases to 750°C, the whole alkali salt part has become molten, the amount being 14% by weight. At 770°C the silicate part forms a 15% melt, the total amount being now 29% melt in the ash. From here on the silicate part continues to melt, ending up at 36% total melt in the ash at 1200°C.

Ash #3 forms a large amount of silicate melt at 770°C. At this point 35% of the ash is found in the molten phase. At 845°C the alkali salt part starts to contribute to the melt formation. At 895°C all the alkali salts have melted, the total amount of melt now being 55%. This amount increases still and reaches the maximum value of 65.6% melt in the ash at 1200°C.

Ash #4 forms an alkali salt melt at 625°C. At 770°C also the silicate part starts to melt, almost doubling the total amount of melt from 17% to 30%. The amount increases to about 33% at 810°C after which the increase slows down, however, still increasing the melt part to 40% which is reached at 1200°C.

Ash #5 forms also a first alkali salt melt at 625°C. The amount increases immediately to 15%. At 765°C the whole alkali salt part is molten, forming some 30% molten phase in the ash. At this same temperature the silicate part starts to melt, forming roughly 20% molten phase immediately. This increase the total amount of melt to 50% at this temperature. The amount increases still up to the maximum temperature 1200°C at which 57% of the ash has molten.

Ash #6 forms a very small amount of alkali salt melt already at 530°C. The amount stays very low (below 5%) throughout the calculated temperature range. At 780°C the silicate part starts to melt. The amount is up to some 1000°C low, but increases above 1000°C rapidly to reach its maximum of some 35% silicate melt at 1040°C. The total amount of melt is at this temperature 38% and does not exceed that number in the calculated temperature range.

The rest of the ashes, i.e. #7, 8, 9 and 10 form only alkali salt melts. Ash #7 has a T_0 of 575°C. The amount stays low to approximately 800°C and does not exceed the value of 20% in the whole calculation range. Ash #8 forms a first melt of roughly 20% at 615°C. The amount continues to increase until the temperature reaches the value of 760°C. At this point 45% of the ash is molten. After this the amount does not increase anymore. Ash #9 behaves somewhat like ash #7, i.e. a T_0 of 535°C with a low amount of melt formed, up to a temperature of roughly 750°C, where the amount starts to increase up to the maximum value of 25% which is reached at 810°C. Ash #10 forms a first melt at 870°C. At this temperature the alkali salt part melts almost completely and forms a 25% melt of the total ash.

DISCUSSION

Comparing the sintering tendencies for the ashes #2, 5, 6, and 8 with the melting behavior calculations one finds fairly good correlations between the T_{20} temperature, i.e. the temperature where 20% of the ash is molten and the sintering temperatures, T_{smt} . For the ash #2 the T_{smt} is between 700° and 750°C, the T_{20} is 770°C. For the ash #5 the T_{smt} is between 650° and 675°C, and the T_{20} is 700°C. For the ash #6 the T_{smt} is between 950° and 1050°C, and the T_{20} is 1025°C and for the ash #8 the T_{smt} is between 625° and 650°C, the T_{20} being 625°C. In all these cases the melt probably caused the strength increase in the ash pellets tested. In the case with ashes #2 and 6 it seems probable that it was the silicate melt that caused the sintering, while it for the ashes #5 and 8 seemed to be the alkali salt melt causing the sintering.

For the ash #3 the compression strength test indicates sintering to start at roughly 800°C. The melting behavior calculations suggest, however, a significant melt formation already at 770°C, i.e. the melt behavior calculations overpredict the sintering. The viscosity of the formed melt may explain the temperature difference found when comparing the T_{20} to the T_{smt} . If we assume that the formed melt had a high viscosity, the time for the sintering caused by that glassy phase would have been longer than that for a low viscous glassy phase, indicating that the sintering measurements were not done long enough. In these tests 4 hours were used as the standardized sintering time. No viscosity measurements were, however, done at this stage.

For the ash #1 the melting behavior calculations suggest a molten phase below 20% from 770°C throughout the calculated temperature range. Some sintering was detected beyond 900°C. Since most of the formed melt for the ash #1 throughout the calculated temperature range was a silicate melt the viscosity of that may again explain the sintering. No viscosity calculations were however done.

For the ashes #7, 9, and 10 the melting behavior calculations predict melts up to roughly 20% of the total ash from 800°C for the ash #9, 850°C for the ash #7, and 880°C for the ash #10. For the ashes #9 and 10 a fairly good correlation can be seen between the T_{20} and the T_{smt} but for the ash #7 the sintering temperature and the melting behavior calculation does not correlate at all. In this cases no sintering was detected in the tested conditions. Obviously the component estimations presented in Fig. 2 fail in this case. The ash #7 contains fairly large amounts of analysed carbonate (expressed as CO_2 in Tab. 1). The melts predicted for this ash was all alkali salt melts, with potassium carbonate as the main component. If we assume that no potassium carbonate is present in the ash (all analysed CO_2 as calcium carbonate instead), the alkali salt part would decrease to 1/10 of its amount and hence, no large amount of melt could form.

For ash #4 the melt behavior calculations do not correlate well with the sintering measurements. The alkali salt part of the ash reaches its complete melting temperature T_{100} at 820°C, at which also most of the silicate melt to be formed is present. At this point roughly 35% of the ash should be molten. The sintering, detected by the compression strength test, does not, however, indicate any significant strength increase until 950°C. No clear explanation could be found for this behavior.

CONCLUSIONS

Silicate and salt melts may cause extensive deposit formation in steam boilers. The formation of these kind of melts can today be calculated with fairly acceptable accuracy, using multi-component, multi-phase thermodynamic equilibrium calculation. Good knowledge of which components are present in the ash and accurate thermodynamic data is, however, required.

Of ten ashes tested in laboratory conditions and predicted for their melting behavior, for six ashes the melt behavior calculations correlated well with the measured behavior. For the ashes #5, 8, 9, and 10 the alkali salts formed the major part of the melt while it for the ashes #2 and 6 seemed to be the silicate melt that caused the strength increase.

In two cases, for the ashes #1 and #3 the melt behavior calculations predicted a somewhat lower temperature for T_{20} than for T_{smt} . In these cases the calculations predicted a viscous silicate melt to be formed as the major phase. A possible cause for the higher T_{smt} may have been a high viscosity in the silicate melt, causing so slow sintering that the compression strength test didn't have time to detect it.

In the rest of the cases (two ashes) the melt prediction calculations seemed to fail to predict the sintering behavior detected by the compression strength test. A possible reason to this failure is errors in the assumed components used in the calculations.

REFERENCES

- [1] Backman, R., Hupa, M., Uppstu, E.: Tappi J. 70 (6), 123 (1987).
- [2] Frenkel, J. J.: Physics USSR 9 (5), 385 (1945).
- [3] Skrifvars, B.-J., Hupa, M., Hyötty, P.: J. Inst. Energy, 64 (461), 196 (1991).
- [4] Skrifvars, B.-J., Hupa, M.: Characterization of biomass ashes, presented at the Engineering Foundation Conference on "Applications of Advanced Technology to Ash-related Problems in Boilers", July 1995, Waterville Valley, New Hampshire, USA.

Table 1. The ash analyses of the studied fuels, expressed as weight-% of their corresponding oxides.

| # | SiO ₂ | Al ₂ O ₃ | Fe ₂ O ₃ | P ₂ O ₅ | CaO | MgO | Na ₂ O | K ₂ O | SO ₃ | CO ₂ | Cl |
|----|------------------|--------------------------------|--------------------------------|-------------------------------|------|------|-------------------|------------------|-----------------|-----------------|-----|
| 1 | 65.7 | 1.7 | 1.4 | 5.0 | 2.7 | 1.8 | 0.3 | 4.6 | 1.4 | 0.0 | 0.2 |
| 2 | 56.3 | 0.5 | 0.6 | 1.9 | 6.3 | 1.4 | 0.2 | 12.6 | 2.9 | 1.3 | 2.1 |
| 3 | 48.8 | 6.4 | 1.9 | 3.0 | 3.9 | 5.5 | 0.8 | 18.9 | 3.5 | 3.1 | 0.0 |
| 4 | 44.1 | 5.1 | 2.3 | 2.1 | 6.7 | 3.6 | 0.3 | 16.0 | 5.2 | 1.9 | 1.8 |
| 5 | 34.2 | 0.4 | 0.5 | 2.1 | 9.1 | 2.0 | 0.1 | 24.7 | 2.3 | 6.1 | 3.2 |
| 6 | 34.0 | 4.7 | 4.4 | 3.0 | 17.3 | 11.4 | 0.4 | 17.1 | 1.2 | 0.5 | 0.5 |
| 7 | 7.3 | 1.5 | 1.3 | 4.8 | 44.8 | 5.8 | 0.8 | 11.3 | 1.5 | 5.2 | 0.0 |
| 8 | 3.3 | 0.3 | 0.3 | 7.6 | 27.7 | 3.1 | 0.7 | 28.4 | 1.9 | 22.3 | 4.4 |
| 9 | 0.6 | 0.3 | 0.3 | 6.0 | 35.1 | 10.4 | 2.3 | 13.6 | 2.0 | 27.6 | 0.3 |
| 10 | 0.6 | 0.1 | 0.7 | 10.7 | 28.8 | 4.4 | 0.2 | 22.5 | 5.9 | 23.5 | 0.2 |

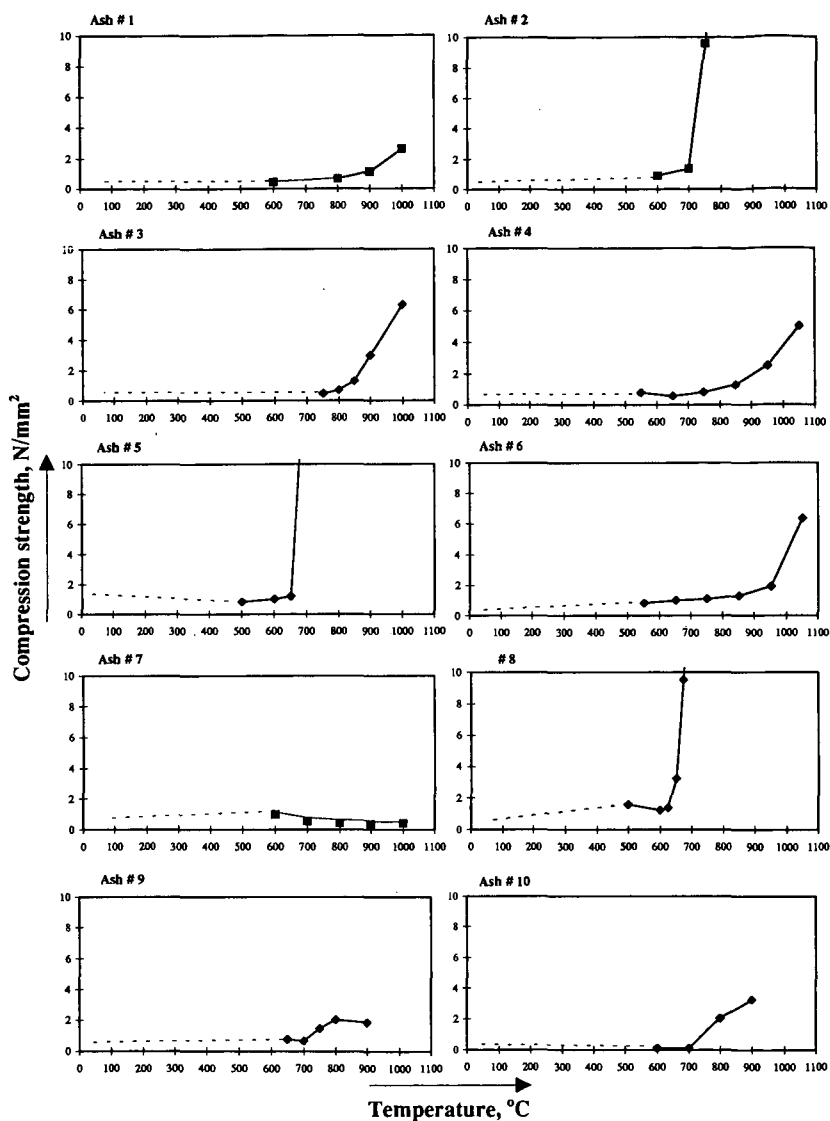


Figure 1. Sintering tendency for ten ashes, tested with the compression strength sintering test. O-tests indicated in the left corner of each figure. Sintering time 4h, dry air atmosphere.

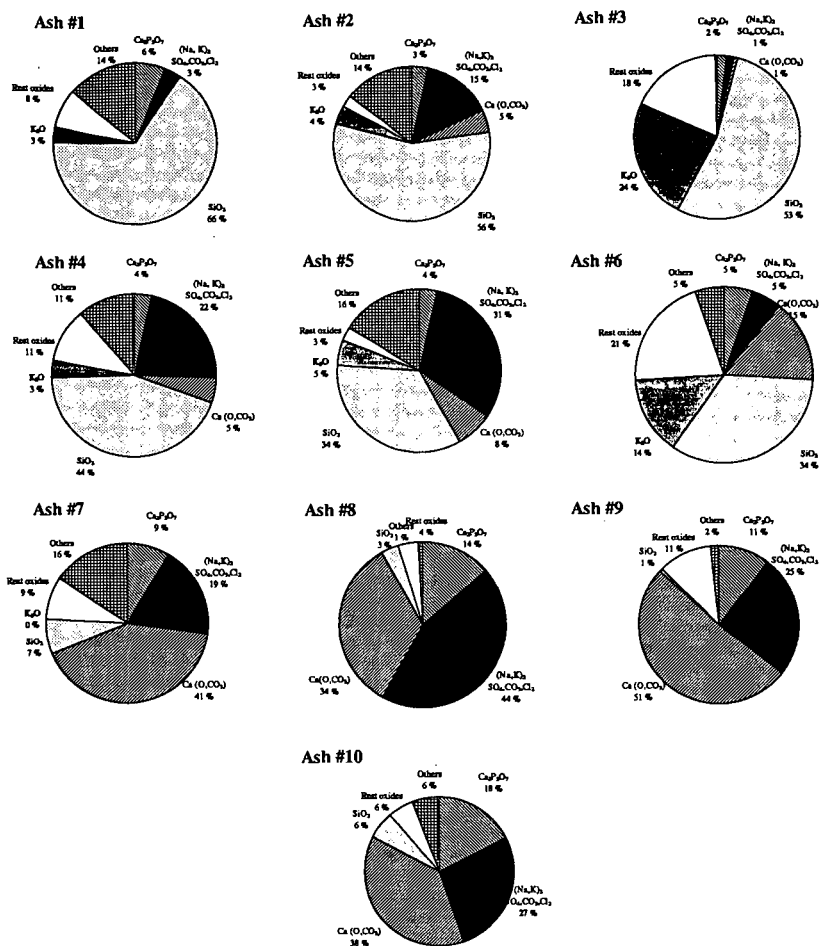


Figure 2. Stoichiometrically estimated amounts of different components (weight-%) present in the 10 ashes, presented in Table 1. The calculations assume that all phosphour is present as $\text{Ca}_3\text{P}_2\text{O}_7$, carbonate as both K_2CO_3 and CaCO_3 , rest calcium as CaO , all chlorine as KCl , sulfur as both Na_2SO_4 and K_2SO_4 , rest potassium as K_2O , all silicate as SiO_2 , rest analysed elements as oxides and un-analysed elements as others.

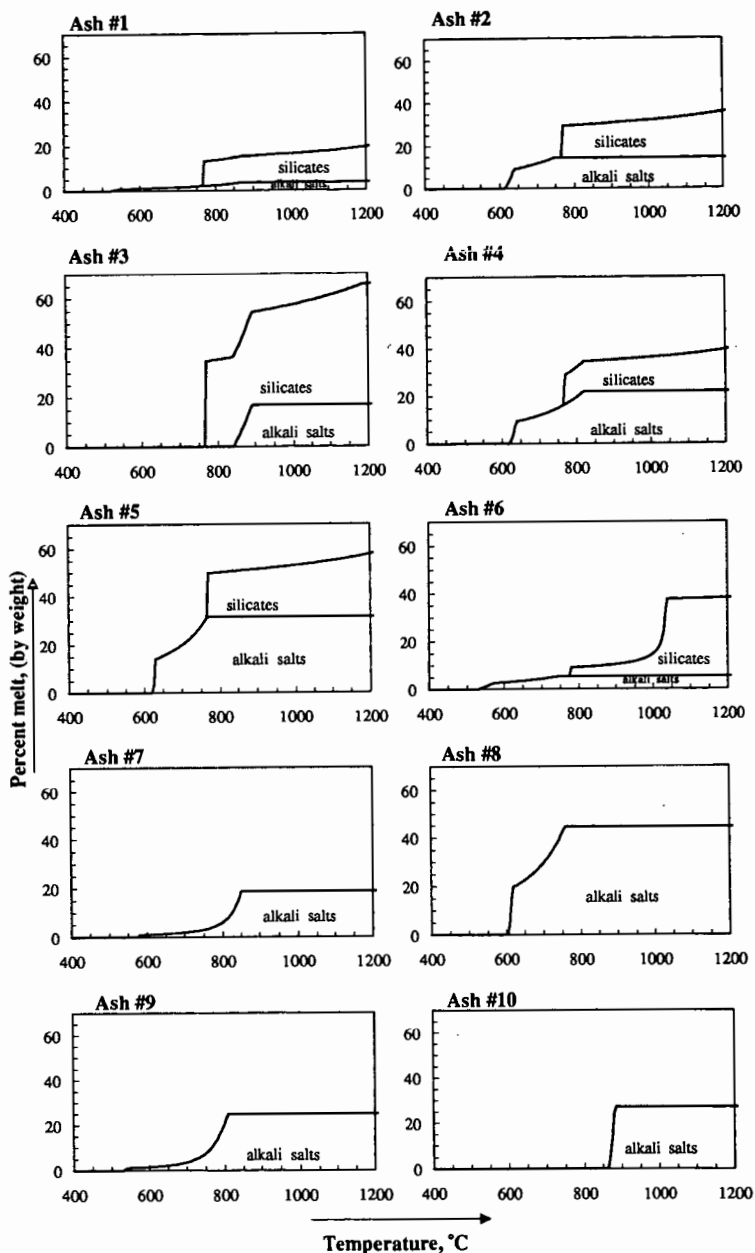


Figure 3. The melting behavior calculations, based on the components presented in Figure 2.

ASH FUSION TEMPERATURES AND THE TRANSFORMATIONS OF COAL ASH PARTICLES TO SLAG

S. Gupta, T.F.Wall, R.A.Creelman and R.Gupta

Department of Chemical Engineering

University of Newcastle, Callaghan, NSW 2308, Australia

Keywords: Ash fusion, viscosity and shrinkage.

ABSTRACT

A mechanistic study is detailed in which coal ash is heated with its shrinkage measured continuously up to a temperature of 1600°C. The temperatures corresponding to the rapid rate of shrinkage are shown to correspond to the formation of eutectics identified on phase diagrams. Samples were therefore heated to these temperatures, cooled rapidly and examined with an SEM to identify the associated chemical and physical changes. The progressive changes in the range of chemical analysis (from SEM), the extent of undissolved ash particles and porosity were then quantified and related to homogenisation, viscosity and ash fusion mechanisms.

INTRODUCTION

Ash deposition on furnace walls in pf (pulverised fired) furnaces is called slagging when it occurs in the high temperature areas of furnaces directly exposed to flame radiation and fouling in other regions such as tubes in the convection section of the boiler. The characterisation of coal ash for its tendency to slag and foul has been traditionally related to the bulk chemistry of the ash and ash fusion temperatures. There are well-documented shortcomings of these approaches relating to their uncertainties as predictive tools for plant performance, that is, poor repeatability and reproducibility of ash fusion measurements. Of particular concern is the estimation of the initial deformation temperature (IDT). IDT is the temperature at which the rounding of the tip of an ash cone is noted, which has been accepted as the temperature where the ash first softens and therefore becomes sticky. The nature of physical and chemical changes occurring during melting of coal ash has been investigated in the current study to provide an alternative procedure to the ash fusion test. The characteristic melting temperatures then are related to the transformations, and reactions of ash and these are interpreted in terms of their importance to fouling and slagging in furnaces.

EXPERIMENTAL

The current study is based on a range of samples selected from domestic power stations to those exported from Australia as steaming coals. Several export coals were selected on the basis of difficulty of the estimation of their IDT's. Laboratory ash was prepared for all the samples and ashes from some of the corresponding power stations were also obtained. Different laboratories reported a wide variation in IDT estimation, the difference being as great as 400°C in some cases.

Several techniques have been tried to investigate the fusibility of bituminous ashes in a related study as detailed elsewhere (Wall et al., 1995). The major events observed in these techniques are illustrated in Figure 1. The top two plots in Figure 1 are based on the HRL Test (Ellis, 1989). The electrical resistance and shrinkage of compacted ash pellets are recorded concurrently from room temperature to about 1350°C in this test. The third plot indicates the shrinkage of compacted ash pellets sandwiched between two tiles as developed at ACIRL (Coin, et al. 1995). The last plot is based on the TMA (thermomechanical analysis) technique developed by the CSIRO Division of Coal and Energy Technology. The current paper will be restricted to results obtained from the last technique.

TMA Technique (Thermomechanical Analysis)

Shrinkage measurements are frequently used in metallurgy and ceramic science to study the physical properties at high temperatures. Raask(1979), Ellis(1989), Lee(1991), Gibson(1991) and Sanyal(1993) have studied electrical resistance and shrinkage properties for sintering and fusion characteristics of ashes in the past. However, a systematic study comprising several types of measurements, laboratory ash and combustion ash with investigations of fusion mechanisms for temperatures up to 1600°C has been lacking. TMA technique involves measurements of the shrinkage of loose ash (~35mg.) in a specially designed sample holder which is located between a cylindrical graphite container with a flat bottom and a rod with a tapered end. As the assembly (ash) is heated from room temperature to 1600°C, the rod sinks into the ash and when eventually flows as slag into the annular gap between the rod and the container. The samples were heated in neutral environment as per AS (Australian Standards) requirements. The output of this experiment provides 3 to 4 'peaks' (maximum rate of shrinkage with temperature) of different intensity and at different temperatures which are related to melting characteristics of the sample as shown in Figure 1. There is no significant shrinkage in most of the samples below 900°C. The temperatures associated with particular shrinkage levels were noted as T(x%).

Studies to Identify Transformations

Compacted ash pellets were heated under standard AS reducing conditions and rapidly quenched in air to freeze the samples. The chemical composition of liquid phases and slags were determined from sectioned samples of these pellets using a scanning electron microscope (SEM) and electron dispersive spectrum (EDS). Micrographs of the samples were also obtained to compare the porosity and extent of undissolved particles. Bulk density of some of the samples has also been measured at different temperatures.

RESULTS

Mechanism of Ash Fusion

The current observations are based on twenty nine samples. Most of the samples can be grouped into four categories, and represented by particular samples as follows: i) ash with a high SiO₂/Al₂O₃ ratio, low Fe₂O₃ and poor reproducibility for the IDT e.g. EN3; ii) ash with a SiO₂/Al₂O₃ ratio within the norm of Australian coals, low Fe₂O₃, and very poor reproducibility for the IDT e.g. EN6; iii) ash with high Fe₂O₃(11%) e.g. EQ1 with good reproducibility and iv) ash with high CaO(16%), e.g. ET2 with good

reproducibility for the IDT. TMA measurements provided 'peaks' identifying rapid fusion events during heating. These 'peaks' have been related to formation of eutectics identified on appropriate phase diagrams (Wall, et al., 1995). Shrinkage results demonstrated occurrence of the peaks in three distinct groups. Lower temperature peaks up to 1100°C were related to eutectics in SiO_2 - Al_2O_3 - K_2O system and 1200°C peaks to SiO_2 - Al_2O_3 - FeO system. Peaks in the range 1220°C to 1440°C have been correlated to FeO and CaO reactions with various proportions of SiO_2 and Al_2O_3 .

Homogeneity and Porosity of Samples:

The melt composition will change continuously with temperature till ash is transformed completely to a homogeneous liquid. The chemical composition of slag should then be of the bulk ash. The melt composition was determined for at least 10 points per sample at one temperature using SEM and EDS mode. Major variation in the melt composition is due to different extent of dissolution of silica particles. SiO_2 (wt.%) concentration in the melt has been selected to illustrate the homogenisation of liquid phase. SiO_2 in melt reaches to bulk ash composition rapidly in high iron sample EQ1 as shown in Figure2, where the FN3 and EN6 melt approach to the bulk ash composition at a higher temperature.

Ternary diagrams have also been used for describing the change in melt composition. The chemical composition from point analysis was normalised to three component system i.e. SiO_2 - Al_2O_3 - CaO for ET2 and SiO_2 - Al_2O_3 - FeO for other samples. The normalised analyses of EN6, EQ1 and ET2 are presented on ternary diagrams of SiO_2 - Al_2O_3 - FeO and SiO_2 - Al_2O_3 - CaO as shown in Figure3. EQ1 and ET2 melt composition range narrows to that of bulk ash at lower temperatures as compared to EN6 (Figure3). CaO appears to be most important constituent for rapid homogenisation at various stages.

At low temperatures diffusion rates are slow therefore melt formation proceeds slowly. As the ash is heated open pore network transforms to micropores and a minimum porosity. Melting and reaction occurs to form the first liquid phase that has a composition close to iron cordierite. This liquid may start flowing to fill the open network and hence contribute to initial densification. The reaction of this melt phase with specific solids (SiO_2 rich) until progressive depletion of the solids occurs and finally slumping of the pellets as the proportion of the liquid increases significantly. Air entrapped in the sample causes pore formation. It was observed that pore formation increases with iron content. Most of the porosity is either closed or in the form of spherical pores. Majority of the samples indicate that T(50%) (temperature corresponding to 50% shrinkage) is associated with closed and spherical pore structure. Gibson(1991) also observed similar trends. Bulk porosity keeps on decreasing till formation of closed pores takes place. Closed porosity is found to be increasing rapidly after T(50%) in most of the cases. The bulk density estimated from pellet dimensions also indicated that high alkali samples acquire minimum porosity at lower temperatures compared to high silica samples. It was also observed that temperatures corresponding to minimum porosity lie between 1200° to 1300°C. Physical changes before 50% shrinkage may depend on the permeability of liquid through the open porosity. After 50% shrinkage, the rate of shrinkage may depend on the rate of dissolution of residual silica in the melt (i.e. amount and particle size of quartz in the initial sample). Image analysis of electronmicrographs of various samples indicated less than 25% undissolved particles at T(50%).

AFT and Alternative Shrinkage Temperatures

The traditional AFT test involves observation of four temperatures (IDT, ST, HT and FT) depending on the physical state of the ash cone. Huffman(1981) observed that at IDT most of the melting is completed and it was also estimated that glass phase was more than 75%. Figure5 shows the linear shrinkage associated with IDT and some 'peak' temperatures. The first peak, i.e. first important fusion event in majority of the samples was observed around ~10% shrinkage of ash. The second peak occurred at <30% shrinkage of most of the samples, except for high iron and high CaO , which are associated with ~50% shrinkage at the second important event. It can be seen that IDT is associated with approximately ~50% shrinkage for EQ1 and ET2 samples of good reproducibility and around 60% for poor reproducibility samples e.g. EN3 and EN6 (Figure 4). The IDT clearly does not represent first shrinkage event.

The temperatures corresponding to these fusion events may be used for ash deposition characterisation. Figure 5 illustrates a ranking criteria for ash deposition based on temperature vs shrinkage plot for many samples. The samples requiring higher temperatures for a given shrinkage level are expected to be associated with least deposition, while those at the bottom are expected to be most troublesome. Hence ET2 (high CaO) would provide worst deposition, whereas PQ2(least alkali) should provide least deposition. However, the location of a particular sample within this ranking will depend on the temperature in different regions of the plant. In practical terms, this implies that ranking will depend on the temperature in different parts of the plant.

Correlation of shrinkage with ash viscosity, and sticky particles

The current understanding of the of the ash deposition is based on the stickiness of the particles. If the particles are sticky they will adhere to a surface on impact. Many studies have related stickiness to the viscosity of the particles which, in turn, has been calculated from the chemical composition. The viscosity calculated from the known composition of the ash samples therefore provides a basis for estimating theoretical temperatures for particles to be sticky, which can be related to the extent of shrinkage measured at these temperatures. Boni et al. (1990) suggested that ash particles with viscosity $>10^7$ Pas are not sticky and will not collect on the heat transfer surface. The sintering and slagging has also been related to viscosity of ash particles by Raask (1985). Figure 6 indicates the range of viscosity of the liquid slag generated from the ash samples which is calculated from the Urbain correlation (Urbain et al., 1981) based on the ash chemistry. This figure also provides the shrinkage range of importance to ash deposition. All ash samples fall within the viscosity range of 10^5 to 10^7 Pas at 25% shrinkage (Figure 7). Therefore it may be suggested that this shrinkage level is appropriate as criterion for ash stickiness. Examination of electronmicrographs from quenched samples also indicate the significant proportion of liquid phase

corresponding to these temperatures. It can be seen from this figure that ash particle impinging onto walls will be sticky at a similar temperature at which liquid formation has been observed in the pellets.

CONCLUSIONS

1. IDT clearly does not represent the first fusion event.
2. T(25%) is found to be associated with significant particle deformation.
3. T(50%) is related to formation of closed or spherical pores, which corresponds to >75% melt phase.
4. The temperatures corresponding to particular shrinkage events may be used as alternate ash fusion temperatures.

ACKNOWLEDGMENTS

We are most grateful to Mr. Dick Sanders of Quality Coal Consulting Pty. Ltd. for managing the project, selecting samples and providing insights into the AFT procedures. The study was supported by the Australian Coal Association Research Program with Mr. Grant Quinn of BHP Australia Coal as project monitor. The assistance of Dr. John Saxby at CSIRO is greatly appreciated.

REFERENCES

- Boni et al. (1990), Transformations of Inorganic Coal Constituents in Combustion System, DOE Report No. AC22 - 86PC 90751, March (1990).
- Coin, C., Reifenscin, A.P. and Kahraman H. (1995), Improved Ash Fusion Test, Engineering Foundation Conference on Application of Advanced Technologies to Ash - related Problems in Boilers, USA.
- Ellis, G.C. (1989), The Thermomechanical, Electrical Conductance and Chemical Characteristics of Coal Ash Deposits, NERDDP Project No. 1181 Final Report Volume III, SECV R & D Dept, Australia.
- Gibson, J.R. and Livingston, W.R. (1991), The Sintering and Fusion of Bituminous Coal Ashes, Engineering Foundation Conference on Inorganic Transformations and Ash Deposition During Combustion, Palm Coast, Florida.
- Huffman, P.G., Huggins F.E. and Dunmyre G.R. (1981), Investigation of the High Temperature Behaviour of Coal Ash in Reducing and Oxidising Atmospheres, Fuel, 60, 585-597.
- Lee, G.K. et al. (1991), Assessment of Ash Sintering Potential by Conductance and Dilatometry, Pittsburgh Coal Conference.
- Raask, E. (1979), Sintering Characteristics of Coal Ashes by Simultaneous Dilatometry - Electrical Conductance Measurements, J. Thermal Analysis 16, 91.
- Raask, E. (1985), Mineral Impurities in Coal Combustion, Hemisphere Publishing Corporation USA.
- Sanyal, A. and Mehta, A.K. (1994), Development of an Electrical Resistance Based Ash Fusion Test. The Impact of Ash Deposition in Coal Fired Furnaces, p445-460, Taylor and Francis, Washington.
- Urban G. et al. (1981), Trans. J. Br. Ceram. Soc., Vol. 80, p139-141.
- Wall, T.F. et al. (1995), Coal Ash Fusion Temperatures - New characterisation Techniques, and Associations with Phase Equilibria, Engineering Foundation Conference on Application of Advanced Technology to Ash - Related Problems in Boilers, New Hampshire, USA.

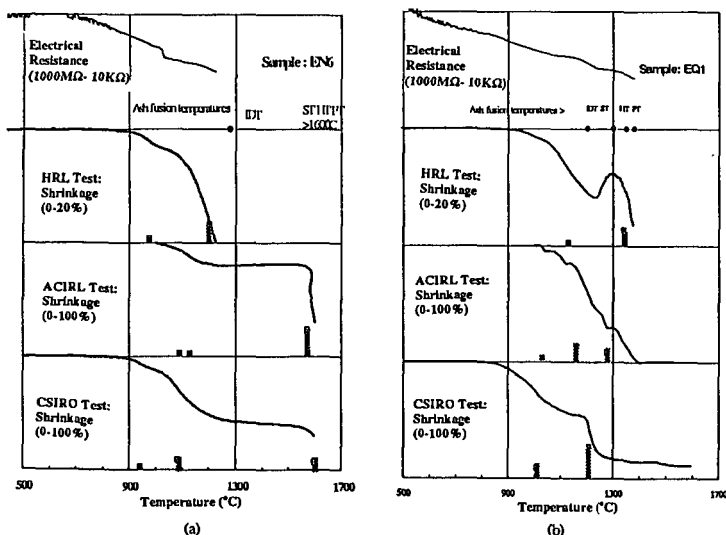


Figure 1. a) Sample EN6, comparison of the results for the techniques. Top plot - electrical resistance data from HRL test, bottom of three plots - shrinkage experiments reported as progressive ash sample linear dimension on heating. The bars indicate 'peak' temperatures of rapid change in ash sample heating. b) Sample EQ1.

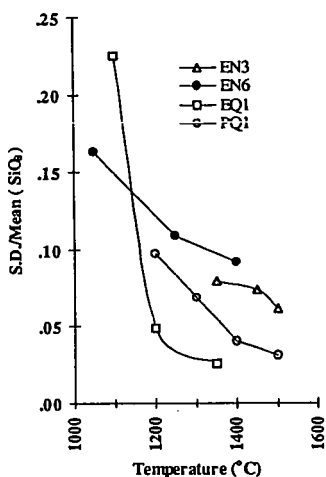


Figure 2. Variation in SiO_2 composition in melt phase, for different samples expressed as the standard deviation normalised to the mean.

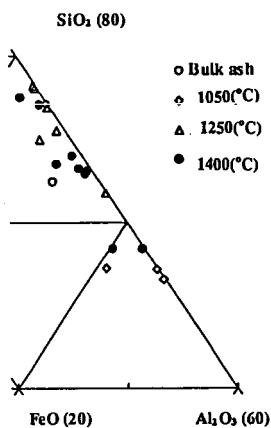


Figure 3(a)

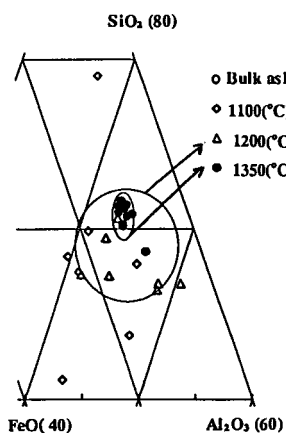


Figure 3(b)

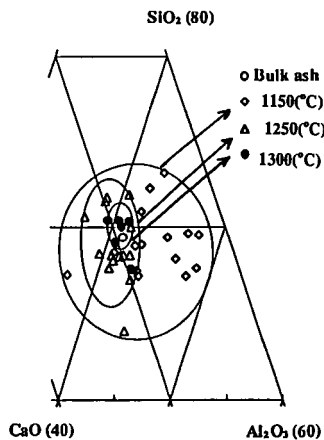


Figure 3(c)

Figure 3. Ternary plot for melt compositions for a) EN6, b) EQ1 and c) ET2.

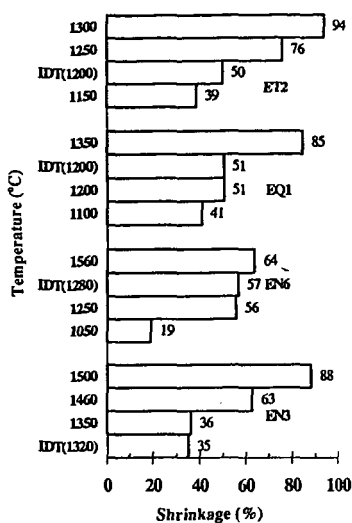


Figure 4. Shrinkage(%) at peak temperatures and IDT for samples EN3,EN6,EQ1 and ET2.

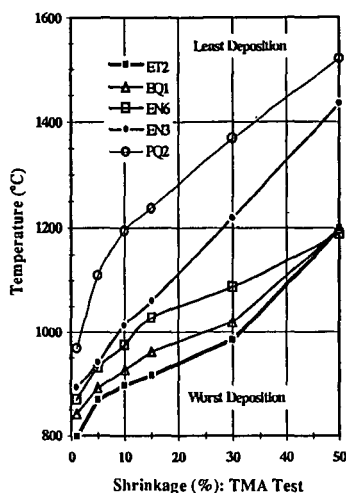


Figure 5. Relative sample ranking plot for ash deposition based on shrinkage(%) temperatures.

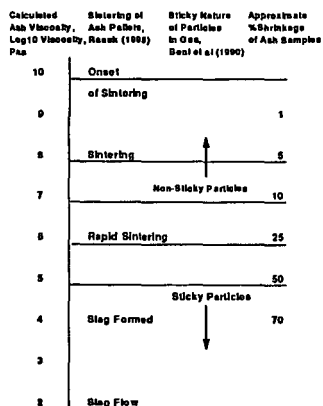


Figure 6. Association between physical state of ash, sintering and sticky nature of particles in the furnace.

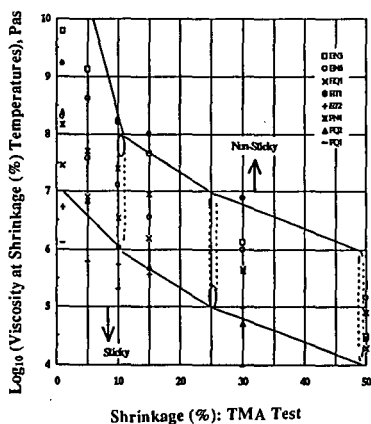


Figure 7. Correlation of calculated viscosity (Urbain' Model) and different levels of shrinkage with regions for sticky and nonsticky particles.

PHASE RELATIONSHIPS IN COAL ASH CORROSION PRODUCTS

DAVID KALMANOVITCH
DB RILEY, INC.
WORCESTER, MA

ABSTRACT

The corrosion of heat transfer surfaces in coal-fired utility boilers is a major concern to the efficient operation of these units. Despite the importance of the corrosion there has been limited research on the relationship between the ash components on the tube surface and the interactions and reactions between the various components and the steel surface. Mechanisms such as molten phase corrosion, sulfidation, and high temperature oxidation have been identified as leading to extensive wastage of tube metal. However, while the corrosion process can be identified using techniques such as metallography and x-ray diffraction there is limited insight into the role of the coal mineralogy and ash deposits on the surface in the corrosion process.

This paper describes research into the formation of molten or semimolten phases within ash deposits which are associated with corrosion of superheater and reheater fireside surfaces. For example, the phases potassium pyrosulfate ($K_2S_2O_7$) and potassium aluminum sulfate ($K_2Al_2SO_7$) have been determined by x-ray diffraction to be present in deposits where fireside corrosion has occurred. However, both these phases are not directly derived from coal minerals or the common matrix observed in ash deposits. The examination of the reactions and interactions within deposits which result in the formation of these and other phases associated with corrosion will be discussed in the paper.

INTRODUCTION

The high temperature corrosion of pressure parts in utility boilers is a major aspect of the design and operation of the system. The ideal design of heat transfer surfaces would be a material which would be resistant to creep damage and exhibit no corrosion. In reality the economics of boiler design requires the use of steels which are not only susceptible to creep damage (at temperatures above 650° C and pressures above 14 MPa) but also susceptible to corrosion. The corrosion is important as the reduction in wall thickness caused by the wastage results in reduced capacity to contain steam pressures, increased hoop stresses within the tube, and in reduced creep life. Therefore, it is very important that the corrosion process occurring on the fireside surface of heat transfer surfaces be understood and thereby reduced by either fuel choice or change in design/operating conditions.

The high temperature corrosion of heat transfer surfaces is usually observed in coal fired systems and confined to superheater and reheater components. In many cases the corrosion is localized to the tubing with the highest metal temperatures within the component such as the outlet portion. The metal temperatures in this location are either known or measured and are functions of unit design and operation. However, a knowledge of the metal temperatures is only a part of the issue with respect to the corrosion process. A major aspect is the reactions and interactions of the phases within the ash deposit and the relationship between these phases and corrosion processes.

The most aggressive form of fireside corrosion occurs with a molten phase. The mechanism is referred to as molten ash corrosion or liquid ash corrosion. Wastage rates of up to 0.5 mm per year for tubes 10-20 mm thick are not uncommon and can result in rapid reduction of component planned life expectancy. Despite the importance of the corrosion process there has been limited research to date with respect to the relationship between the coal ash properties (coal mineralogy), the ash deposit formed on the fireside

surface and the presence of molten ash corrosive phases. In recent years, however, significant efforts have been placed on the understanding of ash deposition processes. From this research methods to characterize and predict ash behavior on heat transfer surfaces have been developed. In addition to understanding the growth of deposits, itself important to the design and operation of utility boiler systems, these techniques and models have now been applied to understanding the relationships between the deposit and the tube metal surface.

When considering the corrosion process it is important to understand the nature of the tube metal surface. The type of metal used can be a ferritic alloy such as SA213-T22 (iron based alloy with a nominal 2.25 wt% chromium and 1.0 wt.% molybdenum) or an austenitic alloy such as SA213-304 (type 304 stainless steel). In both cases, resistance to high temperature oxidation and corrosion is due to the presence of an intact adherent external protective scale. In the case of the ferritic alloy this scale is predominantly magnetite (Fe_3O_4). For austenitic alloys, the protective scale is chromium oxide. Phases within the deposit which affect the integrity of this scale will result in wastage of the tubing. It is the molten phases formed during the liquid phase corrosion mechanism which are most aggressive towards the protective scale. Under these conditions the high mobility of corrosive ions and the removal of corrosion products including the protective scale results in increased wastage.

Therefore, it is important to understand the phase relationships within deposits and how these phases contribute to the corrosion process. This requires a description of ash deposits and the techniques used to characterize the interactions and reaction with respect to the corrosion interface.

CHARACTERIZATION OF ASH DEPOSITS

Ash deposits are formed from the coal minerals present in the fuel. The common minerals observed in coal are listed in Table 1 along with the nominal chemistry. As the minerals are geological in nature some minerals are poorly defined chemically. The minerals are not distributed uniformly throughout the coal and may be associated with the coal maceral (inherent) or excluded from the coal matrix (extraneous). Furthermore, there is a great variation in size of the mineral grains between different coal sources. The variation of the mineralogy results in a variation in the nature of the ash produced. However, while the ash may be different the bulk chemical composition may show less variation. This difference makes it very difficult to relate the chemical composition of the ash to the behavior of the ash in a combustion system. The mineralogical transformations of the minerals during combustion are complex and do not lend themselves to simplistic correlations. The coal mineralogy is established using a technique called computer controlled scanning electron microscopy (CCSEM). This technique determines the size and chemistry of the various minerals observed in coals. Specifically, CCSEM analysis establishes the size distribution of mineral species in the sample.

Knowing the mineralogy of the coal is the first step in understanding the deposits and their relation to corrosion. It is important to establish the mineralogy of the ash produced in the combustion system. This is performed by again using CCSEM analysis on ash which has passed through the system (fly ash). The comparison of the mineralogy of the coal and the mineralogy of the fly ash allows determination of the complex phase transformations of the minerals. Furthermore, by establishing the mineralogy of the ash it is possible to identify precursors to deposition and potential corrosive molten phase formation within the deposit.

The second stage is to examine and understand the phase relationships within the deposits present on a corroded tube. This analysis is in addition to the forensic analysis of failed or corroded superheater and reheater tubes. Normally, the tube sample is subjected to visual and metallurgical analysis. In cases where fireside corrosion is suspected, the ash deposit is sometimes subjected to x-ray diffraction and chemical analysis. It is from the powder x-ray diffraction analysis of the ash on the tube that the basis of the phase relationship within the deposits and the corrosion was postulated. Table 2 lists some of

the phases associated with high temperature corrosion and the melting point of these phases.

All the phases listed in Table 2 have melting points around the metal skin temperature of the tube. There are a number of issues to discuss with respect to the phases listed. First, the detection of these phases is performed by x-ray diffraction analysis. This analysis only detects crystalline phases and therefore, does not identify "molten" or amorphous phases. The second issue is the application of melting point data for complex salt mixtures. Mixtures of salts such as those found in these deposits will have eutectic and liquidus temperatures below that of the melting point of the pure end members. Therefore some knowledge of the mixture is necessary in order to assess the impact of the phase on melting. This data is obtained by performing an analysis called scanning electron microscopy point count (SEMP) at and around the corrosion interface. SEMPC was developed to determine the phase assemblage of coal ash deposits. The technique involves the analysis of over 200 random points using scanning electron microprobe analysis methodologies. The chemical analysis of each point is then processed through a normative computer program which establishes if the point can be classified as a given phase. For example, a point is classified as quartz when the chemical analysis contains essentially pure silicon and oxygen (oxygen is determined by difference). More complex phases such as mullite ($3\text{Al}_2\text{O}_3 \cdot 2\text{SiO}_2$) are classified based on the presence of essentially silicon, aluminum, and oxygen with the silicon and aluminum at the correct molar ratio (within a reasonable tolerance). The analysis involves the identification of crystalline and amorphous phases. The results are used to determine the type of bonding in an ash deposit and the role of the various phases in deposit growth and development of strength. This involves the application of models of ash transformations and viscosity. Furthermore, the ability to identify and quantify the various amorphous or molten phases allows determination of key characteristics which are related to the chemical composition. These characteristics include the eutectic temperature of a selected region or phase and the potential for reaction with another phase. The eutectic temperature is obtained from phase equilibria.

The potential for reaction is obtained by looking at the base to acid ratio of the individual points classified as amorphous in the SEMPC analysis. Highly basic phases will tend to be more reactive towards acidic phases than other basic phases. Thus it can be seen that SEMPC analysis can have great value in establishing the characteristics of corrosion interfaces. The technique can identify the various phases which are present including the amorphous phases. The eutectic and melting characteristics can be obtained from suitable phase equilibria data and models. Mass transfer of corrosion products and corrodents can be determined using a model of viscosity. Corrosion potential is determined by examining the propensity for interaction between the different amorphous phases (acidic or basic) with the basic or amphoteric oxides of the protective scale. Another advantage of the application of the SEMPC technique to the study of ash corrosion is the ability to determine the relationship between key components within the deposit. For example, while it is difficult to identify the presence of a potassium pyrosulfate phase by x-ray diffraction it is possible to identify phases rich in potassium and sulfur with molar ratios corresponding closely to that of pyrosulfate (i.e. $\text{K/S} = 1.0$ while potassium sulfate has a molar ratio of $\text{K/S} = 2$). Furthermore, the presence of iron with this and similar "corrosive" phases indicates the role of this phase in the corrosion process. Another area where the SEMPC analysis can be used is to establish the change in chemistry and phase within the deposit. As noted above, a phase commonly associated with high temperature corrosion is that of potassium aluminosulfate. This phase is of particular interest as there is no direct precursor to this phase from the coal mineralogy. In most coals all the aluminum is observed with clay species such as kaolinite and illite. Furthermore, the potassium is also mainly associated with the illite clay in coals. A simplistic reaction pathway for this phase would be:



The melt phase would be a mixture of potassium aluminosilicates, the composition of which would be dependent on the original mineral chemistry and the amount of

potassium aluminosulfate formed. Clearly, significant disassociation of the aluminosilicates is necessary to facilitate the reaction of the aluminum and potassium from the reactants. This is not observed in most coal ash deposits where the Si/Al molar ratio (a defining parameter for most clay species) tends to remain constant. The SEMPC technique not only allows one to detect and quantify the amount of potassium aluminosulfate, amongst other phases, but can give valuable insight into the nature of the melt phase. In relation to corrosion the following question is postulated: is the potassium aluminosulfate the corroding phase or is the amorphous phase associated with the potassium aluminosulfate which causes the corrosion.

An example of SEMPC data is given below. The deposit was from a superheater tube where corrosion had been noted based on ultrasonic thickness measurements. The deposit was scraped off and submitted for SEMPC analysis. The phase assemblage is listed in Table 3. The phases include iron oxide, mullite, calcium silicate, calcium sulfate, ferric sulfate, pyrrhotite (FeS), pyrite, aluminosilicate (resembling kaolinite clay) and unclassified phases. The unclassifieds represent the amorphous phases. As part of the SEMPC analysis the points are averaged to obtain a "bulk" chemical composition. This chemical composition corresponds to the average chemistry of the region selected for the analysis and represents the region where the corrosion occurs. The ability to separate the different phases, and thus the corresponding chemistry, allows a determination of the average composition of the amorphous phases. Both these chemical compositions are listed in Table 4. The data shows that the bulk composition of the deposit was enriched in iron oxide, sodium oxide, and sulfur trioxide compared to the original coal ash (12% Fe₂O₃, 1 % Na₂O, 3% SO₃). The amorphous phase was further enriched in SO₃, Na₂O, and K₂O and depleted in CaO and Fe₂O₃. This data shows that the corrosion was due to the presence of a corrosive alkali sulfate phase. However, further analysis can be performed on the SEMPC results. For example, Figure 1 shows a ternary molar plot of Fe, S, and Na for all the points rich in iron, sulfur, and sodium. The graph shows that sulfur is only associated with the points with 5-10 mole % sodium. However, no definitive phase can be ascertained confirming the amorphous nature of the corroding phases. Similar graphs can be produced to establish the relationships between selected components in order to develop a more accurate assessment of the effect of ash chemistry and mineralogy. Furthermore, from this data methods to predict the corrosive potential of a given coal ash with gas and metal temperatures can be developed.

CONCLUSION

The phase relationships in coal ash deposits and their effects on high temperature corrosion have been introduced. The complex nature of deposition and corrosion can be studied by the application of advanced analytical techniques such as computer controlled scanning electron microscopy (CCSEM) and scanning electron microscopy point count (SEMPC). The valuable data from these techniques combined with design and operating conditions can be used to develop methods to control coal ash corrosion.

Table 1
Common Minerals Observed in Coal

| Mineral name | Nominal Chemistry |
|--------------|--|
| Quartz | SiO ₂ |
| Pyrite | FeS ₂ |
| Kaolinite | Al ₂ Si ₂ O ₁₀ (OH) ₂ |
| Illite | K _{1-1.5} Al ₄ Si _{7-8.5} Al _{1-1.5} O ₂₀ (OH) ₄ |
| Calcite | CaCO ₃ |

Table 2
Melting Point of selected phases observed in ash deposits

| Compound | Melting Point/°C |
|---|------------------|
| K ₂ Fe(SO ₄) ₃ | 618 |
| K ₂ Al(SO ₄) ₃ | 654 |
| Na ₂ Fe(SO ₄) ₃ | 624 |
| Na ₂ Al(SO ₄) ₃ | 646 |
| KFe(SO ₄) ₂ | 694 |
| NaFe(SO ₄) ₂ | 690 |

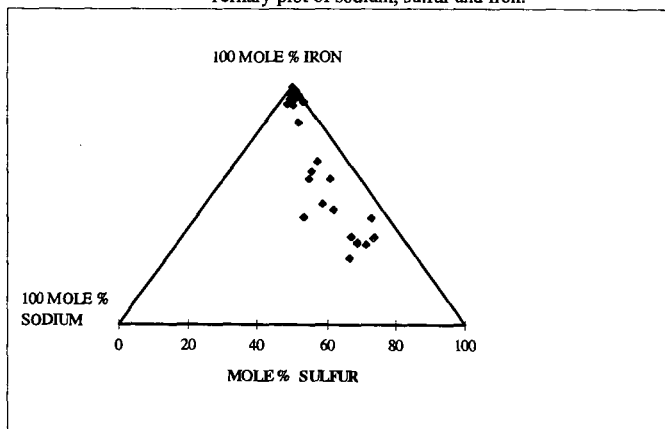
Table 3
Phase Assemblage of Deposit as Determined by SEMPC

| PHASE | VOLUME % |
|--|----------|
| MULLITE ($3\text{Al}_2\text{O}_3 \cdot 2\text{SiO}_2$) | 0.5 |
| CALCIUM SILICATE (CaSiO_3) | 0.5 |
| IRON OXIDE | 18.6 |
| ANHYDRITE (CaSO_4) | 1.0 |
| FERRIC SULFATE ($\text{Fe}_2(\text{SO}_4)_3$) | 4.0 |
| PYRRHOTITE (FeS) | 2.0 |
| PYRITE (FeS_2) | 1.0 |
| ALUMINOSILICATE (KAOLINITE) | 1.0 |
| UNCLASSIFIEDS | 71.4 |

Table 4
Chemical Composition of Ash Deposit

| OXIDE | BULK | AMORPHOUS |
|-----------------------|------|-----------|
| SILICA | 18.1 | 21.5 |
| ALUMINA | 10.3 | 12.0 |
| IRON OXIDE | 36.2 | 24.7 |
| TITANIUM DIOXIDE | 0.5 | 0.5 |
| PHOSPHOROUS PENTOXIDE | 0.3 | 0.4 |
| CALCIUM OXIDE | 1.2 | 0.6 |
| MAGNESIUM OXIDE | 1.0 | 1.1 |
| SODIUM OXIDE | 3.4 | 4.1 |
| POTASSIUM OXIDE | 1.9 | 2.5 |
| SULFUR TRIOXIDE | 26.8 | 32.1 |

Figure 1
Ternary plot of sodium, sulfur and iron.



INFLUENCE OF ASH DEPOSIT CHEMISTRY AND STRUCTURE ON PHYSICAL AND TRANSPORT PROPERTIES

Larry L. Baxter
Combustion Research Facility
Sandia National Laboratories
Livermore, CA 94550

Keywords: Combustion, Ash, Heat Transfer in Porous Media

Abstract

Boiler ash deposits generated during combustion of coal, biomass, black liquor, and energetic materials affect both the net plant efficiency and operating strategy of essentially all boilers. Such deposits decrease convective and radiative heat exchange with boiler heat transfer surfaces. In many cases, even a small amount of ash on a surface decreases local heat transfer rates by factors of three or more. Apart from their impact on heat transfer, ash deposits in boilers represent potential operational problems and boiler maintenance issues, including plugging, tube wastage (erosion and corrosion), and structural damage.

This report relates the chemistry and microstructural properties of ash deposits to their physical and transport properties. Deposit emissivity, thermal conductivity, tenacity, and strength relate quantitatively to deposit microstructure and chemistry. This paper presents data and algorithms illustrating the accuracy and limitations of such relationships.

Introduction

Ash deposit properties in boilers depend on both deposit structure and composition. Thermal conductivity and emissivity, the two properties with the greatest impact on heat transfer, demonstrate strong and complex dependencies on both deposit structure and composition. The effects of deposit structure relate largely to the phases present in the deposit and the extent of sintering or contact between individual particles. This paper focuses on the effects of emissivity and porosity variations on heat transfer through boiler deposits.

Heat and mass transfer through porous media depend on macroscopic and microscopic structural properties of the media. Upper and sometimes lower bounds for transfer coefficients can be established based on easily measured structural properties, but precise expressions for transfer rates depend on a high level of structural detail, commonly beyond what could reasonably be expected to be available in practical applications. Our approach is to identify the limits and increase the level of sophistication of our models up to the point that we make the best use of available information.

Results

A useful idealization for illustrating the major effects of deposit structure on thermal conductivity is a solid of known porosity and thermal conductivity and with no conduction in the gas phase. Quanta of vibrational energy (heat) move randomly through this solid. A temperature gradient in the solid is represented by spatial differences in the population of phonons. We seek an expression relating the efficiency at which phonons can move through the porous material to its physical structure. In this simple model, heat transfer proceeds through the solid phase at its customary rate but stops when it encounters the void phase.

Spatial autocorrelation functions relate the probability of two locations being the same phase (solid or void) as a function of distance between them. Generally, autocorrelation functions are bounded by ± 1 and are identically unity at displacements of 0. Characteristically for real materials, they also decay to a limiting value in a smooth but not necessarily monotonic fashion. For isotropic material, the limiting value is the volume fraction of the phase present at a displacement of 0. If the presence of void vs. solid phase is represented as a random event, there are fairly general conditions under which the autocorrelation becomes an exponential decay, with the spatial constant of the exponent a measure of average grain size.

In addition to the amount of solid vs. void volume in the material, the connectedness of the solid phase plays a large role in determining the heat transfer rate. There are higher order correlation functions and connected correlation functions that statistically give clues to the connectedness of a phase. The concept of tortuosity is the approach we have taken, where the tortuosity is defined as the shortest average path length through the solid phase between two points divided by the straight-line distance between the same points. As the solid phase becomes less connected, the tortuosity increases. Using these three most readily available characteristics of the solid phase, the solid volume fraction, the mean particle size, and the tortuosity, we have developed a model for the dependence of the average thermal conductivity on structural properties. We are currently pursuing means of extending the model to nonisotropic conditions more sophisticated descriptions of deposit structure. In its current state, the heat transfer model depends on material porosity and tortuosity

of both the condensed and gaseous phases, in addition to the thermal conductivity of the two phases.

Aside from the anisotropies of the material, this approach largely ignores the efficiency of the connections between particles. Particles that connect at a single point or over a very small area typically conduct heat far worse than those that are connected over large fractions of their projected areas. In some analyses, the connection points dominate the heat transfer process. This connectedness is captured somewhat, but not entirely, in the concept of the tortuosity. We will examine this aspect of our model in the future. In its current state, it may somewhat over-predict the heat transfer rate in porous media.

The over-prediction is partially compensated by the effect of our initial assumptions. In the original model, the void space was assumed to be non-conducting and radiative heat transfer through the material is ignored. In reality, both intra-media radiative heat transfer and conduction through the gas phase occur. At present, we allow these two simplifications in the model and recognize that they are somewhat balanced by the incomplete descriptions of connectedness of particles in the condensed phase.

In its current state, the heat transfer model reveals some useful insights. These will be illustrated by models of heat transfer through artificially conceived by realistic deposits under boiler-like conditions. The deposits are assumed to exist on cylindrical surfaces and the analysis at this point is limited to one dimension, i.e., the radial dimension.

One dimensional, transient heat transfer through a cylindrical surface is described by

$$\rho \hat{C}_p \frac{\partial T}{\partial t} = k \left[\frac{1}{r} \frac{\partial}{\partial r} \left(r \frac{\partial T}{\partial r} \right) + \frac{1}{r^2} \frac{\partial^2 T}{\partial r^2} \right] \quad (1)$$

Where traditional symbols are used for density, heat capacity, temperature, time, and radial direction and the effective thermal conductivity is represented by k . If the transient term is ignored, the partial differential equation becomes an ordinary, second-order differential equation of the form

$$0 = k \frac{1}{r} \frac{d}{dr} \left(r \frac{dT}{dr} \right) \quad (2)$$

which can be solved directly. Two constants, a and b , are involved in the solution as constants of integration in the first and second steps of the solution as follows

$$a = r \frac{dT}{dr} \quad (3)$$

and

$$T = a \ln(r) + b \quad (4)$$

By equating the surface heat flux at the fireside of the deposit with the heat flux conducted through that deposit at that location,

$$-k \frac{dT}{dr} \Big|_{r=r_d} = q \quad (5)$$

the first constant can be evaluated as

$$a = \frac{-qr_d}{k} \quad (6)$$

The second constant is evaluated by equating the temperature at the inner surface of the deposit to the boiler tube surface temperature

$$T(r_i) = T_i = \frac{-qr_i}{k} \ln(r_i) + b \quad (7)$$

which yields

$$b = T_i + \frac{qr_i}{k} \ln(r_i) \quad (8)$$

rendering a final solution of the form

$$T(r) = T_i - \frac{qr_i}{k} \ln\left(\frac{r}{r_i}\right) \quad (9)$$

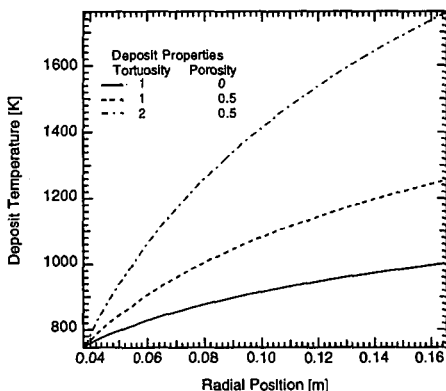


Figure 1 Parametric variation of deposit temperature as a function of position for various values of the solid volume fraction and tortuosity. See text for details of incident heat flux, etc.

This form reduces to a linear dependence of deposit temperature on distance in the limit of small deposit thickness relative to the radius of curvature. An example temperature profile is illustrated in Fig. 1 for the case of a five-inch deposit resting on a three-inch, outside-diameter steam tube with a 750 K surface temperature exposed to a heat flux of 10 kW/m² and with a thermal conductivity of 2.22 W/(m K). Both the porosity and tortuosity are considered to be unity in the base case, with both parameters being varied by a factor of two to illustrate the effects of deposit properties on the temperature profile. The temperature range depends linearly on the tortuosity and inversely on the porosity such that a change in either quantity changes the difference between deposit surface temperature and tube surface temperature by the same factor. The extent of curvature in the prediction is determined by ge-

ometry, not deposit physical properties. Deposits with solid volume fractions lower than (more porous than) 0.5 and tortuosities higher than 2 are common in many systems.

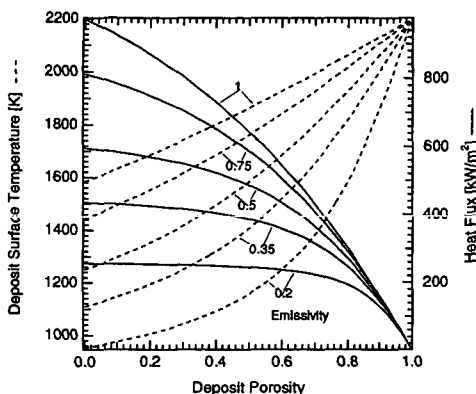


Figure 2 Deposit surface temperature and heat flux as a function of porosity and emissivity assuming no intra-deposit radiative heat transfer and a non-conducting gas phase. Tortuosity is assumed to be unity.

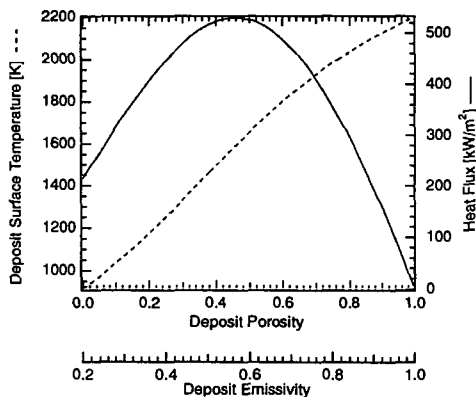


Figure 3 Deposit surface temperature and heat flux under the same assumptions as in Figure 2 but assuming a linear relationship between emissivity and porosity.

The previous predictions assumed that the incident heat flux, whether from radiation or convection, does not change as deposit surface temperature changes. In practice, incident heat flux is strongly coupled to deposit surface temperature. As an illustration, the heat transfer model predictions for the furnace section of a typical boiler are illustrated below. Only radiative heat transfer is considered, with an assumed black body radiative temperature of 2200 K, deposit thickness of 2 mm, deposit solid phase thermal conductivity of 2.22 W/(m K), and a waterwall composed of 750 K walls made of four inch OD tubes. Predictions of deposit surface temperature and heat flux are illustrated for a range of porosity and deposit emissivity values. Intra-deposit radiative heat transfer and intra-deposit conductive heat transfer through the gas phase are neglected and deposit tortuosity is assumed to be unity. None of these assumptions is generally accurate. They are made here to allow illustration of the impact of porosity and emissivity on heat transfer.

The parametric graph indicated in Fig. 2 belies the potential complexity of the relationships between deposit physical properties and heat transfer rates. While the trends in Fig. 2 indicate relatively smoothly varying and monotonic relationships between emissivity or porosity and heat flux, in practice the relationship may not be monotonic. In many cases of practical interest porosity and emissivity are correlated. Heat fluxes under such conditions may not vary monotonically with physical properties. Figure 3 illustrates the trends with an assumed linear relationship between porosity and emissivity, as read by the dual abscissae. As the relationships become more complex, and as factors such as intra-deposit radiative heat transfer and tortuosity are included, the relationships can become increasingly complex.

Structural properties of ash vary temporally, effecting changes in both porosity and tortuosity. A common example is sintering or melting of deposits, accompanied by increases in particle-to-particle contacting area and decreases in tortuosity and porosity. A simple example is illustrated in Fig. 4. In an idealized case of uniform spheres, a change in linear dimension of less than 15 % is accompanied by a change in contacting efficiency of theoretically zero in the initial case to 50 % in the slightly sintered case. This gives rise to proportional changes in tortuosity and the porosity changes from 0.48 to 0.17. Such changes lend themselves to mathematical treatments in predicting heat transfer through ash deposits. Similar treatments describe the effect of condensation or sulfation on deposit microstructure. These have been used in the past to explain the development of deposit properties ranging from tenacity to strength.

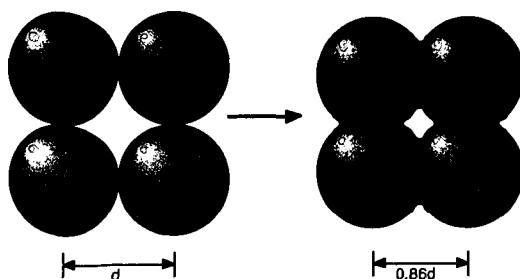


Figure 4 Conceptual illustration of the changes in contacting efficiency and tortuosity with sintering/melting.

As a practical example, Figure 5 is a scanning electron micrograph of a deposit produced during combustion of rice straw in Sandia's Multifuel Combustor. The deposit was generated on the wall of the MFC combustor and accumulated over a 3 hour test period. The wall temperature was 900 °C, the gas temperature was 1000 °C, and the gas composition is estimated to contain 6 % oxygen. Most of the deposit has a glassy appearance, with occasional nodules under the otherwise smooth surface.

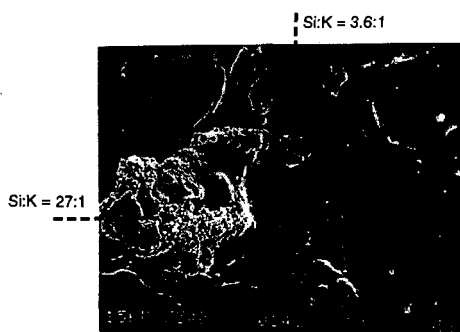


Figure 5 Scanning electron micrograph of a portion of a rice straw deposit collected from a ceramic surface in the MFC. The porous, silica based material was exposed by fracturing the deposit through one of the nodules evident in many locations on the smooth, glassy surface.

The deposit composition is determined as a function of location on the surface using electron dispersive spectroscopy in a scanning electron microscope. Both phases are composed principally of silicon. By comparison with the nodules, the glassy phase contains more nonsiliceous material. More than half of the nonsiliceous fraction is potassium.

For example, the melting point of silica decreases from about 1700 °C to less than 750 °C as potassium is introduced to form potassium silicates. Incorporation of additional materials, in particular other alkalis and alkaline earth materials, usually lowers the melting point further still. The silicon to potassium ratio observed in the glassy portions of the deposit illustrated in Figure 5 is about 3.4 on a mass basis, or about 81 % SiO_2 to 19 % K_2O . An equilibrium mixture of such material becomes completely molten at approximately 1300 °C. This is slightly above the temperature of deposit, but the addition of calcium and other heteroatoms to this mixture reduces the melting point significantly. The nodular material, on the other hand, has a much higher melting point. These changes in phase have obvious effects on the microstructure of the deposit and hence on its physical and transport properties.

Conclusions

Ash deposit microstructure influences the mechanical and transport properties by impacting the degree of connectedness between particles and the tortuosity of heat transport through the deposit. Mathematical models are used to predict the impact of microstructural features on bulk deposit properties and on resulting boiler performance. Deposit surface temperatures can change many hundreds of degrees, depending on deposit thermal and structural properties. Heat fluxes are also dominantly influenced by similar structural properties. Two properties that encapsulate much of the deposit microstructure effect are the porosity and tortuosity. Rational models of the dependence of thermal conductivity on these parameters are presented with predicted results. Experimental examples of how tortuosity and porosity develop in deposits, depending on deposit phase, are also presented.

ALGEBRAIC INTERPRETATION OF COMPOSITION PHASE CLASSIFICATION CRITERIA FOR CCSEM.

Peter N. Slater, M. Bret Abbott, and John N. Harb
Department of Chemical Engineering and Advanced Combustion Engineering Research Center
Brigham Young University
Provo, UT 84602

Keywords: CCSEM, Fly Ash, Classification

INTRODUCTION

Data from computer controlled scanning electron microscopy (CCSEM) are typically interpreted by grouping particles into bins based on their elemental compositions. Some of the bins correspond to well-defined mineralogical species or phases with known properties. Other bins are defined for convenience so that similar particles can be grouped together. Experience has shown that it is difficult to predict *a priori* what phases will be determined in an analysis; this is particularly true in the case of fly ash samples which are largely amorphous at combustion temperatures. Often a large number fraction of the analyzed particles do not fit any of the predefined phases and are classified as unknown. In such cases, it is difficult to interpret the analysis results since nothing is known about a large fraction of the sample. It is desirable then to have a means of extracting some sort of composition information from the unclassifiable particles. This paper addresses the problem of defining new bins to describe particles which do not fit into the predefined classifications using an algebraic formulation of the criteria.

METHOD

CCSEM reports particle compositions as n-dimensional vectors, where n is the number of elements analyzed. Typically, n is equal to twelve and the elements are Na, Mg, Al, Si, P, S, Cl, K, Ca, Ti, Fe, and Ba. To determine whether or not a given composition belongs to a phase, numerical tests or criteria are applied. These tests are linear inequalities, e.g., $Si + Al \leq 80$, or ratios, e.g., $Si/Al \leq 2$, which can be expressed as linear inequalities. Therefore, the test for membership in a phase can be written as a system of linear inequalities. Using matrix notation, the test can be written $Ax \leq b$, where the rows in the matrix A and the vector b correspond with the individual criteria.

Consider for example, a simple system with two elements, X and Y, and two phases, A and B with constraints as follows:

| Phase A | Phase B |
|-------------|------------------|
| $x \leq 40$ | $x \geq 80$ |
| $y \leq 40$ | $y \leq 40$ |
| | $x + y \leq 100$ |

It is implicitly assumed that compositions are limited by zero below and by one hundred percent above. The algebraic forms for these two phases would be:

| Phase A | Phase B |
|---|---|
| $\begin{bmatrix} 1 & 0 \\ 0 & 1 \end{bmatrix} \begin{bmatrix} x \\ y \end{bmatrix} \leq \begin{bmatrix} 40 \\ 40 \end{bmatrix}$ | $\begin{bmatrix} -1 & 0 \\ 0 & 1 \\ 1 & 1 \end{bmatrix} \begin{bmatrix} x \\ y \end{bmatrix} \leq \begin{bmatrix} -80 \\ 20 \\ 100 \end{bmatrix}$ |

Note that the sign of the first constraint for phase B has been changed so that it could be written in the less than or equal to form. The phases can also be represented as regions in the x-y plane, as illustrated in Figure 1. Any composition (x,y) falling within the square region at the lower left would be classified as phase A. Likewise, phase B would comprise any composition falling within the triangular region at upper right. Any other composition, such as the points indicated in the figure, would be unclassified.

The unclassifiable points in Fig. 1 appear in two distinct clusters. One is nearer to phase A and the other is nearer to phase B. The observation that unknown particles tend to appear in clusters when plotted in this fashion and that a cluster would of necessity lie closest to one phase is the basis for the algebraic classification scheme: find the distance to each of the defined phases and then group the composition with the phase having the shortest distance.

Finding the distance from a point to a given phase is an optimization problem called a quadratic program. The quadratic objective function is the square of the Euclidean distance from the composition to a composition that meets the phase's criteria. By minimizing this objective function subject to the criteria, the composition within the phase closest to the given composition is determined. Examination of the resulting groupings of unknown compositions from a complete CCSEM analysis reveals trends and clusters of points which can be used to define new phases. This classification scheme is shown in Fig. 2.

The algorithm has been implemented using a sparse matrix data structure to minimize the memory and computational requirements. Several thousand known compositions can be classified

in minutes on a 75MHz Pentium computer. Using a numerical Sequential Quadratic Programming (SQP) algorithm to solve the quadratic programs on an HP 9000/755 workstation, several thousand unknown compositions can be classified in about an hour. The number of optimizations required is $m \cdot p$, where m is the number of unknown particles and p is the number of known phases. Given this dependence, it has proven wise to start with a relatively small number of particles, several hundred rather than several thousand, and define new phases based on the initial results before proceeding to the complete data set. This dramatically reduces the number of optimizations.

RESULTS AND DISCUSSION

The method has been applied to the analysis of ash derived from Pittsburgh #8, an eastern subbituminous coal, and ash from Black Thunder, a western subbituminous coal from the Anderson seam of the Powder River Basin. ASTM ash analyses of the elemental oxides from both coals are presented in Table 1. Note the low-rank Black Thunder contains a great deal of organically bound calcium and relatively few discrete mineral grains. Its ash, therefore, is expected to be significantly influenced by the organically bound constituents. The inorganic content of Pittsburgh #8, however, is primarily discrete minerals. The major mineral species found in the Pittsburgh coal are pyrite, quartz, aluminosilicates, potassium aluminosilicates, pyrite, and calcite [1]. The ash of Pittsburgh #8 is controlled by the transformations (coalescence and fragmentation) of the discrete minerals during combustion.

Ash data from both coals were classified using a typical set of phases. This set consisted of 47 well-defined phases [3] and several more loosely-defined aluminosilicate phases. The results of the classification are presented in Table 2. The heavy line separates the loose phases from the phases that were more well-defined. Minor phases have been omitted from the table for brevity. The phase set used is clearly inadequate for characterizing these ashes; 58% of the Black Thunder and 24% of the Pittsburgh #8 particles were unclassifiable. In fact, only 14% of the Black Thunder and 7.54% of the Pittsburgh #8 was classified with the well-characterized bins, and the majority of that was quartz.

In the Pittsburgh #8 ash, 39% of the particles contained five mole percent or more iron. Of these, 19% or nearly half of the iron-bearing particles were unclassifiable. Given the importance of iron in ash deposition behavior, it is essential to know more about its occurrence in the ash than is provided by the this typical phase set.

The algebraic classification scheme was applied to the Black Thunder ash using the 47 well-defined phases. Results are tabulated in Table 3. The quantities are reported in percentage of original particles (classifiable plus unclassifiable). Minor phases (less than 1% of total) have been omitted. Only values for Mg, Al, Si, Fe, and Ca are reported since these five elements were found to be sufficient to characterize the bins. Of course, other elements do play a role in the properties of individual particles and the category as a whole. Their omission in the table does not imply that they should be ignored when the CCSEM analysis is interpreted. The table includes the mean value and standard deviation for each of the elements included.

Using the 47 phases, 85% of the Black Thunder ash particles were unclassifiable. The algebraic classification scheme was able to classify 82% of the particles into eight major phases. The contents of the various bins are distinct from one another, as evidenced by the differences in the means of the major elements which characterize each bin. The "near quartz" category has the highest mean silicon content, 76%. Several bins share the same major elements, but in clearly distinguishable compositions. It is sometimes desirable to further subclassify these bins; preliminary work has shown that classifications based on the ranking of the four most abundant elements in a particle is a good basis for distinguishing composition within a nearest-phase category.

To focus on the distribution of iron in the 24% of the particles that were found unclassifiable, the algorithm was applied to the Pittsburgh #8 ash using the phase set which included the loosely-defined bins. The results for the major iron-containing bins are presented in Table 4. Bins were chosen for inclusion based on the fraction of the total iron-bearing particles they contained; bins with less than one percent have been omitted. It is clear that most of the unclassifiable particles contain iron and that they can be grouped into nine major categories. The means in these categories are distinct, indicating that the algorithm has indeed differentiated the particles.

In most cases, particles did not fit into their nearest phases because they contained too much of a minor constituent. Cutoffs are typically five mole percent. In the "near Fe-Al-Silicate" phase, 44% of the particles contained too much calcium, 32% contained too much potassium, and 18% contained too much sodium. Many particles violated more than one constraint; i.e. they contained too much of two or more elements. Examination of the reasons why particles do not fit the known phases yields insight into both the ash composition and the mechanisms by which it formed.

CONCLUSIONS

Particle composition classification schemes must be designed to provide meaningful information about specific ash samples due to the variability in the parent fuels and combustion conditions. Using a generic set of phases, large fractions of the particles are often unclassifiable.

The algebraic interpretation of the phase criteria provides a straightforward means of classifying these particles with no assumptions about the dominant elements or the form that the new classifications should take. The classifications thus made provide a number of distinct categories that can be used to characterize the ash.

ACKNOWLEDGMENTS

The authors wish to thank David P. Kalmanovitch for his invaluable assistance in formulating the criteria used to identify crystalline phases. Rachel Newsom and Eyas Hmouz undertook the tedious work of translating the phase criteria for use with the algebraic classification program. This work was funded by the U.S. Department of Energy under the University Coal Research Program, Grant No. DE-FG22-93PC93226. Additional funding was provided by the Advanced Combustion Engineering Research Center (ACERC) at Brigham Young University. Funds for ACERC are received from the National Science Foundation, the State of Utah, 42 industrial participants, and the U.S. Department of Energy.

REFERENCES

1. Harb, J.N. (1994) Investigation of Mineral Transformations and Ash Deposition During Staged Combustion, Quarterly Progress Report #3, U.S. Department of Energy Contract DE-FG22-93PC93226.
2. Richards, G. H. (1994) Investigation of Mechanisms for the Formation of Fly Ash and Ash Deposits for Two Powder River Basin Coals, Ph.D. Dissertation, Brigham Young University, Provo, UT, 84602.
3. Kalmanovitch, D.P. (1991) Personal Communication

Table 1. Ash Oxide Analyses (SO_3 -free) of Black Thunder and Pittsburgh #8 Coals

| Weight % of Ash | Black Thunder [2] | Pittsburgh #8 [1] |
|-------------------------|----------------------|----------------------|
| SiO_2 | 36.7 | 47.86 |
| Al_2O_3 | 19.7 | 21.79 |
| Fe_2O_3 | 6.1 | 18.01 |
| TiO_2 | 1.5 | 1.06 |
| CaO | 25.5 | 6.69 |
| MgO | 5.7 | 1.16 |
| Na_2O | 1.7 | 0.75 |
| K_2O | 0.4 | 1.73 |
| P_2O_5 | 1.1 | 0.37 |

Table 2. Phase Distribution of Ash Particles

| Phase | Black Thunder (% of particles) | Pittsburgh #8 (% of particles) |
|----------------------|-----------------------------------|-----------------------------------|
| Quartz | 12.38 | 5.31 |
| Iron Oxide/Carbonate | 0.0 | 2.23 |
| Plagioclase Solution | 1.76 | 0.0 |
| Kaolinite | 12.54 | 35.77 |
| Ca-Al-Silicate | 6.2 | 3.61 |
| Na-Al-Silicate | 5.35 | 1.8 |
| K-Al-Silicate | 1.44 | 8.67 |
| Fe-Al-Silicate | 0.21 | 14.55 |
| Fe-Silicate | 0.37 | 2.37 |
| Unclassified | 57.57 | 24.53 |

Table 3. Nearest Phase Classifications of Black Thunder Ash

| Phase | Nearest Phase | % | | Mg | Al | Si | Ca | Fe |
|-------|------------------------|------|-----|------|------|------|------|-----|
| 1 | Quartz | 3.4 | ave | 2.0 | 8.2 | 76.1 | 5.6 | 1.6 |
| | | | std | 7.5 | 4.3 | 19.2 | 7.8 | 2.8 |
| 2 | Ca-Aluminate | 3.6 | ave | 11.7 | 29.8 | 4.6 | 45.1 | 6.5 |
| | | | std | 4.2 | 2.8 | 2.9 | 2.8 | 2.5 |
| 3 | Tri Ca-Aluminate | 35.4 | ave | 14.1 | 21.5 | 4.7 | 48.8 | 7.7 |
| | | | std | 5.5 | 7.8 | 3.4 | 6.8 | 3.9 |
| 4 | Gehlenite | 4.3 | ave | 8.9 | 26.5 | 12.4 | 38.4 | 8.7 |
| | | | std | 4.2 | 7.6 | 5.5 | 5.9 | 7.5 |
| 5 | Gehlenite-Na melilite | 2.7 | ave | 5.9 | 28.2 | 25.4 | 28.9 | 5.4 |
| | | | std | 3.0 | 4.9 | 7.8 | 6.4 | 5.7 |
| 6 | Akermanite-Na melilite | 5.8 | ave | 10.7 | 14.3 | 30.7 | 33.7 | 5.9 |
| | | | std | 7.2 | 6.9 | 15.5 | 7.9 | 5.8 |
| 7 | Anorthite | 1.3 | ave | 3.6 | 37.2 | 32.1 | 18.4 | 3.6 |
| | | | std | 2.4 | 4.4 | 5.5 | 3.9 | 3.2 |
| 8 | Plagioclase Solution | 25.2 | ave | 0.6 | 38.2 | 50.3 | 3.3 | 1.4 |
| | | | std | 1.4 | 9.7 | 8.5 | 4.5 | 3.4 |

Table 4. Nearest Phase Classification of Iron Particles in Pittsburgh #8 Ash

| Phase | Nearest Phase | % | | Na | Mg | Al | Si | S | K | Ca | Fe |
|-------|------------------------|------|-----|-----|-----|------|------|-----|-----|------|------|
| 1 | Gehlenite-Na melilite | 0.65 | ave | 0.8 | 1.8 | 23.9 | 27.4 | 4.0 | 0.4 | 24.8 | 13.4 |
| | | | std | 1.4 | 2.1 | 4.0 | 7.8 | 6.8 | 1.2 | 6.1 | 6.6 |
| 2 | Akermanite-Na melilite | 1.35 | ave | 1.5 | 5.4 | 15.0 | 26.4 | 3.3 | 0.1 | 25.3 | 17.8 |
| | | | std | 2.0 | 5.6 | 4.7 | 10.2 | 5.1 | 0.5 | 6.6 | 10.4 |
| 3 | Anorthite | 0.58 | ave | 0.5 | 2.1 | 32.5 | 34.7 | 1.8 | 0.7 | 15.0 | 10.3 |
| | | | std | 0.8 | 2.2 | 2.6 | 2.9 | 3.1 | 0.9 | 2.6 | 3.5 |
| 4 | Plagioclase | 1.2 | ave | 3.4 | 2.4 | 29.0 | 36.9 | 4.1 | 2.1 | 8.9 | 10.6 |
| | | | std | 2.7 | 2.3 | 4.8 | 5.5 | 6.3 | 1.7 | 3.5 | 4.5 |
| 5 | Kaolinite | 2.71 | ave | 0.7 | 0.9 | 21.3 | 68.1 | 3.0 | 1.6 | 1.2 | 2.1 |
| | | | std | 1.2 | 1.7 | 15.3 | 18.1 | 2.9 | 1.5 | 1.9 | 1.8 |
| 6 | Ca-Al-Silicate | 3.66 | ave | 1.2 | 4.3 | 28.4 | 35.0 | 1.8 | 1.1 | 19.0 | 5.8 |
| | | | std | 1.5 | 7.6 | 9.0 | 11.2 | 2.8 | 1.4 | 12.9 | 2.7 |
| 7 | K-Al-Silicate | 2.01 | ave | 3.9 | 1.4 | 31.1 | 39.8 | 3.4 | 7.7 | 1.3 | 4.4 |
| | | | std | 4.6 | 2.4 | 12.4 | 14.9 | 4.7 | 9.7 | 2.1 | 2.9 |
| 8 | Fe-Al-Silicate | 8.99 | ave | 2.7 | 2.9 | 30.0 | 37.4 | 1.4 | 3.2 | 4.2 | 15.5 |
| | | | std | 2.1 | 4.4 | 7.1 | 9.0 | 2.8 | 2.1 | 3.4 | 11.7 |
| 9 | Iron Silicate | 1.76 | ave | 1.9 | 1.7 | 10.9 | 23.5 | 4.9 | 0.6 | 5.0 | 49.6 |
| | | | std | 4.5 | 4.2 | 7.0 | 22.6 | 8.5 | 1.1 | 7.9 | 20.3 |

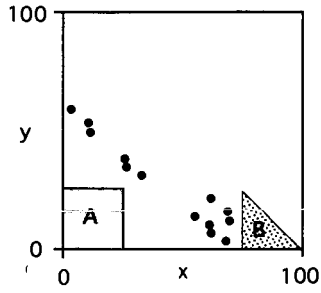


Figure 1. Phases A and B

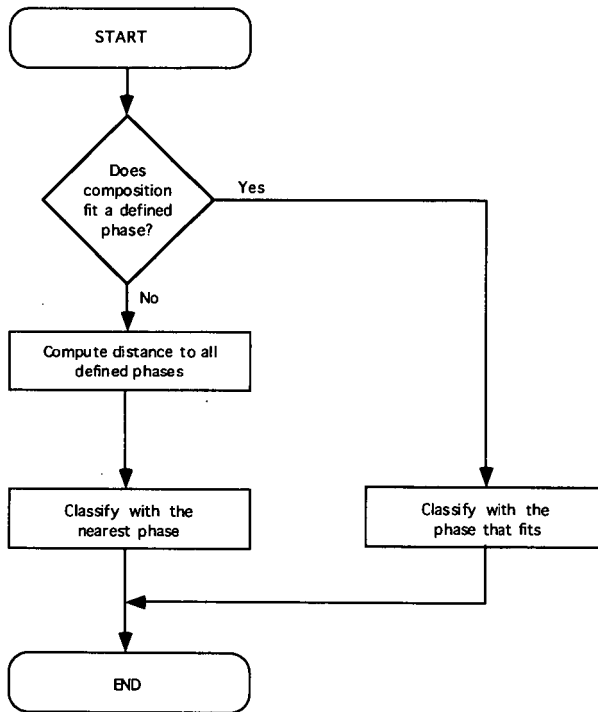


Figure 2. The Algebraic Classification Algorithm

SLAGGING BEHAVIOUR OF PEAT ASH

Heikkinen, R., Laitinen, R. S., Patrikainen, T., Tiainen, M., Virtanen, M.
Department of Chemistry, University of Oulu, Linnanmaa,
SF-90570 Oulu, Finland

Keywords: peat ash, slagging, SEM

INTRODUCTION

The use of peat for energy production in Finland dates back to early 1970's. For the present, the peat combustion is responsible for over 5 % of the energy production in Finland. Many of the major Finnish power plants still use pulverised fuel, but the utilisation of fluidised bed boilers is rapidly increasing. Boilers of this type are best suited for fuel with a low energy value because the increased efficiency is beneficial for the community heat distribution.

The Toppila power plant of Oulu Energy Company in the city of Oulu, Finland has two units. The older one, Toppila I, is a 250 MW boiler using pulverised peat as fuel. The new Toppila II boiler is a 310 MW circulating fluidised bed boiler. The power plant uses 15 000 m³ of peat per day with full load.

The slagging behaviour of peat ash varies depending on the bog peat is originating. The plant shutdown because of extensive slagging may cause significant economical losses in the entire chain of energy production. Therefore the slagging behaviour of peat ash needs to be predicted already from peat prior to its combustion.

In coal ash chemistry the slag formation is connected to the presence of iron, sulphur, alkaline and earth alkaline metals in ash. These metals act as fluxing agents in aluminium silicate systems.¹⁻³ Several predictive indices have been developed for coal in order to estimate the slagging tendency of coal ash.⁴ These indices are based on the bulk analysis carried out in laboratory conditions using standard ashing methods.⁵ These indices have been criticized, because the ash is not formed in the actual turbulent conditions with fast heating rate and real gas phase composition.⁶ New methods have been developed to understand the sintering and slagging events. These methods use coal analyses, power plant parameters, ash analyses together with CCSEM, analyses from probe samples, fly ash samples, bottom ash samples, aerosols etc.^{4,7-10}

RESULTS AND DISCUSSION

In this study we report the slagging behaviour of five peat samples (A-E) of different origin. With the exception of B the samples were collected from Toppila I and originate from Northern Finland. Samples of standard ash were analysed by using ICP- and DCP-AES, X-ray diffraction (XRD), and scanning electron microscopy with energy dispersive X-ray microanalysis (SEM-EDS). Table 1 presents the both the CHNS-analysis of the original peat sample and the elemental bulk compositions of standard ash from each sample.

The ash of peat A that is known to have a strong tendency to slag contains remarkable quantities of iron and relatively small amounts of aluminium and silicon oxides. The content of alkaline metals is quite low. The ash of peat B also known to be problematic contains a remarkably high amount of calcium. The sulphur content is also higher than in the harmless peat types C, D, and E.

X-ray diffraction powder diagrams were recorded with a Siemens D5000 diffractometer. Ash samples were carefully ground and mixed with ethyl alcohol to make a slurry which was spread on a glass plate for the diffraction experiment. Quartz, albite and anorthite are the most common minerals in peat ash. The tendency of peat ash to slag seems to correlate with high amounts of haematite and maghemite (peat A) or anhydrite (peat B).

Scanning electron microscopy (Jeol JSM-6400 and Link eXL system with the image analysis software) provides simultaneous information on the chemical composition and mineral content of fuel ash particles.

The mineral content of original peat is very low and the particles seem to be scattered throughout the organic material. Therefore we could not observe any minerals in peat. It was only after standard ashing⁵ that inorganic material was visible in the SEM image.

The SEM images were produced by applying constant accelerating voltage of 15 kV and the current of 1.70·10⁻⁶A. The magnification was 430X. When possible, the minimum of one thousand particles were analysed.

The composition of peat ash based on CCSEM can be visualized by using appropriate distribution diagrams (see Figure 1). The classification yields useful information when the corners in these "ternary" diagrams are defined in terms of the total content of selected oxides. The composition at each corner is chosen in order to gain information about the potential glass formation in the slag particles. It can easily be seen from the diagrams in Figure 1 that the phase distribution in the ash particles of the harmless peat E is different from that in the severely slagging peat A. It is obvious that the content of iron-rich particles is greatly enhanced in the problematic peat ash. While the bulk analyses shown in Figure 2 do not provide information about the composition of discrete particles, they do reflect the differences in the particle distribution between the slagging and harmless fuel in a qualitative fashion (c.f. Figure 1).

The slagging indices were calculated from the bulk analysis of peat ash. As these indices have been developed for coal and depend on the sulfur content found in coal,⁴ they are not suitable for the prediction of slagging behaviour of peat ash due to the very low sulphur content in each peat sample. This is exemplified in Figure 3 that shows the slagging index, R_s , of the standard ash for each peat sample A-E. In each case the slagging index implies relatively unproblematic behaviour upon combustion. It is known, however, that the peat A and B show a severe tendency to slag, whereas the peat C, D, and E are known to be relatively harmless. As seen from Figure 3, the slagging index does not carry information even on the relative slagging tendency. This is due not only to the low sulphur content but also due to the differences in the contents of silicon, phosphorous, sodium, potassium, calcium, and iron.

Two extensive tests in an actual power plant boiler have also been carried out. Samples were collected from the fireside by use of the slagging probes. Analyses were made from samples taken from fuel, slagging probes, and fly ash. The evaluation of the results is currently in progress, but it already seems apparent that the standard ash does not behave similarly to the actual boiler ash in all respects.

CONCLUSIONS

It is one of the corner stones in coal and glass chemistry^{1,11} that alkaline metals, alkaline earth metals, iron, sulphur and phosphorous are able to lower the melting point and increase the viscosities of fuel ash particles. This phenomenon may lead to a severe slagging problem in the boiler superheater and wall area. It is important to design predictive tools for the ash slagging in order to prevent the major economical losses caused by a possible plant shutdown.

The mineral material in peat differs to a certain extent from that in coal. For example, both coal and peat contain iron in significant amounts. Coal, however, contains sulfur in larger amounts than peat, because iron is found as pyrite in coal, whereas in peat it occurs as siderite or as haematite. Therefore, we are currently developing a new classification technique to establish the mineral distribution of peat and peat ash particles. The method is based on CCSEM. The conventional classification utilizing CCSEM is based on the identification of mineral phases from the elemental composition of the particles. This approach might not be useful in the case of ash particles, since extensive glass formation takes place upon combustion. Therefore, the particle distribution is best judged on the basis of oxide distribution as illustrated in Figure 1. The choice of suitable corned compositions enables meaningful deductions to be made about the actual phases in the ash particles. The mineral composition of bulk ash can be studied with XRD powder diffraction. The tendency of ash vitrification, however, can also be observed from the shape of the diffraction diagrams.

REFERENCES

- (1) Raask, E., *Mineral Impurities in Coal Combustion*, Hemisphere, New York, 1985, 485 pp.
- (2) Boni, A. A.; Helble, J. J.; Srinivasachar, S., EPRI, Effects of Coal Quality on Power Plants-Second International Conference, Saint Louis, Missouri, Sep 19-21, 1990, p. 1.15-1.38.
- (3) Huffman, G. P.; Huggins, F. E.; Shah, N.; Shah, A., *Progr. Energy Comb. Science* **1990**, *16*, 243-251.
- (4) Winegardner, E. C., *Coal Fouling and Slagging Parameters*, ASME Publ., 1974.
- (5) *Annual Book of ASTM Standards, Vol. 05.05 Gaseous Fuels; Coal and Coke*, American Society for Testing and Materials, 1989, D 3174-89, p. 302.
- (6) Skorupska, N. M.; Couch, G., Engineering Foundation Conference, June 20-25, 1993, Solihull, England, p. 137-150.
- (7) Skrifvars, B.-J., *Report, 1989, 89-13*, Åbo Akademi.
- (8) Beér, J. M.; Sarofim, A. F.; Barta, L. E., Engineering Foundation Conference, March 10-15, 1991, Palm Coast, Florida, p. 71-94.
- (9) Hutchings, I. S.; West, S. S.; Williamson, J., Engineering Foundation Conference, July 16-22, 1995, Waterville Valley, New Hampshire, Session V.
- (10) Lind, T.-L.; Kauppinen, E. I.; Valmari, T.; Klippel, N.; Mauritzson, C., Engineering Foundation Conference, July 16-22, 1995, Waterville Valley, New Hampshire, Session VII.
- (11) Rawson, H. *Inorganic Glass-Forming Systems*, Academic Press, London, 1967, pp. 317.

Table 1. Ultimate and ash analyses of peat (A,C-E peat from domestic sources; B peat from abroad). A and B exhibit severe slagging. C-E are harmless.

| Ultimate analysis | A % | B % | C % | D % | E % |
|----------------------------------|-------|-------|-------|-------|-------|
| C | 49,1 | 50,3 | 52,9 | 51,0 | 52,0 |
| H | 6,08 | 5,84 | 6,34 | 6,66 | 6,39 |
| N | 2,77 | 1,44 | 2,50 | 2,79 | 1,27 |
| S | 0,22 | 0,31 | 0,27 | 0,21 | 0,13 |
| O | 32,9 | 35,6 | 33,8 | 33,5 | 36,6 |
| ash | 8,96 | 6,51 | 4,18 | 5,81 | 3,58 |
| Standard ash composition of peat | | | | | |
| Na | 0,02 | 1,10 | 0,43 | 0,43 | 1,48 |
| Mg | 0,78 | 2,92 | 2,32 | 1,15 | 1,68 |
| Al | 3,20 | 4,64 | 4,41 | 4,23 | 6,79 |
| Si | 6,17 | 17,31 | 8,87 | 17,40 | 19,64 |
| P | 4,62 | 1,34 | 2,28 | 2,35 | 1,97 |
| K | 0,06 | 0,96 | 0,83 | 2,47 | 2,75 |
| Ca | 7,99 | 21,53 | 17,14 | 8,00 | 9,17 |
| Ti | 0,06 | 0,31 | 0,15 | 0,14 | 0,50 |
| Fe | 61,37 | 7,68 | 38,97 | 27,79 | 18,56 |
| B | 0,19 | 0,04 | 0,23 | 0,15 | 0,21 |

* calculated value

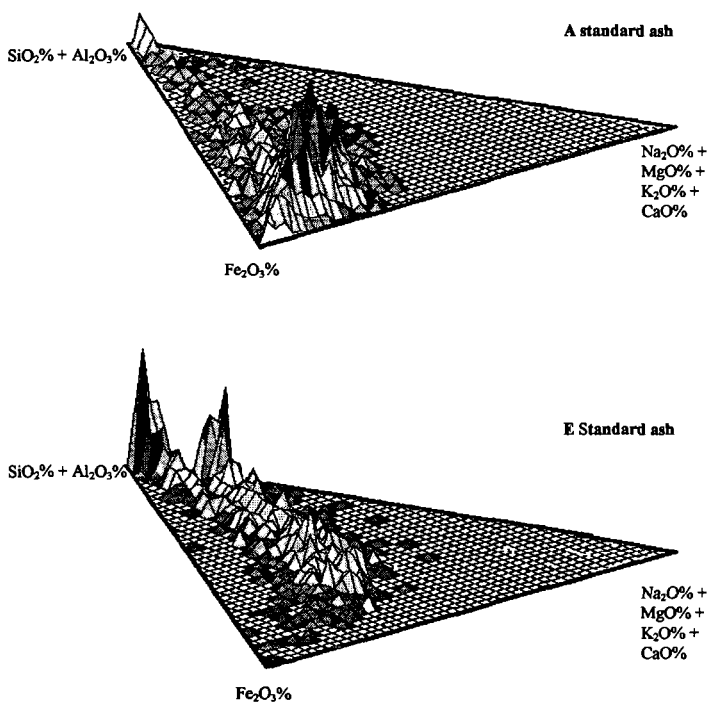


Figure 1. The compositional distribution of ash particles in slagging (A) and harmless (E) peat. The height of the column relates to the fraction of particles with the indicated composition. The ash particles of peat A are concentrated in the iron-rich region in the diagram implying the presence of low melting iron-silicates.

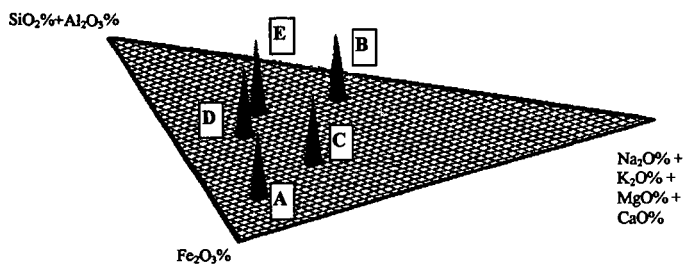


Figure 2. The bulk composition of standard ash from peat A-E.

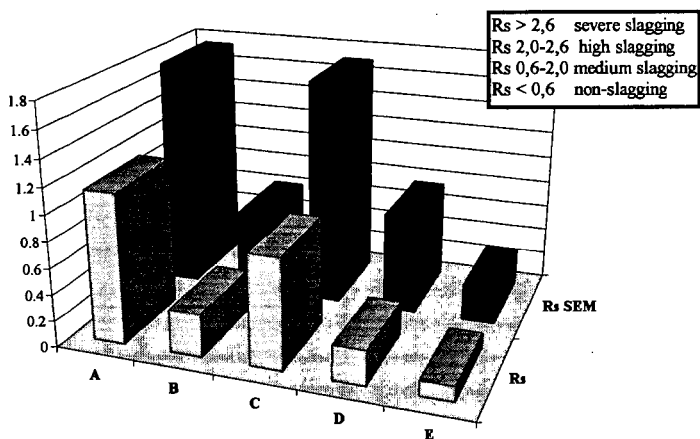


Figure 3. The slagging index ⁴ was calculated both from the bulk ash composition (R_s) and from the particle compositions as determined with SEM-EDS (R_s SEM). Both indices show the same trends. As indicated in the figure, these values are typical for non-slagging or medium slagging ash. However, due to the very low sulfur content in peat, R_s index is not directly applicable to peat. In fact A and B have turned out to exhibit severe slagging behaviour.

IMPACT OF CHAR AND ASH FINES ON POROUS CERAMIC FILTER LIFE

M. A. Alvin
Westinghouse Electric Corporation
Science & Technology Center
Pittsburgh, PA 15235

Keywords: Char, ash, filtration.

ABSTRACT

Although frequently inert, char and ash fines can potentially have a deleterious impact on the life of porous ceramic filters that are currently being utilized in advanced coal-fired applications. This paper reviews several of the char and ash related issues that have been encountered in various Westinghouse Advanced Particulate Filtration systems which limited filter life.

INTRODUCTION

During the past 10-15 years, Westinghouse has been involved in the development of Advanced Particulate Filtration (APF) systems for removal of char and ash fines that are released during coal and biomass gasification or combustion. Initially individual porous ceramic filter elements were installed in slipstreams at the Kellogg Rust-Westinghouse (KRW) fluid-bed gasification test facility in Madison, Pennsylvania, and at the New York University combustion test facility in Westbury, New York. Recently these efforts have been expanded to the use of multiple cluster arrays containing 384 or 748 filter elements within a common pressure vessel at the American Electric Power (AEP) pressurized fluidized-bed combustion (PFBC) demonstration plant in Brilliant, Ohio, and at the Sierra Pacific integrated gasification and combined cycle (IGCC) test facility in Reno, Nevada.

Numerous phase changes and generally a loss of material strength were encountered during use of the monolithic first generation filters under PFBC conditions at AEP, as well as during operation in Ahlstrom/Foster Wheeler's pressurized circulating fluidized-bed combustion (PCFBC) test facility in Karhula, Finland.^(1,2) When catastrophic failure of the first generation monolithic filter elements occurred, it generally resulted from thermal fatigue or shock of the oxide-based alumina/mullite matrices, or from creep crack growth of the nonoxide-based clay bonded silicon carbide filter materials. Advanced second generation, fracture toughened, fiber reinforced filter elements are currently being developed and installed in W-APF systems in an attempt to mitigate catastrophic failure of the porous ceramic matrix during process operation. The stability and/or changes within the second generation filters materials are being evaluated in on-going test programs at the Westinghouse Science and Technology Center in Pittsburgh, Pennsylvania.⁽³⁾

Although the composition and morphology of the first and second generation filter materials change during exposure to advanced coal-fired and biomass process environments, the porous ceramic filter elements generally remain intact, surviving exposure to the process temperature and gas chemistry. Unfortunately failure and performance limitations (i.e., reduced gas flow permeability; decreased particle removal efficiency; etc.) have been encountered due to ash related issues as (1) bridging; (2) filter bowing; (3) inner wall blinding; (4) inner bore plugging; (5) wedging of fines between the ceramic filter flange and metal holder mount; (6) auto-ignition; and (7) membrane debonding in alkali-laden systems. The following section provides an overview of Westinghouse's field experience where filter life and performance have been limited by the deposition and adherence of char and ash fines.

FIELD EXPERIENCE

American Electric Power — Pressurized Fluidized-Bed Combustion

During the early test campaigns at AEP, the Westinghouse APF system was challenged with inlet dust loadings of 600 ppmw, consisting primarily of fine ash particles with a mass mean particle size of 1-3 μm . As a result of the small particle size and the tendency for the particles to sinter, dust built-up between filter elements, and along the dust sheds and plenum support pipes, forming compact bridges. Ash bridging lead to bowing and distortion of the clay bonded silicon carbide candles at process operating temperatures of 620-790°C, as well as random catastrophic failure of filters during plant startup and shutdown. Post-test inspection of the filter arrays indicated the close proximity and/or contact of the bottom closed end caps of adjacent bowed candles, and the fresh fractured surfaces at the base of the filter flanges.

When failure occurred during the early test campaigns at AEP, fines were released into the clean gas plenum and exhaust gases. During pulse cleaning, fines were reentrained and back pulsed into the inner wall of the remaining intact filter elements. Due to the relatively extensive open porosity of the 15 mm clay bonded silicon carbide filter support wall, fines filled the porous wall to depths of ~1-3 mm from the inner surface, reducing gas flow permeability through the elements.

Alternately during the later test campaigns at AEP, when the primary cyclone was inactivated, the filter array was challenged with dust loadings of 18,000 ppmw, consisting primarily of ash particles with a mass mean size of 27 μm . Ash bridging was not encountered after 1110 hours of operation at temperatures of 760-845°C. A tenaciously bonded ash cake formation, however, resulted along the metal filter holder mounts along the top arrays. Enhanced sulfur sorption occurred along the fines that encapsulated the top filter holder mounts, leading to the formation of magnesium sulfate hydrate ($\text{MgSO}_4 \cdot 6\text{H}_2\text{O}$) and anhydrite (CaSO_4).⁽⁴⁾ The high thermal expansion of the ash fines which wedged in between the filters and metal holder mounts potentially caused failure of several of the low load bearing elements to occur during multiple plant startup and shutdown cycles.

Once random failure of the filters was encountered, ash was released into the effluent stream, which was then back pulsed into the inner bore of the remaining intact filter elements. Due to the high particulate loading during conduct of the final test campaign at AEP, compact plugs of ash accumulated within the inner bore of select filter elements. Again due to the high thermal expansion of the ash in comparison to the ceramic filter matrices, crack formations resulted generally near the end caps of the clay bonded silicon carbide, alumina/mullite, and fiber reinforced chemically vapor infiltrated (CVI) silicon carbide candles after numerous plant startup and shutdown cycles. Although failure of these elements did not occur during process operation, removal and elimination of the elements from continued testing was warranted.

Comment

Irrespective of the high load bearing capabilities of the first generation monolithic filters, or the low load bearing capabilities of the advanced second generation filament wound or fiber reinforced filter matrices, successful extended operating life and performance of porous ceramic filters in high temperature coal-fired process applications will require mitigation of ash bridging events. Process control will also require that sorption of gas phase sulfur species be accompanied by subsequent removal of the fines without deposition and retention of tenaciously bonded dust cake layers along metal support structures. The tenaciously bonded sulfur-enriched ash conceivably limited the life of the low load bearing advanced filter elements, and lead to a labor intensive effort for removal of the remaining intact monolithic alumina/mullite and clay bonded silicon carbide candles, and second generation CVI-SiC composite filter elements.

Ash filling, blinding of the inner wall, or plugging of the inner bore leads to reduced gas flow permeability through the porous ceramic filter matrices and possibly decreases the dust cake removal capabilities during pulse cleaning. In addition, development of crack formations and a substantially increased weight of the elements results, and the capability to regenerate or clean the filter elements off-line becomes virtually limited. Obviously successful extended operating life and performance of the hot gas filtration system will require that ash bridging and wedging along the exterior of the filter elements, and ash filling, blinding, and/or plugging along the inner wall and bore of the filter elements be eliminated.

Ahlstrom — Pressurized Circulating Fluidized-Bed Combustion

During operation of the W-APF at the Ahlstrom PCFBC test facility in Karhula, Finland, 128 alumina/mullite candle filters were initially installed and operated at temperatures of ~900°C.⁽²⁾ Failure of several of the elements was considered to have occurred during the first test campaign as a result of ignition of carbon monoxide-rich process gas in the presence of oxygen when the main air compressor malfunctioned. Generally the ~900°C PCFBC operating temperatures were considered to lower the thermal fatigue characteristics of the alumina/mullite matrix, through the formation of microcracks along the inner bore of the candle, which ultimately reduced the strength of the conditioned filter elements.

After removal of the alumina/mullite candles and installation of the clay bonded silicon carbide filters testing continued at temperatures of ~830°C. Creep crack growth of the clay bonded silicon carbide filters resulted, ultimately leading to elongation of the filter body and random

catastrophic failure. As a result, efforts fostered the development of advanced high temperature, creep resistance binder-containing, clay bonded silicon carbide candle filters.

Foster Wheeler — Carbonizer and Combustor Test Facilities

In 1992, Westinghouse installed and operated an APF system at the Foster Wheeler carbonizer test facility in Livingston, New Jersey. Twenty-two alumina/mullite candles formed the filter array. Initially one element failed, and char fines were back pulsed into the inner bore of the remaining filter elements. During startup in an oxidizing environment, combustion of the fines resulted, and catastrophic failure of several of the alumina/mullite filter elements occurred. Although alternate first or second generation filter elements had not been subjected to similar operating conditions, limited survival of these materials to withstand auto-ignition is expected.

In 1993 an alternate array of candles was installed in the W-APF system and operated under second generation PFBC conditions at the Foster Wheeler. During a ~210 hour test segment, the cyclone plugged and the filter vessel was filled with ash fines, causing failure of several of the filter elements. Post-test inspection of the array indicated that a tenaciously bonded sodium-potassium sulfate eutectic melt formed along the outer surface of the filter elements, which then served as the collection site for the adherence of CaSO_4 , CaO and CaCO_3 fines.⁽⁵⁾ The formation of the eutectic melt readily caused debonding of the membrane along the outer surface of the clay bonded silicon carbide filters. The alumina/mullite candles were virtually unaffected. Additional reactions of the binder phase in the clay bonded silicon carbide filter elements with gas phase alkali released in the Foster Wheeler second generation PFBC effluent stream were also observed.

The deleterious impact of auto-ignition of char fines, as well as the formation of the mixed alkali eutectic phase and bed carry-over require more stringent process control in order to achieve successful long-term operation of the ceramic filter elements in the advanced particulate removal systems.

Texaco — Entrained-Bed Gasification

Westinghouse utilized cross flow filters during the early test campaigns at the Texaco entrained-bed gasification test facility in Montebello, California. Failure was encountered when the stacked plate alumina/mullite cross flow filters delaminated, and when char fines became wedged between the cross flow flange and metal filter holder mounts. Wedging and failure along the flange had also been observed during long-term durability testing of the cross flow filters under simulated high temperature, high pressure, PFBC conditions at the Westinghouse test facility in Pittsburgh, Pennsylvania.

During the later test campaigns, clay bonded silicon carbide and alumina/mullite candle filters were retrofitted into the Westinghouse filter vessel at Texaco. After ~400 hours of operation, the candles were removed, and were observed to be coated with a tenaciously bonded dust cake layer. Removal of the $\text{FeO}(\text{OH})$, FeAl_2O_4 -enriched cake from the outer surface of the filter elements was extremely difficult, which ultimately lead to the removal of the membrane of the clay bonded silicon carbide candle filters.⁽⁵⁾

Biomass Gasification

In 1994 and 1995 Westinghouse operated a twelve filter element array at the IGT biomass fluidized-bed gasification test facility in Chicago, Illinois. Post-test inspection of the clay bonded silicon carbide filter elements after ~21 and ~30 hours indicated that either an ~5.3 mm brown or ~1.2 mm black dust cake layer remained along the outer surface of the filter elements. The Fe_3O_4 , Fe_2O_3 , C, K, and SiO_2 -enriched dust cake layer which was easily removed from the filters generally retained the contour of the candle body.⁽⁴⁾ Debonding and/or removal of the outer membrane of the clay bonded silicon carbide candles was not observed after short-term operation in the 675-916°C biomass gasification environment.

FILTER ELEMENT LIFE AND REGENERABILITY

Porous ceramic filter elements can be utilized for extended service operation as demonstrated by Westinghouse during conduct of the five test campaigns at AEP where several surveillance clay bonded silicon carbide candles successfully survived 5855 hours of operation. At AEP Westinghouse also demonstrated the regenerability of the clay bonded silicon carbide candles by initially brushing the ash cake layer from the outer surface of the filter elements, followed by water washing and drying. Nearly complete gas flow permeability was recovered for the filter

elements in this manner. If ash blinding occurred along the inner wall or fines formed a compact inner bore plug, complete regenerability of the elements was not possible.

FILTER ELEMENT CONSTRUCTION

During field operation, the texture or roughness of the outer surface, as well as changes in the wall thickness of the filter elements dramatically impact the adherence and/or removal of the dust cake layer. As the texture or roughness of the surface increases, residual ash cake thickness tends to increase, leading to a reduced gas permeability through the filter wall. An optimal construction of the filter element is a uniform wall thickness along the length of the body and closed end cap areas. In this manner uniform removal of the dust cake layer can be accomplished during pulse cleaning.

FUTURE EFFORTS

Westinghouse will continue to explore the impact of char and ash fines on the stability of the porous ceramic filters during future testing at the Sierra Pacific Pinon Pine gasification test facility in Reno, Nevada, and at the Southern Company Services integrated gasification and combined cycle (IGCC) test facility in Wilsonville, Alabama, and at the Pacific International Center for High Temperature Research (PICHTR) biomass gasification demonstration plant in Hawaii. Testing is currently on-going at the Foster Wheeler/Ahlstrom test facility in Karhula, Finland, where advanced first and second generation monolithic and fiber reinforced filter elements are being subjected to 900°C PCFBC test conditions. As a result of these efforts, the ultimate viability, performance and robustness of the first and second generation porous ceramic filter elements will be challenged under a relatively wide gamut of process operating conditions — all of which are required to define successful long-term operation of the advanced high temperature particulate filtration systems.

REFERENCES

1. M. A. Alvin, "Advanced Ceramic Materials for Use in High Temperature Particulate Removal Systems," 1995 AIChE Annual Meeting, Miami, FL, November 17, 1995.
2. M. A. Alvin, R. E. Tressler, T. E. Lippert, E. S. Diaz, and E. E. Smeltzer, "Durability of Ceramic Filters," Coal-Fired Power Systems 94 — Advances in IGCC and PFBC Review Meeting, Morgantown, WV, June 21-23, 1994.
3. M. A. Alvin, T. E. Lippert, E. S. Diaz, and E. E. Smeltzer, "Filter Component Assessment," Advanced Coal-Fired Power Systems '95 Review Meeting, Morgantown, WV, June 27-29, 1995.
4. M. A. Alvin, "Advanced Coal-Fired and Biomass Ash and Char Formations," 12th International Pittsburgh Coal Conference, Pittsburgh, PA, September 11-15, 1995.
5. M. A. Alvin, "Characterization of Ash and Char Formations in Advanced High Temperature Particulate Filtration Systems," Fuel Processing Technology, Vol. 44, Nos. 1-3, September 1995, pp. 237-283.

THE ROLE OF PHYSICAL FACTORS IN MASS TRANSPORT AND PHASE TRANSFORMATION IN INTERGRANULAR MELTS DURING COAL ASH SINTERING AND DEPOSIT DEFORMATION

Jan W. Nowok, John P. Hurley, and Steven A. Benson
Energy & Environmental Research Center
University of North Dakota
PO Box 9018
Grand Forks, ND 58202-9018

Keywords: Coal ash deposits, ductile properties, mass transport phenomena

ABSTRACT

The role of physical properties of melts such as viscosity, diffusion, and surface-interfacial tensions in sintering and deformation mechanisms of ash deposits above the glass transformation temperature is discussed. The differential thermal analysis (DTA) technique was applied to measure glass transformation and crystallization temperatures. Sintering of selected coal ashes was performed as a function of temperature in air. The mechanical properties of sintered ashes were measured below and above T_g . It was found that a correlation exists between sintering propensities of amorphous ashes and plastic deformation of deposits above T_g , which both depend on the mass transport phenomena in the intergranular liquid phase.

INTRODUCTION

In combustion and gasification technologies a great need exists to define the lowest temperature at which the fouling propensity of fly ash on heat-exchange surfaces is maximally reduced. Numerous experimental studies have been reported in the literature that emphasize the role of interparticle melts in the sintering behavior of fly ashes. Using a quasichemical approximation, researchers were able at first to give a qualitative description of the liquid-phase composition that causes rapid deposit growth. Specific interactions between ash particles with dissimilar chemical compositions usually cause the formation of an interparticle silicate melt with a nonuniform structural composition, the unstable physical properties of which affect intergranular mass transport. The structural heterogeneity of silicate melts depends on two major contributions to the free energy of mixing: configurational entropy of mixing, which favors mutual miscibility, and dispersion forces, which energetically favor phase separation. A formulation of the chemical composition and structural homogeneity of melts to account for intergranular transport in the liquid phase is applied here. The preparation procedure for homogeneous aluminosilicates derived from coal ashes was described in an earlier article.¹ Mass transport through an intergranular liquid phase near and above the temperature of glass transformation, T_g , in sintering and superplasticlike deformation of ash deposits is described here.

HYSTERESIS IN MELT-CRYSTAL TRANSFORMATION AND GLASS TRANSFORMATION TEMPERATURE

Figure 1 illustrates the variation of Beulah slag viscosity with temperature, on cooling. The rapid increase of viscosity below the temperature of critical viscosity (T_c) is caused by slag crystallization.² Figure 2 shows the differential thermal analysis (DTA) results for Beulah glass and two more selected glasses derived from coal ashes on heating. The exotherms are caused by the formation of crystalline phases. Generally, hysteresis in the slag-crystal transformation manifests itself as a difference in crystallization temperatures on cooling of a melt and on heating of a glass. This effect does not suggest that melt transformation occurs at two different free energies. On cooling, the free energy of a supercooled melt is similar to that of nucleation and crystalline-phase growth on the liquidus. On heating, however, the additional energy for nucleation and further crystal growth of the same crystalline phase(s) comes from strain energy created during fast cooling and interfacial energy in the case of polycrystalline amorphous material. The strain energy results from the formation of an unrelaxed matrix during structural relaxation of the melt. The formation of a crystalline phase 1) in the bulk of the slag will increase its viscosity and simultaneously change its flow characteristics and 2) in an intergranular melt will increase deposit strength.¹

The temperatures of glass transformation, T_g , on heating, are indicated in Figure 2. The ideal T_g corresponds to structural relaxation, at which the melt remains in equilibrium, and crystallization does not occur. This takes place only when the quench rate is high enough.³ It has been demonstrated empirically that shear viscosity is of the order of 10^{13} poise at T_g , and various thermodynamic quantities such as compressibility, specific heat, and thermal expansion are discontinuous.⁴ In this context, the glass transition is simply a reflection of the appearance of the elastic component. A remarkable aspect of glass transition is that it suggests changes in deposit behavior from brittle below T_g to ductile above T_g . This means that a glassy slag and/or intergranular amorphous phase will start to flow.

Figure 3 illustrates the variation in the crystallization temperature and temperature of glass transition with the base:acid ratio. Generally, both temperatures, T_c and T_g , increase with lowering base:acid ratio.

The T_g can be evaluated using an empirical equation [1] if the liquidus temperature of an aluminosilicate system is known:³

$$T_g/T_c = 2/3 \quad [1]$$

Calculated temperatures of glass transformation for amorphous ash slags, included in Figure 3, correspond to those determined by DTA.

DENSIFICATION AND SUPERPLASTICLIKE DEFORMATION

Figure 4 illustrates changes in the apparent density of sintered amorphous coal ashes with temperature. The minimum on the curves corresponds to the maximum volume of deposits resulting from the volume of material and closed pores.⁶ Usually, the densification process is defined as a pore filling by a liquid-phase flow and pore shrinkage, depending on the physical properties of the melt. The sintering process in Beulah and Montana ashes begins at about 700° and 750°C and occurs at temperatures lower than the glass transition temperatures, $T_g \approx 800^\circ$ and $\approx 830^\circ\text{C}$, respectively. This process seems to be caused by strain and interfacial energies stored in surface layers of unrelaxed ash particles, which enhance the diffusion coefficient of ions. Stress has long been known to affect the diffusion process in glass components. A quenched glass usually has a higher ionic transport rate than its crystalline form.

Figure 5 shows the compressive stress-strain relationship in sintered Illinois ash slag determined below and above the temperature of glass transformation, $T_g \approx 940^\circ\text{C}$. Interestingly, the ash deposit is brittle below T_g and exhibits ductile properties above 900°C as a consequence of the disappearance of the elastic property of the intergranular amorphous phase. It is apparent that mean compressive stress decreases as the ash base:acid ratio increases (Figure 6). This suggests that the yield strength of the deposit depends on the thickness of the intergranular liquid phase and decreases with the increases in the base:acid ratio. Generally, the uniform yield (flow) stress as recorded on Figures 5 and 6 is attributable to superplasticlike deformation of materials, which is observed during stretching of a body as a large elongation without cracking. In glass ceramics, superplasticlike behavior may arise either by the viscous flow mechanism of intergranular layers or diffusion, which may be similar either to viscous⁷ or to diffusional⁸ creeps. Most silicate glasses containing modifying oxides are close to ideal elastic solids below the glass transition temperature.⁹ There is, however, a small delay of elastic effect, likely resulting from the motion of alkali ions.

DISCUSSION

Intergranular mass transport in coal ashes sintered above the temperature of glass transformation (T_g) can be compared to that in capillarylike media that is based on viscous-diffusional mass transport.¹⁰ In this model of liquid-phase sintering, the motion of the melt is caused by activated motion of the meniscus, which may occur either by viscous flow or by volume diffusion. The movement of the meniscus originates from the interface of atomic/ionic motion, creating a dynamic surface tension in the liquid phase. Intergranular mass transport through the liquid phase requires a sufficient quantity of melt, above some critical thickness, which may be provided by the dissolution of silicate from ash particles into the melt. In heterogeneous systems, this can create gradients of chemical potential, possibly introducing nonequilibrium conditions.

Superplasticlike deformation in ash deposits may occur above the temperature of glass transformation (T_g). Two major independent factors allow superplasticlike deformation in a polycrystalline material with a liquid phase to occur. The first factor is a repetitive cycle of plasticity and dissolution of particle-to-particle connections; the second is compressive stress, which will segregate a small fraction of liquid to triple junctions.¹¹ Thus, the model of superplasticlike deformation of ash deposits above T_g seems to be similar to that of the transport of matter through the liquid phase in the liquid-phase sintering mechanism. The migration of intergranular melt is a response to the imposed gradients of hydrostatic pressure across the specimen caused either by surface tension, in the case of sintering, or by compressive stress, in case of superplastic deformation.

LITERATURE CITED

1. Nowok, J.W.; Benson, S.A.; Steadman E.N.; Brekke, D.W. *Fuel* **1993**, 72, 1055.
2. Nowok, J.W. *Energy & Fuels* **1994**, 8, 1324.
3. Leutheusser, E. *Phys. Rev.* **1984**, 29A, 2765.
4. Fumiko Yonezawa. *Solid State Physics* **1991**, 45, 179.
5. Baret, G.; Madar, R.; Bernard, C. *J. Electrochem. Soc.* **1991**, 138, 2836.
6. Nowok, J.W.; Benson, S.A.; Jones, M.L.; Kalmanovitch, D.P. *Fuel* **1990**, 69, 1020.
7. Dryden, J.R.; Kucerosvsky, D.S.; Wilkinson, D.S.; Watt, D.F. *Acta Metall.* **1989**, 37, 2007.
8. Chen I-W.; Liand, An Xue. *J. Am. Ceram. Soc.* **1990**, 73, 2585.
9. Bansal, N.P.; Doremus, R.H. *Handbook of Glass Properties*; Academic Press: Orlando, 1986; p 306.
10. Nowok, J.W. *J. Mater. Res.* **1995**, 10, 401.
11. Maehara, Y.; Langdon. T.G. *J. Mater. Sci.* **1990**, 25, 2275.

TABLE 1. Composition of Coal Ashes (weight percent expressed as equivalent oxide)

| ID | Description | B:A | SiO ₂ | Al ₂ O ₃ | Fe ₂ O ₃ | TiO ₂ | CaO | MgO | Na ₂ O | K ₂ O | P ₂ O ₅ |
|----|-----------------------|------|------------------|--------------------------------|--------------------------------|------------------|------|-----|-------------------|------------------|-------------------------------|
| A | Beulah | 0.64 | 27.5 | 15.0 | 16.3 | 1.6 | 24.8 | 5.9 | 8.1 | 0.1 | 0.6 |
| B | NIPSCO | 0.64 | 31.1 | 15.1 | 13.0 | 1.3 | 29.4 | 6.9 | 1.2 | 2.1 | 0.3 |
| C | SUFCo | 0.37 | 51.3 | 11.0 | 9.6 | 0.4 | 22.1 | 2.0 | 2.7 | 0.0 | 0.8 |
| D | Montana Subbituminous | 0.28 | 47.2 | 24.0 | 5.4 | 1.1 | 15.5 | 4.7 | 0.7 | 0.7 | 0.7 |
| E | Pittsburgh 1 | 0.17 | 47.8 | 18.1 | 18.0 | 0.8 | 9.4 | 3.0 | 1.5 | 1.1 | 0.1 |
| F | Pittsburgh 2 | 0.15 | 48.7 | 18.7 | 18.7 | 0.9 | 8.3 | 1.6 | 1.1 | 1.8 | 0.2 |
| G | Illinois | 0.12 | 48.6 | 23.1 | 14.3 | 1.2 | 5.6 | 1.6 | 0.5 | 3.1 | 0.3 |
| H | Gascoyne | 0.73 | 35.2 | 11.5 | 8.8 | 1.5 | 27.6 | 7.5 | 6.7 | 0.1 | 1.0 |

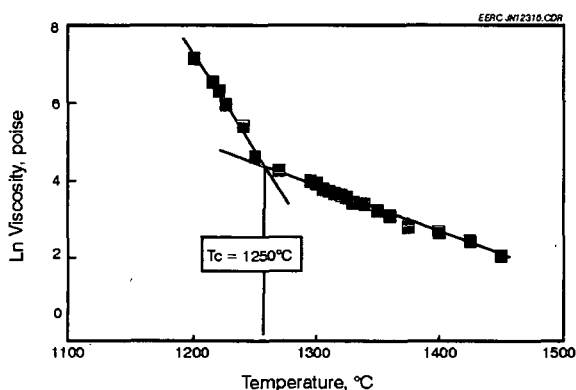


Figure 1. Logarithm viscosity-temperature relationship for Beulah ash slag, as determined on cooling.

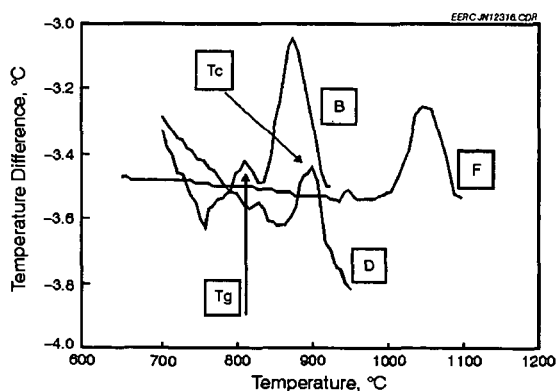


Figure 2. DTA curve of NIPSCO (B), Montana subbituminous (D) and Pittsburgh 2 (F) ash glasses, as determined on heating. DTA measurements were performed using a DuPont 2100 instrument in air at a heating rate of 8°C/min.

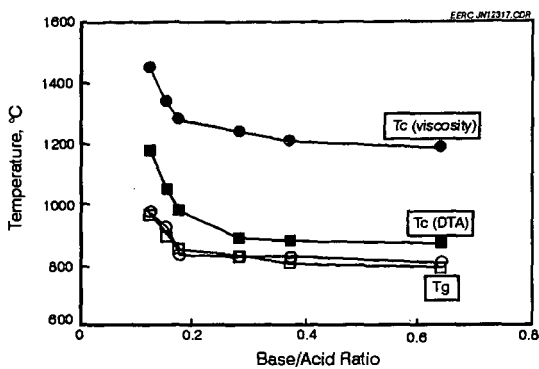


Figure 3. The relationship between the temperature of glass crystallization, glass transformation, and base:acid ratio in ash slags. The calculated values of T_g are represented by \square . The chemical compositions of the coal ashes are listed in Table 1.

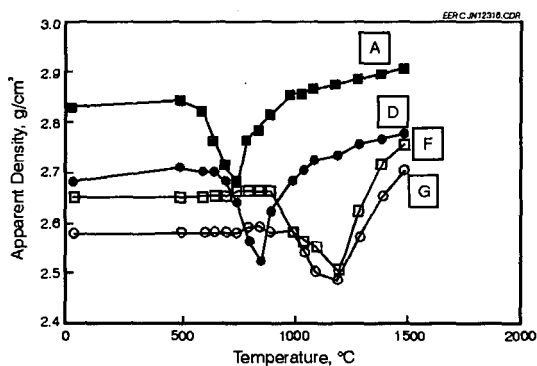


Figure 4. Dependence of apparent density upon sintering temperature for selected ash slags. The chemical compositions of the coal ashes are listed in Table 1.

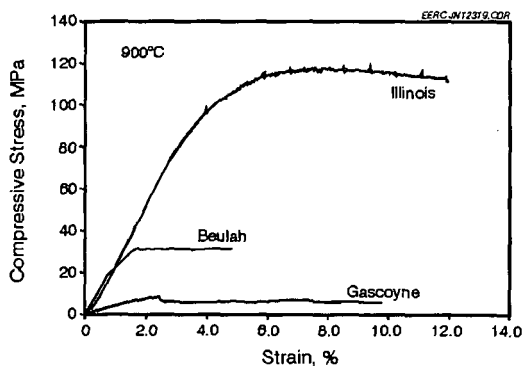


Figure 5. Compressive stress vs. strain in Illinois coal sintered at 1100°C for 20 hr in air. The deformation rate was $2 \cdot 10^{-5} \text{ m} \cdot \text{min}^{-1}$.

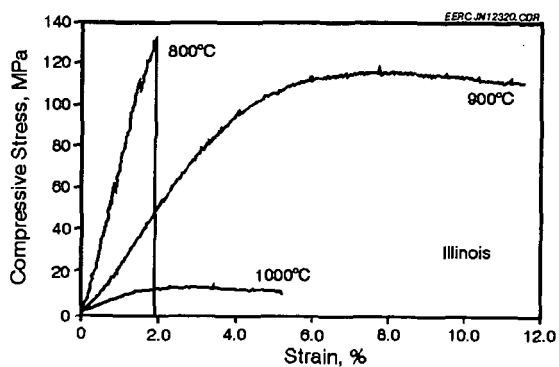


Figure 6. Compressive stress vs. strain in Illinois, Beulah, and Gascoyne ashes sintered at 1100°C for 20 hr in air. The deformation rate was $2 \cdot 10^{-3} \text{ m} \cdot \text{min}^{-1}$.

GASIFICATION SLAG RHEOLOGY IN TITANIUM-RICH, IRON AND CALCIUM-ALUMINOSILICATE GLASSES

D. D. Brooker, M. S. Oh*, J. C. Groen.

Texaco, Inc., P.O. Box 509, Beacon, NY 12508,

*Hongik University, Dept. of Chemical Engineering, Seoul, Korea

Keywords: gasification, slag viscosity, titanium-rich aluminosilicate glass

INTRODUCTION

The Texaco Gasification Process (TGP) employs a high temperature, high pressure slagging gasifier to produce synthesis gas for power, hydrogen, and chemicals. During gasification most of the ash collects on the refractory wall to form a molten glass or slag. The viscosity of the slag plays a key role in determining operating conditions. Insufficient operating temperatures can cause erratic slag flow from the unit, while excessive operating temperatures can result in rapid refractory wear.

Waste streams that are high in titanium (e.g. plastics and tires where TiO_2 is used as a pigment) are being tested for gasification by Texaco. Texaco has developed a process to liquify both used plastics and tires with heated oil to produce a pumpable feed referred to as plastic-oil or tire-oil. Other major elements found with the titanium in these feeds include calcium, aluminum, iron, silicon, and zinc. The zinc sublimes during gasification, leaving behind a titanium-rich calcium-aluminosilicate glass with various amounts of iron.

The rheology of iron and calcium-aluminosilicate glasses within a gasifier has been studied through experimentation under reducing conditions, and by comparing this data to empirical models. Our initial study¹ indicated that: i) most calcium-rich gasification slags should exhibit the classical behavior of a newtonian glass (a continuous slow increase in viscosity as the temperature decreases), and ii) iron-rich slags can exhibit either newtonian or non-newtonian behavior (very low viscosity at high temperatures with a rapid increase in viscosity at some critical temperature (T_c)). At temperatures below T_c , the slag is thought to change from a homogeneous fluid to a mixture of a fluid and rapidly crystallizing phase(s). Slag rheology under oxidizing conditions has been modeled rather successfully with empirical models based on slag composition. These models include Watt-Fereday,² Urbain³, Si Ratio⁴, or modifications of those models⁵. However, these models are limited to 0-5% TiO_2 , and do not predict T_c .

A study by Monteiro, et al⁶, using titanium-rich, calcium-aluminosilicate glass was conducted in which up to 15% TiO_2 was used as a nucleation catalyst. The end result was a reduction in the melting point of the glass by the titanium dioxide. To extend the data base to higher titanium levels, in both calcium and iron-rich, aluminosilicate slags under reducing conditions, viscosity testing was conducted using 0-30% TiO_2 added to both synthetic glasses and gasification slags obtained from commercial units. The experimental viscosity curves were then compared to the empirical curves to determine how well the empirical curves could predict high titanium slag rheology under reducing conditions.

EXPERIMENTAL

Set Up: A Haake Rotovisco RV-100 system with a coaxial cylinder sensor system was employed for viscosity measurements. The sensor system, stationary crucible, and rotating bob with tapered bottom, all composed of high density alumina, are placed in a high temperature furnace. The heating elements (Kanthal Super ST) of the furnace are completely isolated from the viscometer assembly by a mullite tube which runs from the top to the bottom of the furnace. This protects the brittle heating elements from breaking during loading and unloading of the sensor system. The furnace temperature control and the data acquisition of shear rate vs. shear stress were obtained through PARAGON software on an IBM PC. To simulate a reducing condition, a 60/40 mix of CO/CO_2 was passed over the sample at a flow rate of 300 cc/min. The gas mixture entered from the bottom of the furnace and exited through the top. The viscometer was calibrated with a National Bureau of Standard (NBS) borosilicate glass (Standard Reference Material 717).

Procedures: A cylindrical crucible is placed in the furnace. The crucible is locked into the bottom plates of the furnace to prevent the crucible from rotating. The bottom plates are composed of low density alumina to minimize conductive heat loss from the sample. The CO/CO_2 sweep gas is turned on, and the furnace is heated to 1480°C. When the furnace reaches 1480°C, a few grams of pelletized ash are fed from the top. This feeding process is slow enough to allow the pellets to completely melt and degas before the next feeding to prevent the slag from boiling over the sides of the crucible. Once the desired level of the melt is obtained, the bob is lowered from the top, guided by an alignment pin and a stopping plate. This method allows for the viscometer to be assembled in the same way every time, assuring

that the bob is placed in the middle of the slag sample, both horizontally and vertically. Once the viscometer assembly is complete, the temperature is decreased at the rate of 56°C/hr . The viscosity measurements are made every 10 minutes. After the experiment, the slag is cut as shown in Figure 1 and polished for Optical Microscopy (OM) and Scanning Electron Microscopy (SEM) phase analysis. The elemental composition of the slag before and after the viscosity experiments were determined by Inductively Coupled Plasma Emission Spectroscopy (ICP-ES) and phase analysis was conducted by X-Ray Diffraction (XRD).

During the viscosity measurements, the rotation rate of the bob is ramped from 0 to 65 rev/min for 3 mins and back to 0 for the next 3 mins. The shear rate is varied from 0 to 18.2 s^{-1} . The resulting shear rate-shear stress curve is that of a newtonian fluid at high temperatures and characteristic of a non-newtonian fluid at low temperatures. For the viscosity-temperature plot, the viscosity at the highest shear rate was used. Temperature calibration of the equipment was conducted as reported in Oh, et al¹.

Materials: Six synthetic glasses and two coal slags were used in the test program. The synthetic glasses consisted of +99.0 percent pure oxide components as listed in Table 1a. Composition 1 was formulated to match the chemical composition of the ash for a potential plastic feedstock. For Compositions 2 and 3, approximately 10% and 27.5% TiO_2 were added, respectively, to the base case. Barium and magnesium oxides were eliminated from Compositions 4 and 5, and the amounts of calcium and silica were changed while the TiO_2 was held constant. Composition 6 was similar to Composition 3, but without barium oxide being added to the mix.

The coal slags used in the test program were; i) SUFCo (Hiawatha seam, high volatile C bituminous rank) from a commercial plant, and ii) Pittsburgh #8, a bituminous coal, gasified in a pilot unit. The samples were washed and screened to remove most of the carbon. Titanium dioxide was then added at 20% of the slag weight. The chemical composition of the SUFCo slag used in this study contained more calcia, and less silica than previous SUFCo slags that have been used for the calibration runs. For reference purposes, both SUFCo slag viscosities are plotted together.

RESULTS

Final Slag Composition: Both the alumina crucible and bob partially dissolved into the slag and raised the concentration of alumina. Table 1b gives the final composition of the slag, and these values were the ones used in the empirical models. Approximately three percent alumina was added to the SUFCo slag and one percent to the Pitts. #8, which is consistent with previous runs. The calcium and titanium-rich slags dissolved much more alumina, apparently because of the lower slag viscosities at high temperatures. The final chemistry of Composition 2 was not analyzed for this study, because the crucible was destroyed twice before a reasonable viscosity curve could be generated (a phase analysis study is being conducted on the slags from these failed runs in which the chemical analysis will be reported).

Slag Viscosity: Figure 2a contains the viscosity curves of four synthetic slags, SUFCo slags, and SUFCo slag with titanium as a function of temperature. The only slag that exhibited a classic newtonian behavior was the SUFCo slag. Each of the synthetic slags exhibited non-newtonian behavior to varying degrees in which the slags had very low viscosities until a critical viscosity temperature was reached in which the viscosities increased moderately, and then quickly, which led to the spindle snapping. Based on the curves generated during this study; i) at low calcium and high titanium concentrations, the slag starts out fluid, but reaches a critical viscosity at a high temperature (1370°C), ii) at high calcium and moderate titanium levels, the slag is very fluid at low temperatures (1150°C), and iii) at high calcium and high titanium levels, the slag is fluid even at high temperatures, and then reaches a critical viscosity at intermediate temperatures (1270°C).

Figures 2b and 2c contain the viscosity curves of SUFCo and Pitts. #8 slags. Both slags exhibit glassy (newtonian) slag behavior. The result of adding titanium to the SUFCo slag is consistent with the corresponding synthetic slag in that the titanium lowered the viscosity. A critical viscosity may have begun at 1150°C , but the run automatically terminated. For the high iron, Pitts. #8 slag, the addition of titanium appears to have no effect on the viscosity. As a point of reference, the Pitts.#8 slag used in this study is newtonian in behavior compared to the Pitts. #8 generated in our original study which had a dramatic viscosity rise at the critical temperature.

Crystalline Phase Formation: The furnace was turned off at 1190°C and the slags were rapidly cooled by the CO/CO_2 gas mix. After cooling, the crystalline phases and glasses in the slags were examined by SEM. The phases identified were TiO_2 (rutile) and $\text{CaAl}_2\text{Si}_2\text{O}_8$ (anorthite). Both phases were physically aligned with one another. All samples were sent to a university for further analysis and will be reported on at a later date.

DISCUSSION

None of the slags exhibited sharp increase in viscosity at their normal critical viscosity temperature as seen in some previous tests. Therefore, the chemical compositions of the final slags were used in the various models to determine how well the models correlated with the experimental data. Based on the limitations of the models as shown in Table 2, the Watt-Fereday model most closely matches the test conditions.

The actual viscosity of each slag was plotted against the four models. Based on these plots, the Urbain model most closely matches the slag viscosity for the calcium-rich slags, and all of the titanium-rich slags. The only slag samples that the Urbain model did not predict well were the high iron, Pitts. #8 and the intermediate calcium, titanium-rich slag (none of the models were in agreement with this composition).

Even though the Urbain model most closely matches the data, at high titanium concentrations the model predicts higher viscosities than the test run data. The most likely cause for the discrepancy would be the formation of a calcium-titanium-silicate glass phase that has; i) a lower melting point than the calcium-aluminosilicate glass, and ii) a flatter liquidus within its phase boundaries than anorthite. The large crystalline phases that formed during cooldown appear to have little effect on the viscosity as indicated by their orientation to the flow direction within the slag as it spun around the bob.

The Watt-Fereday and Si Ratio model gave the best fit for the high iron slag. Again, based on the compositional limit in Table 2, the Watt-Fereday model contains the most elements within the boundary conditions. In previous runs with Pitts. #8, hercynitic spinels came out of solution rapidly creating a critical viscosity. The difference between the Pitts. #8 used during this test and that used in the prior work was; i) the presence of more iron, and ii) the iron was more likely to be in the +2 valence state (the slag was reduced in the gasifier, while the Pitts. #8 ash used in the first study may not have fully reduced during testing).

The lack of change in viscosity of the Pitts. #8 slag when titanium was added was unexpected. The glass phase should be of fayalite composition which has a low melting point. In previous tests, hercynitic spinels crystallized out of solution, and one would suspect that with the added TiO_2 , FeTiO_3 (ilmenite) which was present would crystallize out of solution near 1300° C and affect the viscosity more noticeably. The combined presence of FeAl_2O_4 and FeTiO_3 should abruptly raise the slag viscosity which was not seen. Several additional runs, along with phase prediction will be done in the future.

CONCLUSIONS

The slag viscosity data for calcium and titanium-rich feeds are consistent with previous studies in that; i) titanium will lower the melting point of a calcium aluminosilicate glass for TiO_2 up to 27.5%, and ii) the higher the calcium concentration, the more fluid the glass will be with or without titanium, for CaO contents up to 30%. The most consistent model for the calcium-titanium aluminosilicate system under reducing conditions is the Urbain Model. For higher iron slags, the Watt-Fereday Model appears to be a better system for predicting viscosity. However, a high iron slag will have a greater likelihood of nucleating a high melting spinel or ilmenite phase, causing a critical viscosity to develop as iron is rapidly withdrawn from the glass phase.

REFERENCES

1. Oh, M. S., Brooker, D. D., DePaz, E.F., Brady, J. J., and Decker, T. R. 1995; Effect of crystalline phase formation on coal slag viscosity. *Fuel Processing Technology*, 44, 191-199.
2. Watt, J. D., and Fereday, F., 1969. Flow properties of slag formed from the ashes of British Coal; I. Viscosity of homogeneous liquid slags in relation to slag composition. *J. Inst. Fuel*, 42, 99-103.
3. Urbain, G., Cambier, F., Deletter, M., and Anseau, M. R., 1981. Viscosity of silicate melts. *Trans. J. Brit. Ceram. Soc.*, 80:139.
4. Corey, R. C., 1964. Measurements and significance of the flow properties of coal-ash slag. *US Bureau Mines Bull.* No. 618.
5. Schobert, H. H., Streeter, R. C., and Diehl, E. K., 1985. Flow properties of low-rank coal ash slags. Implication for slagging gasifiers. *Fuel*, 64:1611.
6. Monteiro, R. C. C., Silva, F. I. F., and Lima, M. R. A., 1992. Effect of the addition of TiO_2 and ZrO_2 on the crystallization of calcium aluminosilicate glasses. XVI International Congress on Glass. Vol. 5.

TABLE 1A - CHEMICAL ANALYSES (ICAP) - STARTING MATERIAL

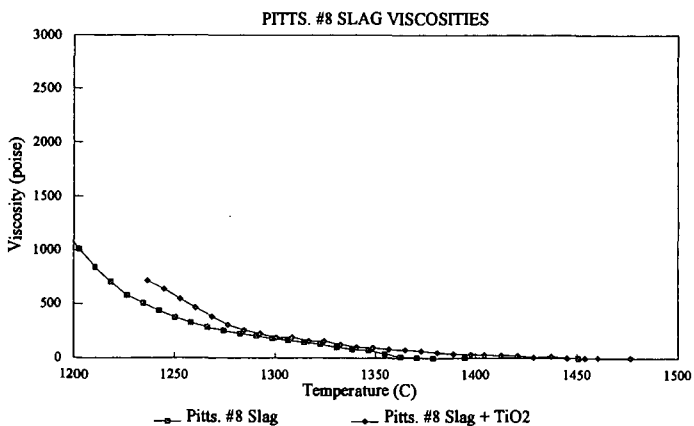
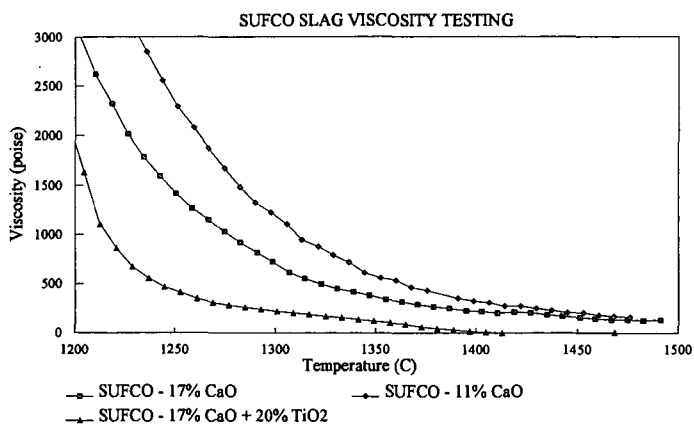
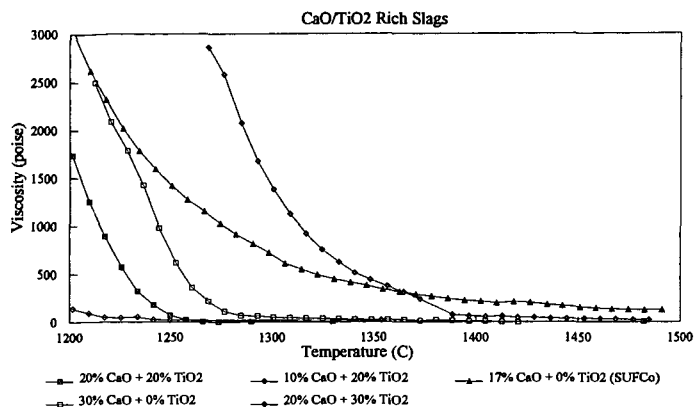
| | SUFCo | Pitt. 8 | Run1 | Run2 | Run3 | Run4 | Run5 | Run6 |
|--------------------------------|-------|---------|------|------|------|------|------|------|
| SiO ₂ | 62.7 | 44.2 | 42.1 | 37 | 30.5 | 50 | 40 | 30 |
| Al ₂ O ₃ | 11.9 | 23.7 | 14.9 | 13.5 | 11 | 15 | 15 | 11 |
| CaO | 11.5 | 3.5 | 26.5 | 23.8 | 19.3 | 10 | 20 | 19.3 |
| TiO ₂ | 1.1 | 1.1 | 0 | 10.8 | 27.4 | 20 | 20 | 27.3 |
| Fe ₂ O ₃ | 6.2 | 22.3 | 9.4 | 8.4 | 6.6 | 5 | 5 | 6.8 |
| MgO | 2.3 | 1 | 3.8 | 3.2 | 2.6 | 0 | 0 | 2.6 |
| Na ₂ O | 2.6 | 1.7 | 0 | 0 | 0 | 0 | 0 | 0 |
| BaO | 0 | 0 | 3.25 | 2.9 | 2.4 | 0 | 0 | 0 |

TABLE 1B - CHEMICAL ANALYSES (ICAP) - END MATERIAL

| | SUFCo + TiO ₂ | Pitt. 8 + TiO ₂ | Run1 | Run3 | Run4 | Run5 | Run6 | Run6b |
|--------------------------------|-----------------------------|-------------------------------|------|------|------|------|------|-------|
| SiO ₂ | 53.4 | 33.3 | 40.5 | 27.1 | 46.7 | 40.4 | 29.7 | 30.1 |
| Al ₂ O ₃ | 15 | 24.6 | 21.2 | 21.4 | 18.5 | 15.8 | 17.1 | 15.5 |
| CaO | 9.6 | 2.7 | 20.4 | 14.6 | 8.1 | 16.8 | 15.8 | 16.1 |
| TiO ₂ | 13 | 20 | 0 | 24.9 | 20.8 | 20.8 | 26.7 | 27.5 |
| Fe ₂ O ₃ | 5.4 | 18.8 | 9.3 | 8.1 | 5.9 | 5.4 | 6.8 | 6.8 |
| MgO | 1.9 | 0.8 | 3.4 | 2.4 | 0.2 | 0.2 | 2.8 | 1.9 |
| Na ₂ O | 2.3 | 1.4 | 0 | 0 | 0 | 0 | 0 | 0 |
| BaO | 0 | 0 | 2.3 | 1.6 | 0 | 0 | 0 | 0 |

TABLE 2 LIMITATIONS OF MODELS

| Oxides | Wt. % | Normalized Wt % | Riboud | Urbain | W-F | SiRatio |
|--------------------------------|-------|--------------------|--------|--------|-------|---------|
| SiO ₂ | 40.4 | 40.8 | 34-56 | 43-73 | 30-60 | 30-59 |
| Al ₂ O ₃ | 15.8 | 15.8 | 0-12 | 8-14 | 15-35 | 15-30 |
| FeO | 5.3 | 5.4 | 8-46 | 2-28 | 3-30 | 5-31 |
| MgO | 0.2 | 0.2 | 8-46 | 0-7 | 1-10 | 1-15 |
| CaO | 16.8 | 16.8 | 8-46 | 1-9 | 2-30 | 0-30 |
| Na ₂ O | 0 | 0.0 | 0-22 | 0-4 | 0 | 0 |
| K ₂ O | 0 | 0.0 | 0-22 | 0-5 | 0 | 0 |
| TiO ₂ | 20.8 | 21.0 | 0 | 0 | 0 | 0 |
| P ₂ O ₅ | 0 | 0.0 | 0 | 0 | 0 | 0 |
| MnO | 0 | 0.0 | 0 | 0-0.3 | 0 | 0 |
| ZrO ₂ | 0 | 0.0 | 0 | 0 | 0 | 0 |
| B ₂ O ₃ | 0 | 0.0 | 0 | 0 | 0 | 0 |
| CaF ₂ | 0 | 0.0 | 0-16 | 0 | 0 | 0 |



Figures 2a-c. Slag viscosity measurements of various slags.

DISSOLUTION OF LIME INTO SYNTHETIC COAL ASH SLAGS.

Liza Elliott¹, Shen Mao Wang¹, Terry Wall¹, Fred Novak², John Lucas¹, Harry Hurst², John Patterson², Jim Happ³.

¹Department of Chemical Engineering
Newcastle University, Australia. (Callaghan 2308)

²CSIRO Division of Coal & Energy Technology
North Ryde, Australia, 2113.

³CRA Advanced Technical Development
1 Research Ave, Bundoora, Australia, 3083.

Keywords: CaO, lime, dissolution, slags, coal ash.

ABSTRACT

One of the alternate processes presently being investigated to produce electrical power from coal is Integrated Gasification Combined Cycle (IGCC). The ash that remains when the coal is gasified in this process, is removed by granulating the molten ash at 1400 - 1500°C. To reduce the melting temperature of the coal ash to this level, a flux, usually limestone, is added with the coal to the gasifier. The rate of dissolution of the flux is uncertain.

This paper reports the investigation of the rate of lime dissolution into synthetic coal ashes, consisting of SiO₂, Al₂O₃ and CaO. Results previously reported have shown that the free dissolution of fine particles (50-200µm) is mass transfer controlled. To investigate forced dissolution, a high temperature viscometer was used to rotate a cylinder of lime in the molten slag for a given period. At temperatures between 1450°C and 1650°C, reaction products of 3CaO.SiO₂/3CaO.Al₂O₃, 2CaO.SiO₂/3CaO.Al₂O₃/12CaO.7Al₂O₃ form around the lime pellet. The concentration gradient involved in the mass transfer was defined, and initial studies of the diffusion coefficients were completed.

INTRODUCTION

Entrained flow gasifiers partially combust coal at elevated temperatures and pressures to create a product gas consisting of carbon monoxide and hydrogen, which is combusted in a gas turbine to produce electrical power. The ash that remains after this combustion, must melt to allow the resulting slag (molten ash) to run down the walls of the gasifier and is tapped from the base of the gasifier. The minimum temperature experienced by the ash within the gasifier is usually between 1400 and 1500°C. The ash must therefore be molten at these temperatures for the ash to be efficiently removed from the gasifier.

Coals with high ash fusion temperatures require the addition of a flux with the coal to lower the melting point of the ash. The alternative, increasing the operating temperature lowers the process efficiency, which is undesirable. Usually this flux is CaCO₃, which, when exposed to the atmosphere within the gasifier breaks down into CaO and CO₂. The flux reduces the viscosity of the resulting slag (depending on the ash being considered).

This paper considers the dissolution process of lime into synthetic coal ash slags, that consist of silica, alumina and lime for forced dissolution and silica, alumina, lime and ironoxide for free dissolution. Our preliminary results have shown that for no convection, dissolution from small lime particles in a synthetic ash is mass transfer controlled and a dicalcium silicate layer formed around the lime particles.⁽¹⁾

Matsushima⁽²⁾ et al. investigated the forced dissolution rate of lime in SiO₂-Al₂O₃-CaO and SiO₂-FeO-CaO slags and found a 2CaO.SiO₂ layer around the solid lime, though he suggested that the layer did not sit next to the lime but was separated by a slag layer. Matsushima determined a boundary layer size by an equation using dimensionless numbers, (determined for the dissolution of steel) and by determining the mass transfer constant $k = \frac{D}{\delta}$ by a mass transport equation and assuming $D = 5.5 \times 10^{-6}$ cm²/s. Samaddar et al.⁽³⁾ investigated the dissolution of alumina, mullite, anorthite and silica in CaO-SiO₂-Al₂O₃ melts with a similar technique as used here. Cooper et al.⁽⁴⁾ also used this technique to study sapphire dissolution and Taira et al.⁽⁵⁾ studied dissolution of alumina in similar slags, while Gudenau et al.⁽⁶⁾ and Olsson et al.⁽⁷⁾ studied the dissolution of carbon into hot metal baths.

METHOD

Free Dissolution.

Small particles of lime, with average diameters of 275, 500 and 750 µm were mixed into synthetic coal ash mixtures: 60SiO₂-30Al₂O₃-6Fe₂O₃-4CaO(wt%). The mixtures of ash and lime were

placed in a platinum crucible and heated in a vertical tube furnace to 1400, 1500 or 1600°C for a defined time in an argon atmosphere. At the end of the experiment, the melt was removed from the furnace and quenched.⁽¹⁾ The regions around the lime particles were studied quantitatively under the Scanning Electron Microscope using EDAX to establish concentration profiles, and the amount of unreacted lime determined by an oxalic titration method.⁽³⁾

Forced Dissolution.

Cylindrical pellets of lime were produced by pressing powdered lime in a die and then sintering the pellets in a muffle furnace for two hours at 1550°C. Samples of slag were premelted from reagent grade oxides, producing a homogeneous melt prior to dissolution experiments. Each slag sample was produced in a molybdenum crucible liner, ensuring no dissolution of carbon from the outer graphite crucible occurred. The slag compositions selected are based on coal ash silica to alumina ratios (2 to 3.35). The range of lime content in slag (15 to 25 wt%), was chosen to ensure the melt would be completely fluid at temperatures used in this set of experiments.

At the beginning of each dissolution experiment, a pellet was suspended on a molybdenum rod above a melt in a vertical tube furnace, refer Figure 1, allowing the pellet to heat to approximately the same temperature as the melt. The furnace atmosphere was kept at a mildly reducing composition by the graphite crucible, which reacted with any oxygen entrained into the furnace with the nitrogen purge gas. Each melt was maintained at temperature for at least thirty minutes to allow the melt to equilibrate. The pellet was then lowered into the melt and rotated at the desired speed for a given period of time. To remove the pellet at the end of a test, a molybdenum cradle containing the crucible the pellet still in position in the melt, was lifted out of the furnace into a cooling tube. Nitrogen was directed onto the crucible to cool it as quickly as possible, as shown in Figure 2. This required three to five minutes.

The frozen melt in the crucible was sectioned through the vertical axis of the pellet and polished before the concentration profile around the lime pellet was determined using a Scanning Electron Microscope. The change in size of the pellet was also measured.

The thickness of the boundary layer was determined by fitting an exponential equation to the lime concentration profile. The boundary layer size is assumed to be the distance from the lime source to the point where the lime concentration does not change (within 1%). The diffusion coefficient for lime dissolving into SiO₂/Al₂O₃/CaO slags was determined from equation 1:

$$-j = \frac{dx}{dt} = \frac{D(C_i - C_\infty)}{\sigma(1 - V_i C_i)} \quad \text{eqn 1}^{(3)}$$

Where j is the flux of lime, x the amount of lime (in cm) removed from the lime pellet, t the time of dissolution, D the lime diffusion coefficient, σ the boundary layer size, C_i the saturation lime concentration at experimental temperature, C_∞ the bulk slag lime concentration and V_i a volume fraction, or $\frac{\rho_s}{\rho_l}$ (the ratio of the density of the solid and liquid phases).

RESULTS

Free Dissolution

A 3CaO·Al₂O₃ + 2CaO·SiO₂ layer (reaction zone) was found to form around the lime particles, with no separation of the layer from the lime by slag, after which the lime concentration falls to the bulk slag concentration. Figure 3 shows the lime concentration outside the crystalline phases does not fall evenly as it is affected by dissolution of lime from adjacent particles. Using the model of a shrinking particle in a fluid with changing concentration, the rate of mass transfer through the melt was found to be the rate limiting step in the dissolution process, as shown in Figure 4.⁽¹⁾

Forced Dissolution

A typical concentration profile in the slag around the pellet is shown in Figure 5. The figure shows a reaction zone followed by an area that exhibits a concentration profile typical of diffusion control. The reaction zone is a combination of 2CaO·SiO₂ and 3CaO·SiO₂. The corresponding alumina phase: 3CaO·Al₂O₃, on the CaO-Al₂O₃-SiO₂ phase diagram, is only seen at the end of the reaction zone, though it is believed to occur throughout the reaction zone in fine defined ribbons around the aluminosilicate crystals. This behaviour of the two types of crystals forming an unhomogeneous layer around the lime is shown in maps of the reaction zone from the Scanning Electron Microscope, Figure 6. The brighter the points appears on the image, the higher the concentration

of that species. The aluminium concentration in this region is higher than can be completely accounted for in the compound $3\text{CaO} \cdot \text{Al}_2\text{O}_3$. Some $12\text{CaO} \cdot 7\text{Al}_2\text{O}_3$ is also being created in this region, though no discrete particles can be determined as it is finely divided amongst the other tricalcium-aluminate crystals.

Other samples showed very little evidence of $3\text{CaO} \cdot \text{SiO}_2$ in the reaction zone, consisting mainly of $2\text{CaO} \cdot \text{SiO}_2$, as shown in Figure 7. This figure also shows the existence of $3\text{CaO} \cdot \text{Al}_2\text{O}_3$, again with some $12\text{CaO} \cdot 7\text{Al}_2\text{O}_3$, to account for the alumina content found, at the interface of the lime pellet and the reaction zone. To produce these compounds the alumina concentration rises well above the bulk slag alumina concentration. This indicates that these phases are crystalline.

The diffusion coefficients calculated from the concentration profile of lime from the end of the "reaction zone" to the bulk slag concentration are given in Table 1. The diffusion coefficient calculated from the forced diffusion experiments are variable. Work is continuing on this area. These initial experiments appear to indicate that temperature may have a greater effect on the size of the reaction zone than the speed of rotation. The size of the boundary layer appears to be affected by both the change in temperature and the speed of rotation. The size of the boundary layer should theoretically decrease with increasing rotational speed, while increasing temperature will decrease the viscosity, affecting the boundary layer size. The results shown are inconclusive and further work is required.

CONCLUSIONS

- The rate limiting step of dissolution of lime into molten ash is the mass transport of the lime into the slag, for both forced and free dissolution.
- A crystalline layer of $2\text{CaO} \cdot \text{SiO}_2$ or $3\text{CaO} \cdot \text{SiO}_2$ interspersed with $3\text{CaO} \cdot \text{Al}_2\text{O}_3$ form around a lime particle dissolving into molten ash.
- The driving force for the mass transport step appears to be the difference between the CaO concentration at the reaction zone and the bulk slag.

ACKNOWLEDGMENTS

The authors acknowledge the financial support of CRA Advanced Technical Development. The CSIRO authors acknowledge the financial support of the NSW State Energy Research and Development Fund, the Australian Coal Association Research Program and the Energy Research and Development Corporation (Australia).

REFERENCES

1. Wang S. M. et al. Experimental Studies and Computer Simulation of Dissolution of Lime Particles into Coal Ash Slags. Australian Symposium on Combustion and the Fourth Flame Days, University of Adelaide, South Australia, November 9-10, 1995.
2. Matsushima, M., et al. A Fundamental Study on the Dissolution Rate of Solid Lime into Liquid Slag. Transactions ISIJ, Vol 17, 1977, p442 - 449.
3. Samaddar B. N. et al. Dissolution in Ceramic Systems: 11, Dissolution of Alumina, Mullite, Anorthite and Silica in a Calcium-Aluminum-Silicate Slag. Journal of the American Ceramic Society, Vol. 47, 1964, p249 - 254.
4. Cooper A. R. et al. Dissolution in Ceramic Systems: 1, Molecular Diffusion, Natural Convection, and Forced Convection Studies of Sapphire Dissolution in Calcium Aluminium Silicate. Journal of the American Ceramic Society, Vol 47 (1) 1964, p 37 - 43.
5. Taira, S. et al. Kinetic Behaviour of Dissolution of Sintered Alumina into $\text{CaO-SiO}_2\text{-Al}_2\text{O}_3$ Slags, ISIJ International Vol 33, (1) 1993 p116 - 123.
6. Gudenau et al. Dissolution of Carbon Brocks in Hot Metal Baths (Auflösung sverhalten von Kohlenstoffsteinen im Roheisenbad. Stahl Eisen Vol. 111 (2), 1991 p89 - 94.
7. Olsson, R. G. et al. Rate of Dissolution of Carbon in Molten FeO-C alloys. Transactions of the Metallurgical Society of AIME, Vol 236, 1966 p426 - 429.
8. Russell, R. O. Journal of Metals, 19 (8), 1967. P104.

FIGURES

Table 1: Diffusion Coefficient Estimates from equation 1.

| $\text{SiO}_2/\text{Al}_2\text{O}_3$ | CaO % | Rotational Speed rpm | Temperature °C | Reaction layer thickness mm | Boundary layer thickness mm | Diffusion coefficient $\text{cm}^2/\text{s} \cdot 10^{-13}$ |
|--------------------------------------|----------|----------------------------|-------------------|-----------------------------------|-----------------------------------|---|
| 3.35 | 25 | 83.25 | 1550 | 0.0544 | 7.2484 | 6.9 |
| 3.35 | 25 | 83.5 | 1450 | 0.056 | 5.39 | 11.4 |
| 3.35 | 25 | 37.15 | 1450 | 1.328 | 5.8 | 6.89 |
| 3.35 | 25 | 20 | 1450 | 0.0587 | 2.35 | 2.04 |
| 3.35 | 25 | 110 | 1450 | 0.0267 | 0.518 | 0.326 |
| 2.25 | 15 | 83.5 | 1550 | 0.039 | 0.933 | 0.784 |
| 2.25 | 20 | 74 | 1450 | 0.384 | 9.539 | 6.5 |
| 2.25 | 20 | 74 | 1650 | 0.190 | 4.7664 | 8.5 |

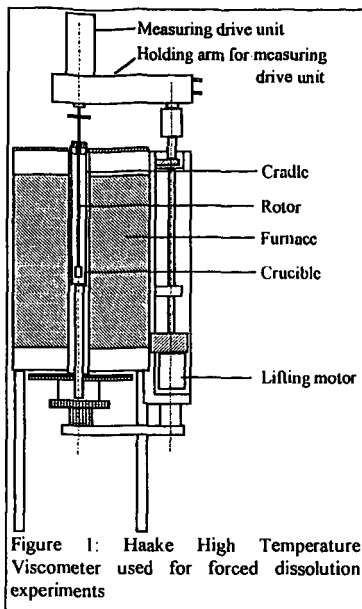


Figure 1: Haake High Temperature Viscometer used for forced dissolution experiments

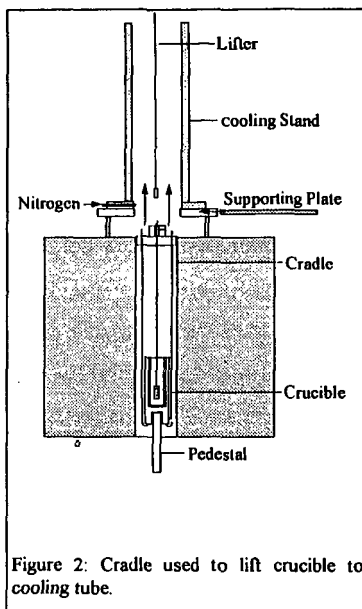


Figure 2: Cradle used to lift crucible to cooling tube.

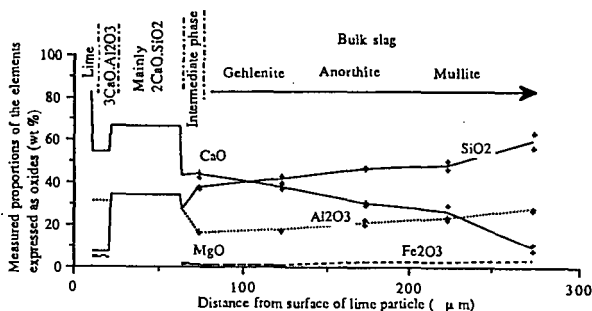


Figure 3: Free Dissolution Concentration Profile around a 750 μm lime particle in slag at 1500°C

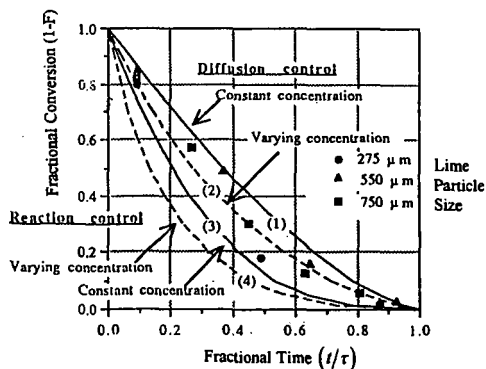


Figure 4: Free Dissolution Experiments: Comparison of Experimental Results with Theoretical Curves for Dissolution Rates Controlled by Diffusion and Reaction Kinetics.

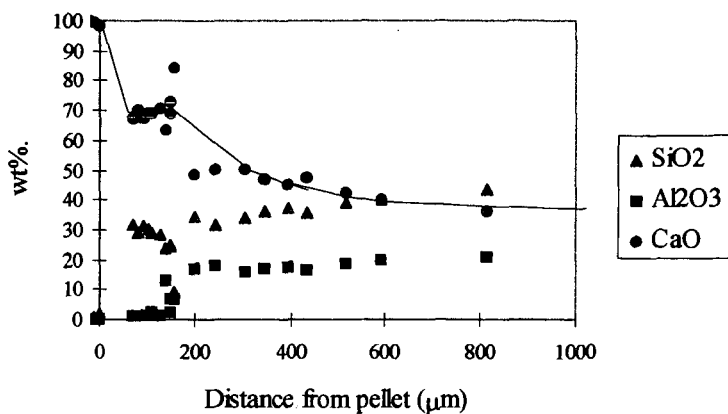


Figure 5: Forced Dissolution Concentration Profile around lime Pellet, $\text{SiO}_2/\text{Al}_2\text{O}_3=2.25$, at 1450°C

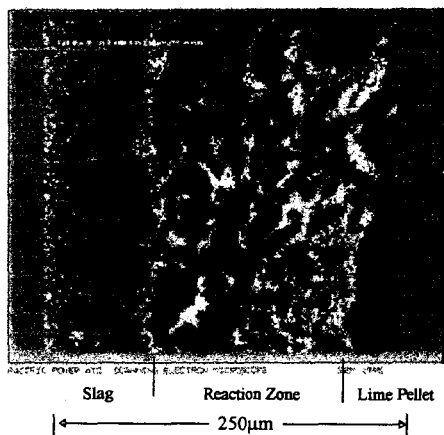


Figure 6: Aluminium Intensity Map

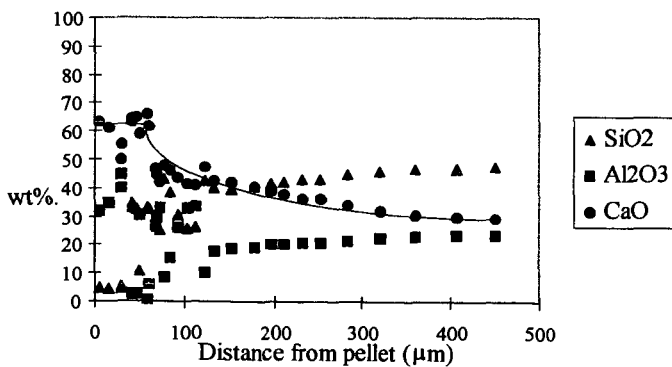


Figure 7: Forced Dissolution Concentration Profile around lime Pellet, $\text{SiO}_2/\text{Al}_2\text{O}_3=2.25$, at 1650°C

THE EFFECTS OF ATMOSPHERE AND ADDITIVES ON COAL SLAG VISCOSITY

John P. Hurley

Tina M. Watne

Jan W. Nowok

Energy & Environmental Research Center

PO Box 9018

Grand Forks, ND 58202-9018

Keywords: Slag, viscosity, and coal slag

ABSTRACT

The viscosities of a Powder River Basin slag were measured in air, air + 10% water vapor, and a reducing atmosphere. The temperature of critical viscosity (T_c), below which the viscosity increases dramatically, was approximately 1250°C in air and air + water vapor, but dropped to 1180°C when measured in the reducing atmosphere. Since the corrosivity of the slag is much higher when its viscosity is low, the slag will be highly corrosive at the substantially lower temperature in reducing gas. The addition of alumina increased viscosity and T_c , making the slag less corrosive, while magnesia additions dropped viscosity but increased T_c . These changes imply that magnesia additions will make the slag slightly more corrosive in its liquid range, but that the slag will harden and become less corrosive at a higher temperature than without the magnesia addition. The changes in T_c were more substantial when measured in the presence of water vapor in the case of alumina additions, but less substantial in the case of magnesia additions.

INTRODUCTION

As coal reacts in an energy system, the inorganic material in the coal reacts to form silica-rich ash. If the temperature of the ash is high enough, it will completely fuse, forming a molten slag. This slag is very erosive and corrosive to energy system materials with which it comes in contact. The viscosity of the coal ash slag determines its flow rate which affects its erosivity, and the diffusivity of ions within the slag which affects its corrosivity. Several phenomenological models based on linear regression analysis of slag composition-versus-viscosity data have been developed to predict the viscosity of coal ash slags in combustor systems.¹⁻⁴ However, these models only work well in predicting slag viscosity at the conditions under which the composition-versus-viscosity data were developed, and it is not well understood how far the predictions can be extended to other system conditions such as variations in local atmosphere. In addition, the models do not predict the temperature at which crystallization starts in the slag, known as the temperature of critical viscosity T_c , below which the viscosity sharply rises. This means that the minimum temperature to which the models can be applied or to which slag can be expected to flow is not well known.

In this article, we report the impact of three gas compositions, each of which may be expected in various regions of a coal-fired boiler, on the viscosity and critical temperature on a high-calcium coal slag produced from a Powder River Basin coal. We also demonstrate how these properties can be manipulated with the use of coal additives in order to reduce their corrosiveness to energy system materials.

EXPERIMENTAL

The viscosity of the slags were measured under three atmospheres: air, air + 10% water vapor, and $H_2/CO/CO_2$ (31/45/24). In addition, reagent-grade magnesium oxide (45 wt%) or aluminum oxide (20 wt%) was added to the slags under both air and air + 10% water vapor conditions. Viscosities were measured with a Haake RV-2 Rotovisco system with a DMK 50/500 dual measuring head, which is a rotating bob viscometer. In this system, the torque on the viscometer bob is converted to an electrical signal to a computer, which controls the rotation at 64 rpm. For oxidizing atmosphere tests, the bob was fabricated from platinum-rhodium (90/10) alloy. For reducing atmosphere tests, the bob was fabricated from molybdenum. In both cases, the bob was 22 mm long with a 30° taper at both ends. The top of the bob terminated in a 16-mm-long, 6-mm-diameter shaft accommodating a 420-mm-long by 3-mm-diameter stem. The bob was immersed until the slag just covered its top. The coal slags were prepared by melting ash powders at 1500°C in air in a platinum crucible and quenched on a brass plate at room temperature. The glasses were crushed, put into alumina crucibles, and heated to 1500°C. The viscosity of the slags were measured over the range of 10 to as high as 4000 poise unless crystallization was seen to occur along the walls of the alumina container, at which point the measurements were terminated. Measurements were started at a temperature of at least 100°C above the temperature of critical viscosity, and the temperature was decreased in 20°C intervals. The bob was rotated in the slag for approximately 40 minutes after each temperature was reached before a reading was taken. The viscometer was calibrated with National Bureau of Standards silicate glasses 710 and 717. The accuracy of the tests is approximately $\pm 5\%$. Compositions of the original ash is listed in Table 1.

TABLE 1

Compositions of Coal Ashes, wt% oxide basis

| Oxide Coal | |
|--------------------------------|-----------------|
| SiO ₂ | 38.8 |
| Al ₂ O ₃ | 20.8 |
| Fe ₂ O ₃ | 6.1 |
| TiO ₂ | 1.5 |
| P ₂ O ₅ | 1.1 |
| CaO | 23.2 |
| MgO | 6.5 |
| Na ₂ O | 1.4 |
| K ₂ O | 0.3 |
| SO ₃ | ND ¹ |

¹ Not detected.

RESULTS AND DISCUSSION

Figure 1 shows the viscosity-versus-temperature curves for the Powder River Basin coal slag in air, air + 10% moisture, and reducing conditions. The curves are very similar for both the air and air + moisture tests, with T_c approximately 1250°C and the viscosity of each slag around 20 poise at 1400°C. However, under the reducing conditions, T_c dropped considerably to 1180°C, and the viscosity of the slag at 1400°C was only around 5 poise. These changes cannot be explained merely by the reduction of iron in the slag from a network former (3+ ion) to a network modifier (2+ ion) since there is so little in the slag.

Figure 2 shows the effects of the additions of alumina and magnesia to the slag when measured in air. As expected, the addition of a network former like alumina increased the viscosity of the slag at 1400°C from 20 to 40 poise. In addition, the temperature of critical viscosity was increased dramatically from 1250°C for the original ash to 1330°C with the alumina addition. X-ray diffraction showed the formation of plagioclase ([Ca,Na][Al,Si]₄O₈) and spinel (MgAl₂O₄) crystals in the melt below T_c . In contrast, the addition of magnesium, a network modifier, to the melt decreased its viscosity as expected, but increased T_c even more, to around 1350°C. Crystals forming in that melt included spinel and monticellite (CaMgSiO₄). The changes in viscosity indicate that alumina additions would decrease the corrosivity of a Powder River Basin slag, while magnesia additions may slightly increase corrosivity. However, because T_c is increased in each case, either addition would dramatically lower slag corrosivity at material temperatures 80° to 100°C higher than the T_c of the slag alone.

Figure 3 shows the effects of the additions of alumina and magnesia to the slag when measured in air + 10% moisture. As was true for the measurements in air, adding alumina raised the viscosity and T_c of the slag but much more substantially, with the viscosity increased by 60 poise at 1400°C while T_c rose by 140°C. This increase in viscosity would reduce the corrosivity of the slag to energy system materials, dramatically reducing the corrosivity of the slag at temperatures below 1400°C. The additions of magnesia also created similar changes as when measured in air. The viscosity of the slag at 1400°C dropped by approximately 10 poise, but T_c rose by only 50°C to 1310°C.

CONCLUSIONS

The viscosity and T_c of a Powder River Basin slag is not substantially different when measured in air or in air + 10% water vapor, but both are substantially reduced when measured in an H₂/CO/CO₂ atmosphere. The reduction is more than would be expected from the conversion of iron from a 3+ ion to a 2+ ion. Adding alumina, a network former, increased viscosity and T_c when measured in air, but more substantially when measured in air + 10% water vapor. The addition of magnesia, a network modifier, to the slag dropped the viscosity and raised T_c , but the change in T_c was less substantial in air + water vapor than when measured in air alone. Either addition will have small effects on corrosivity of the slags above T_c , but will dramatically reduce corrosivity below the new T_c of the modified slags. Also, since combustor gas contains more water vapor than air alone, we suggest that in order to gauge the effect of additives on slag viscosity accurately, viscosity measurements should be made in an atmosphere containing water vapor.

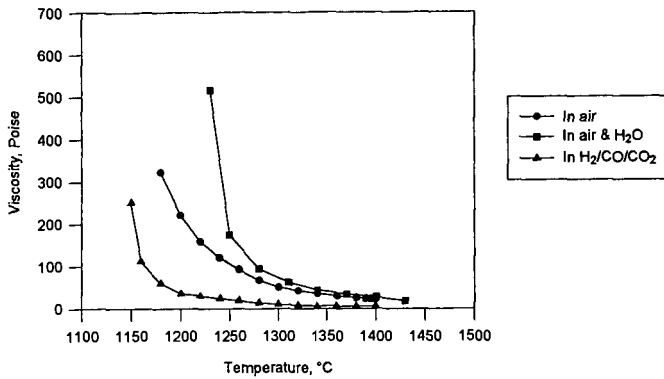


Figure 1. Viscosity-versus-temperature curves for the Powder River Basin coal slag in air, air + 10% moisture, and reducing conditions.

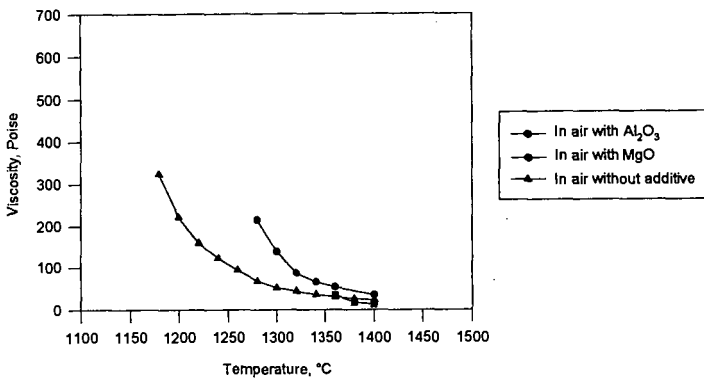


Figure 2. Viscosity-versus-temperature curves measured in air for the Powder River Basin coal slag, slag plus alumina, and slag plus magnesia.

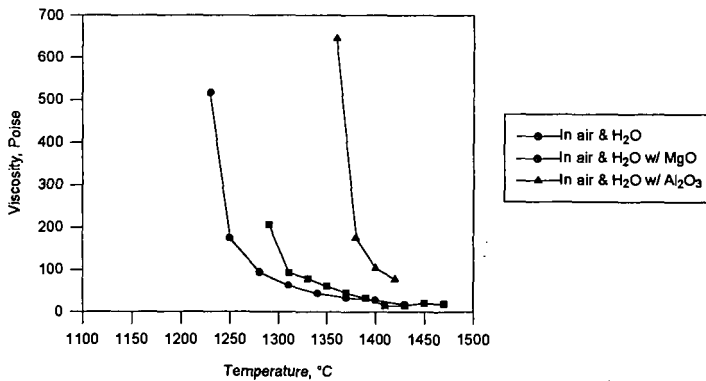


Figure 3. Viscosity-versus-temperature curves measured in air + 10% moisture for the Powder River Basin coal slag, slag plus alumina, and slag plus magnesia.

REFERENCES

1. Urbain, G.; Cambier, F.; Deletter, M.; Anseau, M.R. *Trans. J. Br. Ceram. Soc.* **1981**, *80*, 139.
2. Kalmanovitch, D.P.; Frank, M. *In Proceedings of the Conference on Mineral Matter and Ash Deposition from Coal*; Engineering Foundation, Santa Barbara, 1988, p 89.
3. Jung, B.; Schobert, H.H. *Energy and Fuels* **1992**, *6*, 387-398.
4. Nowok, J.W.; Hurley, J.P.; Steadman, E.N. *In Proceedings of the Conference on the Impact of Ash Deposition on Coal-Fired Plants*; Engineering Foundation, Solihull, England, 1993.